Seeing The Invisible: Single Molecule Microscopy in the Shortwave Infrared

by

Raoul Emile Correa

B.S. Chemistry, University of California, Berkeley (2008)

Submitted to the Department of Chemistry
in partial fulfillment of the requirements for the degree of

Doctor of Philosophy

at the

MASSACHUSETTS INSTITUTE OF TECHNOLOGY

September 2013

Author .....
Department of Chemistry
August 6, 2013

Certified by .....
Moungi G. Bawendi
Professor of Chemistry
Thesis Supervisor

Accepted by .....
Robert W. Field
Chairman, Departmental Committee on Graduate Students

This doctoral thesis has been examined by a committee of the Department of Chemistry as follows:

.....

Professor Troy Van Voorhis
Thesis Committee Chairman

.....

Professor Moungi G. Bawendi
Thesis Adviser
Thesis Committee Member

.....

Professor Keith A. Nelson
Thesis Adviser
Thesis Committee Member

.....

Professor Sylvia T. Ceyer
Thesis Committee Member

Seeing The Invisible: Single Molecule Microscopy in the Shortwave Infrared

by

Raoul Emile Correa

Submitted to the Department of Chemistry
on August 6, 2013, in partial fulfillment of the
requirements for the degree of
Doctor of Philosophy

Abstract

Infrared-active nanostructures play an increasingly important role in the nanoscience toolbox, yet little is known about their optical properties at the single nanoparticle level. In this thesis, we detail efforts to extend the power of single-molecule spectroscopy into the shortwave-infrared (SWIR), marrying confocal microscopy with superconducting nanowire single photon detectors that operate very efficiently in this portion of the spectrum.

As a proof of principle, we interrogate single lead sulfide (PbS) nanocrystals emitting at 1100 nm and observe fluorescence intermittency (blinking) under continuous excitation. The extracted on/off waiting-time statistics were power-law distributed, with exponents nearly identical to those measured from visible NCs. In addition, we demonstrate the feasibility of performing sophisticated photon correlation experiments on weak SWIR emitters and confirm that the photoluminescence from single PbS NCs displays sub-Poissonian photon statistics, strong evidence for single-NC localization.

Next, we use our unique apparatus to probe two key steps in the exciton lifecycle of single 1300-nm-emitting indium arsenide nanocrystals: the time evolution, and subsequent recombination, of single and multiple excitons. Upon correlating PL intensity with the lifetime decay, we discover that InAs/CdZnS nanocrystals blink in one of two ways, either with the PL decay rate fluctuating simultaneously or remaining constant for all PL intensities other than the off state. Surprisingly, we observe grey-state emission - commonly attributed to trion recombination - with a PL lifetime nearly equal to the bright state (attributed to neutral exciton recombination). For the 21 NCs studied, we observe significant heterogeneity in single-NC radiative lifetimes (47 to 179 ns), while simultaneously measuring a near-zero biexciton quantum yield across the sample.

Finally, we perform single-NC spectroscopy on a new generation of CdSe/CdS nanocrystals and extract kinetic rates of recombination for both neutral and charged excitons, which we assign to the bright and grey state respectively. By correlating the instantaneous PL lifetime with the PL intensity using fluorescence-lifetime-intensity-

distribution (FLID) plots, we assess the prospects of alternative blinking mechanisms in 2-monolayer and 7-monolayer CdSe/CdS NCs, as well as QD Corp. NCs (QDC655), and find little evidence for anomalous blinking (i.e. the recently proposed Type B blinking) for all three NC systems.

Thesis Supervisor: Moungi G. Bawendi
Title: Professor of Chemistry

Acknowledgments

Graduate school has been a time of intense personal and scientific growth for me, an experience made possible by the brilliant minds and personalities I have encountered over the past five years. What makes this even more special is that, in most instances, the same group of people are responsible for both forms of maturation - a testament to the kind of scientist this Institute attracts, and produces.

At the root of this growth is my thesis advisor, Moungi Bawendi. His unwavering approach to science inspired the work contained in this thesis, creating an atmosphere of openness where even poor-signal-to-noise data was not shunned, but instead treated as a stepping stone towards publication-quality measurements. Despite my frustration at times with the state of our apparatus, Moungi convinced me to keep at it, to use the downtime as an opportunity to learn how to build SNSPDs (note: it's complicated), and not to get distracted too much by other projects. This was hard advice to swallow as a rising third-year with no results to speak of, but the persistence paid off. In some ways, I owe this doggedness to my undergraduate advisor and mentor, Stephen Leone and Zhi-Heng Loh, two people who live and breathe difficult experiments.

I had the distinct privilege of critically discussing my thesis work with my committee - Keith Nelson, Sylvia Ceyer, and Troy Van Voorhis - from the very beginning. As someone once told me before my candidacy exam, how often do you have three MIT faculty as interested in your science as you are? Keith, serving as an official co-advisor, was especially kind to let me pursue my single-molecule interests without so much as a whisper of "terahertz" - thank you, Keith, for giving me this freedom but still making me feel welcome in your group. I would like to thank Marc Baldo for his constant support throughout my time at MIT, and for placing an incredible amount of trust in the graduate students and postdocs that comprise the Center for Excitonics. Gleb Akselrod, Geoffrey Supran, Yasu Shirasaki, Shane Yost, Dörthe Eisele, and Joel Yuen-Zhou were part of this cohort, and I enjoyed working alongside them.

Gautham Nair was my mentor when I first joined the group - two Indians, raised in foreign lands, educated in equally foreign countries...um, twinsies! He taught me everything there is to know about nanocrystals and olympic weightlifting, passions we still share. Lisa Marshall, Brian Walker, Peter Allen, Scott Geyer, Wen Liu and Hee-Sun Han were senior students who set the tone of the lab; together, they convinced me that productivity and fun were not mutually exclusive. Jian Cui, Darcy Wanger, and Jungmin Lee were my fellow Bawendi classmates, and I have thoroughly enjoyed my interactions with all three of them. Jian and I spent many nights doing battle with single-mode fiber alignment, with Efros' CdSe band-edge exciton paper, and with the Boston social scene. In all three cases, we got our ass handed to us. As we move on, the lab is left in the capable hands of younger students, whose work I eagerly look forward to reading. Li Miao is a quiet force for good, helping us navigate the sea of bureaucracy so that we could focus on research instead of reimbursement.

I am indebted to my SNSPD collaborators, initially at MIT (Karl Berggren, Francesco Marsili, Vikas Anant, Faraz Najafi, Xiaolong Hu) and now at Lincoln

Laboratory (Eric Dauler, Danna Rosenberg, Jamie Kerman, Athena Pan). I learned a tremendous amount from all of them, from low-temperature engineering to electrical ground-loop management (there's always one..). I have appreciated their skeptical gaze on these silly, blinking emitters that are completely impractical for optical communication. I hope our initial studies will inspire even more sophisticated experiments, and with the apparatus left in the capable hands of Thomas Bischof, this is almost a certainty. Special thanks to Dan Harris, Ou Chen, and the PbS scale-up team for providing the nanocrystals studied in this thesis - I sometimes forget how important your role is to the success of Bawendi group spectroscopy.

Life in graduate school would have been a lot more boring had it not been for my closest friends (you know who you are). Game nights, zombies, Thursdays at the Middlesex, Arrested Development marathons, running 200 miles from mountain to beach - these are my fondest memories of Boston. The Kadambi's and the Fernandes' provided homes away from home when I missed my own family, and I thank them for that. My girlfriend Aditi tended to my soul where no-one else dared tread, and I look forward to seeing what the future holds for the both of us.

Finally, I thank my parents and my brother, who have been my personal cheerleading squad of three - none of this would have happened without your love, support, and pictures of bears.

Contents

Chapter 1

Introduction

Our continued understanding of nature is intimately linked to the measurements we can make to probe its inner workings. Extending our reach across time and space, from the ultrafast to the nanoscale, has forced us to acknowledge that discovery does not saturate - rather, it evolves in sync with the contents of our scientific toolbox. Moreover, combining the strengths of individual fields often allows one to answer fundamental questions that could not even be asked previously. It is our hope that the work contained in this thesis in some small way succeeds at this task.

Over the past thirty years, colloidal semiconductor nanocrystal quantum dots (NCs) have evolved from a scientific curiosity to a robust material system, well-suited to the demands of bioimaging [114], solid-state lighting [128], and display technology [63]. These gains have mostly been realized for nanocrystals composed of cadmium selenide (CdSe), whose range of optical activity spans the visible portion of the electromagnetic spectrum. As a result CdSe NCs have become the workhorse of nanocrystal physics, creating a detailed picture of how excitations behave and interact with one another when confined to nanometer-sized 'boxes'. A revolution was sparked when scientists first began to interrogate CdSe nanocrystals one at a time [98] - this experiment and ones that soon followed [30, 31, 97, 89] unveiled new and unexpected phenomena that was at once complex and compelling.

While visible-emitting nanocrystals continue to hold center stage in the practical applicability arena, a new hotbed of research is developing for materials with opti-

cal activity in the shortwave-infrared (SWIR, λ = 1-3 μm). This has largely been fueled by the promise of solution-processable photovoltaics that are cost-effective from a manufacturing perspective. Colloidal nanocrystals synthesized from the lead chalcogenides (PbS, PbSe, PbTe) and indium pnictogenides (InAs, InSb) have exotic physical properties that in theory could be exploited in SWIR optoelectronics, but our rudimentary understanding of fundamental SWIR-nanocrystal optical properties precludes the rational design of high-efficiency functioning devices as we might do with CdSe.

This thesis explores a new wavelength regime in optical microscopy, and details our investigations of two prototypical SWIR nanomaterials at the single particle level. To place our results in the right context, we equip the reader with the language and relevant physics of semiconductors in the following section. Having familiarized them, we then introduce the concept of quantum confinement as one finds in a nanometer-sized semiconductor nanocrystal, closely paying attention to the species we are most concerned with: excitons. We recount a few seminal experiments in single-NC spectroscopy towards the end, and hopefully launch the now-invigorated reader into the details of our work.

1.1 Bulk semiconductor crystals

The optical and electronic properties of nanocrystals are of interest to us precisely because they are unique from the bulk. However, the language we use to describe these properties, especially that of excitons, is rooted in the physics of three-dimensional solids (nanocrystals are commonly thought of as 'zero-dimensional' solids). In fact, correlating our observations from the bulk to the nanoscale is a worthwhile exercise, and provides a level of understanding that is most helpful.

1.1.1 Energy bands and effective mass

The electronic structure of semiconductors is of primary importance and defines the interaction between photons, electrons, and holes. Each of the constituent atoms in

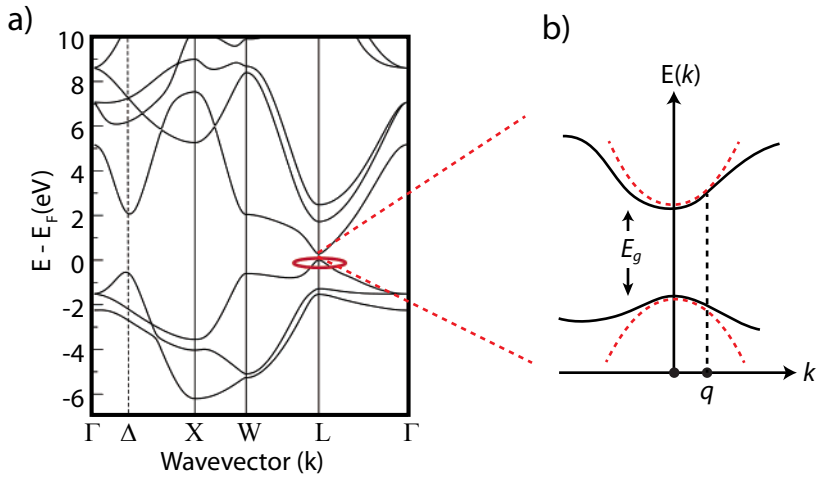

Figure 1-1: a) Calculated dispersion relation for PbSe. The band gap is at the L point (red circle) b) In the effective-mass approximation, the conduction and valence band extrema can be represented by parabolas for small $|k - q|$.

the lattice has a defined number of electron states, the number of which is conserved as the atoms are brought together to form a solid. To a chemist this concept is intuitive, since this is precisely the case in the formation of diatomic molecules. However in solids, the number of atoms is large, resulting not in discrete molecular orbitals but in energy bands. The energy band diagram, or E-k dispersion relation, can be found using a variety of methods, but the simplest uses an electronic wavefunction of the form

$$\Psi(\mathbf{k}, \mathbf{r}) = U_b(\mathbf{k}, \mathbf{r}) e^{i\mathbf{k}\cdot\mathbf{r}} \tag{1.1}$$

where U_b is a Bloch function that assumes the periodicity of the semiconductor atomic lattice. This was the remarkable insight of Felix Bloch who determined that electrons in a solid are similar to free electrons but with a periodic modulation adopted from the lattice [2]. Solving the Schrödinger equation $\hat{H}\Psi = E\Psi$ with a wavefunction of the form above produces a band diagram like the one shown in Figure 1-1a. For a semiconductor, the resulting dispersion relation contains a zone of forbidden energies, the spread of which defines the band gap $E_c - E_v = E_g$. In the language of chemistry, the highest occupied bonding state (HOMO) is the top of the valence band E_v, and the lowest unoccupied antibonding state (LUMO) is the bottom of the conduction band E_c. If we Taylor expand $E(k)$ in this region near the band extrema (Figure

1-1b),

$$E_b(k+q) \approx E_g + \frac{\partial E}{\partial k}q + \frac{1}{2}\frac{\partial^2 E}{\partial k^2}q^2 + \dots \tag{1.2}$$

Using the tools of perturbation theory [2], we can relate the coefficients $\partial E/\partial k$ and $\partial^2 E/\partial k^2$ to important features of the dispersion relation. In particular, the second differential is found to be

$$\frac{\partial^2 E}{\partial k^2} \propto \frac{\hbar^2}{2m} + \left(\frac{1}{q^2}\right)\sum_{b' \neq b} \frac{\left|\langle bk\,|k\cdot p|\,b'k\rangle\right|^2}{\epsilon_{bk} - \epsilon_{b'k}}, \tag{1.3}$$

where m is the mass of an electron in vacuum, p is the electron momentum, and ϵ_{ik} is the energy of the electron state i at position k in the dispersion relation. The second term in Equation 1.3 is a sum over matrix elements that couple nearby electron states ($b \pm 1, 2, \dots$) to the one we are interested in. With a little dimensional analysis, one finds that $\hbar^{-2}\partial^2 E/\partial k^2$ has units of inverse mass, allowing us to recast our Taylor expansion near the band edge as

$$E_b(k) \approx E_g + \frac{\hbar^2 k^2}{2m_{\text{eff}}} \tag{1.4}$$

with

$$m_{\text{eff}} = \left(\frac{1}{2m} + \left(\frac{1}{\hbar^2 q^2}\right)\sum_{b' \neq b} \frac{\left|\langle bk\,|k\cdot p|\,b'k\rangle\right|^2}{\epsilon_{bk} - \epsilon_{b'k}}\right)^{-1}. \tag{1.5}$$

In this 'effective mass approximation', we can think of m_{eff} as a way to lump all the interactions the electron (or hole) feels when it is placed in a solid, rather than an actual physical mass. Now, the broad range of electronic environments for different semiconducting materials can be gauged, albeit crudely, by a single parameter.

1.1.2 Optical absorption and excitons

Having created a framework for how electrons behave in a solid, we now consider their interaction with light. In the process of photon absorption such that an electron is promoted from the valence (VB) to the conduction band (CB), an excited state is produced. The transition probability, and therefore the light absorption intensity,

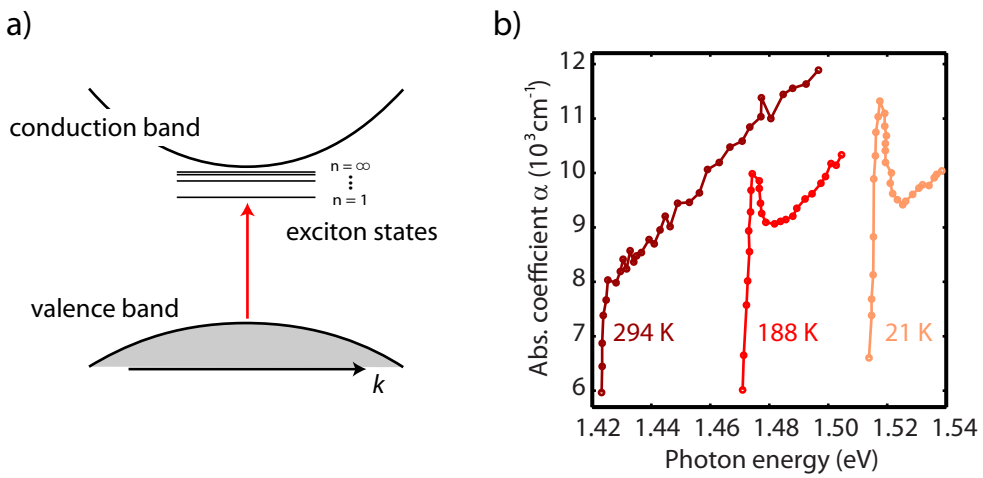

Figure 1-2: a) Promotion of a valence band electron to the $n = 1$ exciton state. The exciton energy level structure near the conduction band is similar to a hydrogen atom. b) Absorption spectra of thin-film GaAs as a function of temperature. In addition to the onset of absorption at the band edge (rising shoulder), a sharp excitonic peak is clearly visible as the temperature is lowered. Figure adapted from [130].

is given by the matrix element $|\langle bk\,|\mu \cdot \mathbf{E}|\,b'k\rangle|^2$. Since μ can be related back to the momentum operator p, one immediately notices the similarity between this quantity and the coupling elements used to calculate the effective mass. Physically, this means that bands which perturb each other strongly are always connected by allowed optical transitions for absorption (or emission) of a photon [65]. In our discussion, we limit ourselves to direct, or vertical transitions for which $k_{\text{electron}} + k_{\text{hole}} \approx 0$.

There is another way to make an excited state [2]. Suppose instead we created a one-electron state in the conduction band that was a superposition of many levels near the CB minimum, forming a localized wavepacket with energy slightly above E_c. Doing the same for the hole states left behind also produces a wavepacket with average energy slightly below E_v - the difference in energy between these two localized states would be slightly larger than the band gap E_g. However, one must take into account the non-negligible Coulombic attraction between the electron and hole; within the effective mass approximation, this can be expressed as

$$H = \frac{p_e^2}{2m_{\text{eff,e}}} + \frac{p_h^2}{2m_{\text{eff,h}}} - \frac{e^2}{4\pi\epsilon\,|\mathbf{r}_e - \mathbf{r}_h|} \tag{1.6}$$

with the Coulomb attraction screened by the dielectric constant ϵ of the semiconductor. If we use a reduced mass instead of the electron and hole effective masses, the Hamiltonian above is remarkably similar to that for the hydrogen atom. This results in a series of Rydberg-like bound states near E_g, which we call *excitons* (Figure 1-2a). Far from a theoretical oddity, evidence for these states can be seen directly in the low-temperature absorption spectrum for most bulk semiconductors (Figure 1-2b). The total exciton wavefunction near $\mathbf{k} = 0$ is

$$\Psi_n(\mathbf{r}) = F_n(\mathbf{r}_e - \mathbf{r}_h)U_c(\mathbf{r}_e)U_v(\mathbf{r}_h) \tag{1.7}$$

where F_n is an envelope function that assumes the shape of hydrogenic wavefunctions with quantum number n (i.e. F_1 produces an s-like envelope, F_2 is p-like, etc), and $U_{c,v}$ are the Bloch functions for the CB and VB extrema. Finally, for the transition probability from the ground state into an exciton state:

$$\left|\langle \Psi_n(\mathbf{r}) \left|p\right| \Psi_0(\mathbf{r})\rangle\right|^2 \approx \left|\langle U_c \left|p\right| U_v\rangle\right|^2 \left|\langle F_n|F_0\rangle\right|^2. \tag{1.8}$$

The electric dipole absorption is thus determined by the symmetry of both the envelope function F and the Bloch functions U - strictly, the envelope function part of Equation 1.8 requires the ground and excited states to have the same symmetry.

1.2 Quantum confinement: nanocrystal quantum dots

In the bulk, adding a Coulombic attraction between an electron and a hole introduces spatial correlation, and produces a natural distance where the kinetic and potential energies are balanced. This length is the exciton Bohr radius $a_B = \frac{4\pi\epsilon\hbar^2}{\mu^* e^2}$, approximately 5 nm in CdSe, 18 nm in PbS, and 36 nm in InAs. An obvious question arises: what happens to the electronic structure when the solid of interest has dimensions on the order of, or smaller than, a_B? To answer this, we follow the same prescription

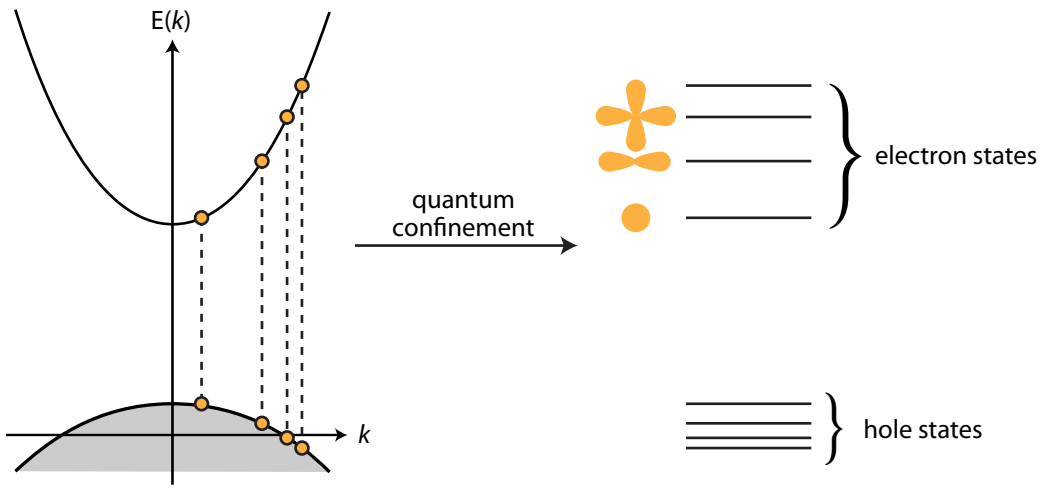

Figure 1-3: Evolution from bulk to quantum-confined electron and hole states. The black dotted lines intersect k at specific points, highlighting the reduced number of wavevectors that are now supported within the confines of a nanocrystal. Here, we assume the hole effective mass is smaller than the electron effective mass, resulting in more closely spaced hole states in the NC. The orange hydrogen-like wavefunction densities reflect the symmetry of electron states.

as we did for the bulk - bringing together a few thousand atoms (instead of the 10^{23} found in 1 cm^3 bulk crystal) and arranging them in a lattice structure identical to their bulk counterpart, new states once again begin to appear due to the overlap between adjacent atomic orbitals. Whereas the surface is neglected in the treatment of bulk electronic properties (since it accounts for a negligible fraction of the overall crystal) the reduced dimensionality of a nanometer-size crystal ('nanocrystal', NC) introduces a dramatic spatial confinement on the internal electrons and holes. Since the number of initial (atomic) and final (NC) states is conserved, the reduced number of atoms results in an electronic structure with a reduced density of states, especially near the band edge. Another way to see the effect of confinement on the electronic structure is with the Hamiltonian itself. Since the kinetic T_{kin} and Coulomb potential V_{coul} energy terms are proportional to $1/r^2$ and $1/r$ respectively, shrinking the size of the crystal to $r \to 0$ results in a Hamiltonian that is dominated by T_{kin}, producing electronic wavefunctions that are similar to particle-in-a-sphere states (Figure 1-3).

Beyond this intuitive picture of quantum confinement, more precise treatments

of nanocrystal electronic structure exist but they are beyond the scope of this introductory chapter. However, we indulge in a few defining characteristics of quantum confinement that bear repeating - we trade detail for understanding, with the hope that our incomplete description spurs the interested reader to the primary literature [27, 28, 100, 67].

1. *The Coulomb interaction is no longer the cause of spatial correlation.* When nanocrystals are synthesized to be much smaller than the bulk exciton Bohr radius a_B, NC electrons and holes no longer 'follow' each other spatially as they would in the bulk since the exciton often delocalizes over the entire NC core. Rather, their correlation in a sense comes from the small volume both carriers are forced to occupy. Mathematically the overall wavefunction can be simplified to reflect this feature: $F_{ex}(\mathbf{r}_e - \mathbf{r}_h) \rightarrow F_e(\mathbf{r}_e)F_h(\mathbf{r}_h)$. Since the absorption of an above-band-gap photon promotes an electron from the valence to the conduction band instead of a Coulombically-bound exciton state, it is somewhat of a misnomer to refer to this excitation as an 'exciton'.

2. *The Coulomb interaction is still large in nanocrystals.* It is common to solve for the eigensystem of nanocrystals by neglecting the Coulomb term, and then adding it's contribution later as a perturbation [17]. However, as was pointed out by Efros, the Coulomb interaction between the optically created electron and hole strongly affects the nanocrystal optical spectra [27]. The attractive potential V_{coul} scales as $1/r$ and in small nanocrystals, Coulomb-mediated processes such as Auger recombination are oftentimes enhanced [93]. Auger recombination is detrimental to the optical activity of semiconductor NCs (both in light emission and photovoltaics) since it is fast exciton-quenching pathway, spurring research to both understand [140, 116, 59] and negate [22, 43, 20] its effects.

3. *The wavevector $\boldsymbol{k}$ is no longer a good quantum number, especially near the band edge.* Having reduced the dimensionality of our solid, it is incorrect to frame the energy structure in terms of E-k dispersion relations, or band diagrams. Instead

of a continuous set of wavevectors, only discrete k are now supported within the confines of the nanocrystal. The eigenspectrum $E = \hbar^2 k^2 / 2m_{\text{eff}}$ reflects this near the band edge. Since the NC states that arise are admixtures of spin ($\vec{S}$), angular ($\vec{L}$) and overall ($\vec{J}$) momentum projections, the quantum number that best describes the state of interest depends on the depth of interactions accounted for. For example, the electron states of CdSe are adequately described by $\vec{L}$ quantum numbers (1S, 1P, 1D), while the hole states require $\vec{J}$ due to nonzero spin-orbit coupling. Away from the band edge, the eigenspectrum is much more dense and resembles the bulk density of states. One should be aware that this transition from discrete to bulk-like is not *that* high in energy, oftentimes just 0.8-1 eV above the band gap.

4. *The exchange interaction is a critical component of NC exciton fine structure.* In general, the total exchange interaction is a combination of both short-range (SR, exponential decay over the length of a lattice constant) and long-range (LR, power law decay over many lattice constants) components [39]. In the effective-mass approximation, the LR contribution is assumed to vanish under certain simplifying conditions, leaving the SR contribution as a perturbation to the overall exciton Hamiltonian. In CdSe, this produces a five-level splitting and the characteristic optically dark exciton ground state which has been experimentally confirmed [28, 99]. However, psuedopotential calculations emphasize the importance of the LR interaction which can be as large as the SR term. In the bulk, the LR term has its origin in dipole-dipole coupling between unit cells, but in NCs it switches to majority monopole-monopole coupling, a uniquely quantum-confined phenomenon [39]. A balanced situation where both the SR and the LR parts contribute to the exchange integral should be the predominating viewpoint, with the total exchange energy as well as the SR component increasing for smaller NC radii [79]. Zunger and co-workers are quick to point out that the degree of wavefunction localization cannot solely explain the SR-LR balance - calculations on epitaxial QDs with a smaller degree of quantum

confinement than colloidal NCs (but made of the same semiconductor material) exhibit significantly larger SR exchange [79].

1.3 Spectroscopy at the nanoscale

It is apparent that the electronic structure of semiconductor nanocrystals is distinct from their bulk counterparts, having seen above the fate of bulk states in the quantum confinement regime [17]. As a result, the optical properties of NCs are significantly modified. A redistribution of bulk oscillator strength towards the lowest exciton state for smaller NCs suggests that spectroscopy near the band-edge will be a powerful tool for observing uniquely nanoscale phenomena.

While nanocrystals have divulged a great deal of information when probed at the ensemble level (most notably, in NC size-dependent PL excitation spectroscopy [101, 5]), interrogating individual nanocrystals one at a time has allowed us to 'see the forest for the trees'. What is intriguing is that single-NC experiments have both reinforced and discounted the full artificial-atom-like picture of the band-edge states - in certain circumstances, it can be treated as an isolated two-level system [15, 4], while in others a more sophisticated approach is needed to explain the data [11, 98, 36].

This thesis is primarily concerned with the optical properties of single nanocrystals in the shortwave-infrared, probing material systems that have to date only been studied at the ensemble level. In this section, we recount a few pioneering experiments conducted on individual CdSe NCs to highlight both the atomic and 'atomic plus' pictures, and set the stage for our own investigations in a previously unexplored wavelength regime.

1.3.1 Nature of the band edge states in nanocrystals

As theory posits, nanocrystal electron states near the band edge are discrete and adopt symmetries according to their angular momentum quantum number $\vec{L}$ [27, 5]. Using a scanning tunneling microscope (STM), Banin and co-workers interrogated individual InAs nanocrystals at low temperature, and experimentally confirmed the atom-like

state sparsity as well as s and p-like symmetries for the electron wavefunction density [4, 6]. On the other hand, single CdSe NC fluorescence measured as a function of applied magnetic field confirmed the complex interaction between electron and hole states that comprise the band edge exciton fine structure [11]; this was in some ways predicated by earlier experiments that probed CdSe dark-bright exciton coupling at the ensemble level [99]. For nanocrystals with a small band gap, strong coupling between the conduction and valence band states is expected, especially in materials where E_g is comparable to the spin-orbit coupling energy (e.g. InSb).

1.3.2 PL intermittency from single NC emitters

In single atoms, it was predicted by Bohr and experimentally confirmed by others that under cw excitation, fluorescence intermittency could occur due to 'quantum jumps' between a bright excited state and a dark metastable state [3]. When the fluorescence from single nanocrystals was first measured, a similar intermittency was observed [98]. One could naively attribute the off state in nanocrystals to a metastable state, say a spin-disallowed one in analogy to the atom picture, but this is erroneous. Instead, detailed fluorescence blinking experiments have implicated carrier trapping, surface ligand rearrangement, Coulomb-enhanced Auger recombination and a host of other mechanisms in switching the nanocrystal off [125, 23, 40]. Each of these mechanisms advance the 'atom plus' viewpoint, requiring direct interaction between the emissive state and its quantum-confined environment. Unfortunately, a model that correctly accounts for all the experimental evidence has yet to be produced, although advances in synthesis have more or less suppressed blinking in CdSe-based NCs [54, 20, 80].

In a similar vein, it came as a surprise that the PL emission linewidth of single CdSe emitters was broader than the lifetime-limited value of a few neV, even at low temperature [30, 32]. The spectral jumps appear to be reversible, implying that irreversible photochemistry is probably not the cause, but instead might be due to a fluctuating charge environment that alters the electronic structure through the Stark effect [34, 82]. Once again, these observations deviate from the isolated atom-like picture.

1.3.3 Multi-exciton quantum yield

As was mentioned above, quantum confinement enhances Coulomb-mediated processes since the interaction scales as $1/r$. If an individual CdSe nanocrystal is doubly excited within the lifetime of the neutral exciton, Auger recombination can efficiently quench the biexciton and leave the single exciton to recombine radiatively. This results in the near-deterministic preparation of a single emitting state - if one was to measure the probability of CdSe two-photon emission as a function of time-delay between subsequent emission events, a dip near time-zero would be observed ('antibunching') [15]. Nair et al. demonstrated that an intimate connection exists between the biexciton quantum yield (η_{BX}) and the extent of antibunching for single nanocrystals [96], making the antibunching experiment a suitable probe for multi-exciton physics at the single NC level. Single molecules [75] and atoms [64] also exhibit strong antibunching but the mechanisms responsible are different.

More recently, synthetic advances have made it possible to tune the Coulomb interaction in nanocrystals [54]. By growing a cadmium sulfide (CdS) shell on a CdSe NC, the band edge electron states delocalize into the shell, thereby reducing the electron-hole overlap. Park et al. recently showed that for thick-shell CdSe/CdS NCs, a broad distribution in η_{BX} can be observed, some as large as 80% [106]. The potential to rationally design systems that exhibit well-defined multiparticle processes is exciting from a fundamental perspective, bringing new physics to light especially at the single nanocrystal level.

1.4 Thesis overview

This introductory chapter has attempted to sufficiently expose the reader to the fundamental properties of colloidal nanocrystals. In particular, it is our hope that a compelling case for extending the power of single NC interrogation to SWIR-active nanocrystals was made. Since optical microscopy plays an integral role in our experiments, Chapter 2 provides a theoretical perspective on the salient features of an imaging system. In there we also detail the experimental realization of our SWIR

microscope, highlighting the unique superconducting nanowire single photon detectors that enabled our investigations. With all the tools on hand, we successfully interrogate single PbS nanocrystals - Chapter 3 describes these results, as well as our ability to perform photon correlation experiments on weak SWIR emitters. In Chapter 4, we use pulsed excitation and study the photophysics of individual InAs/CdZnS nanocrystals, discovering two types of blinking dynamics and extracting the distribution of radiative lifetimes from the studied sample. We switch wavelength regimes in Chapter 5, and investigate single CdSe/CdS nanocrystals that emit in the visible, assessing the prospect of multiple blinking mechanisms in a new generation of CdSe-based nanomaterials. Chapter 6 summarizes our findings across the three NC systems, and provides an outlook on future directions in SWIR-active NC spectroscopy.

Chapter 2

Experimental Methods

In looking for a suitable probe of dynamics at the nanoscale, the scientist is presented with a range of sophisticated experimental tools, each of which has proven its mettle across the fields of chemistry, materials science, physics and biology [21, 91, 136]. This has been especially true of techniques that localize and interrogate single systems, allowing us to study more closely heterogeneous observables rather than just the average. A simple analogy helps motivate why the 'single molecule' scientific approach is a worthwhile endeavor: imagine an alien studying the human species. If, from many miles away, it was to take an average of the entire population, what might it see? The richness of our species, both stark (gender, race, age) and subtle (culture, language) would be completely obscured - humanity's ensemble average looks nothing like the majority of us.

Ever since the first optical detection of single molecules almost 25 years ago [92, 103], fluorescence microscopy has firmly established itself in the scientific toolbox, with a dizzying array of advances aimed at improving resolution [55], signal-to-noise, and importantly, the ability to probe in native environments [83, 88] (arguably, this has as much to do with the advances made in chemically synthesizing photostable fluorescent probes).

The work in this thesis relies heavily on the use of optical microscopes, and the purpose of this chapter is to highlight the essential components of our experimental apparatus. A number of excellent reviews on optical microscopy currently exist

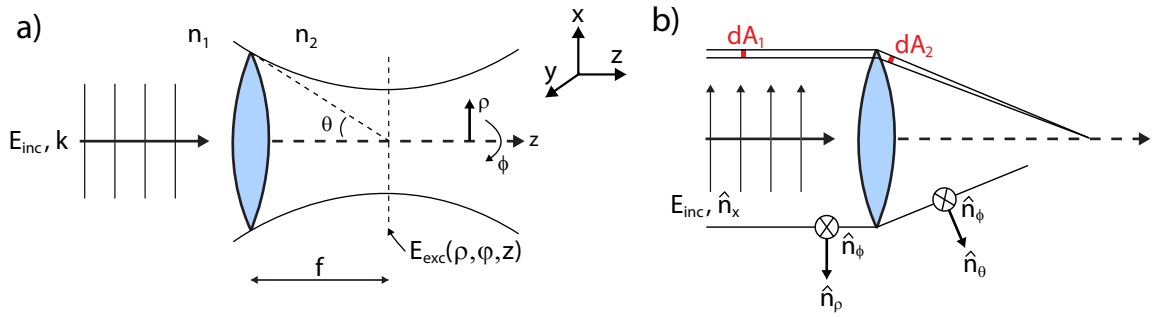

Figure 2-1: a) Focusing a plane wave with a lens. $\mathbf{E}_{\text{inc}}$, plane wave incident on the lens. f, focal length. $\mathbf{E}_{\text{exc}}(\rho, \varphi, z)$, electric field profile in the focal plane. (x,y,z) is the lab coordinate frame, and (ρ, φ, z) is the cylindrical coordinate frame in the focal plane. b) Mapping the coordinate system before and after refraction. dA_1 and dA_2 are areas of constant intensity (see text).

[35, 91, 102]; here, we start with the theory of light microscopy, and end with our experimental realization of a working infrared fluorescence confocal microscope.

2.1 Theoretical underpinnings of light microscopy

In this section, we will attempt to better understand the techniques used in this thesis by placing them in a mathematical framework - in doing so, the salient features of confocal microscopy will be made readily apparent. Extensive primary literature exists, but we will rely heavily on the tools developed in Novotny and Hecht [102].

2.1.1 Focal fields

At the heart of fluorescence microscopy is the principle of refraction, using light and lenses to both excite fluorophores and collect their emission. As is often the case, we want a tightly focused beam and will employ a high-numerical-aperture (NA) lens to produce it - this is depicted schematically in Figure 2-1a. For a monochromatic field $\mathbf{E}_{\text{inc}}$ incident on a perfectly transmissive lens, the field distribution in the focus $\mathbf{E}_{\text{exc}}(\rho, \varphi, z)$ is our target of interest. Separating $\mathbf{E}_{\text{inc}}$ into its s and p polarization components, and mapping (ρ, ϕ) onto the refracted field coordinate system (θ, ϕ)

(Figure 2-1b),

$$\mathbf{E}_{\text{inc}}^{(s)} = [E_{\text{inc}}\mathbf{n}_{\mathbf{x}} \cdot \mathbf{n}_{\phi}] \cdot \mathbf{n}_{\phi} = -E_{\text{inc}}\sin(\phi)\mathbf{n}_{\phi} \tag{2.1}$$

$$\mathbf{E}_{\text{inc}}^{(p)} = [E_{\text{inc}}\mathbf{n}_{\mathbf{x}} \cdot \mathbf{n}_{\rho}] \cdot \mathbf{n}_{\theta} = E_{\text{inc}}\cos(\phi)\mathbf{n}_{\theta} \tag{2.2}$$

with $\mathbf{E}_{\text{inc}}$ polarized along the x axis. The refracted field, which we call $\mathbf{E}_{\infty}$ (the infinity symbol signifies that this field is evaluated far from the focus $(x, y, z) = (0, 0, 0)$, on the lens' reference sphere) must satisfy power conservation. For each ray of area dA,

$$I_{\infty} dA_2 = I_{inc} dA_1 \tag{2.3}$$

$$\frac{1}{2} c n_2 \epsilon_0 \left|\mathbf{E}_{\infty}\right|^2 dA_2 = \frac{1}{2} c n_1 \epsilon_0 \left|\mathbf{E}_{\text{inc}}\right|^2 dA_1 \tag{2.4}$$

$$n_2 \left|\mathbf{E}_{\infty}\right|^2 dA_2 = n_1 \left|\mathbf{E}_{\text{inc}}\right|^2 dA_2 \cos(\theta) \tag{2.5}$$

$$\mathbf{E}_{\infty}(\theta, \phi) = \mathbf{E}_{\text{inc}}(\theta, \phi)(\cos(\phi)\mathbf{n}_{\theta} - \sin(\phi)\mathbf{n}_{\phi})\sqrt{\frac{n_1}{n_2}\cos(\theta)}. \tag{2.6}$$

The incident field impinging on the lens is usually a Gaussian:

$$\mathbf{E}_{\text{inc}}(\theta, \phi) = E_0 e^{-(x_{\infty}^2 + y_{\infty}^2)/w_0^2} = E_0 e^{-\frac{1}{f_0^2}\frac{\sin^2(\theta)}{\sin^2(\theta_{max})}} \tag{2.7}$$

where (x_{∞}, y_{∞}) are the lateral lens coordinates, w_0 is the beam waist, f is the focal length of the lens, and $f_0 = w_0/f\sin(\theta_{\max})$. The final equality in Equation 2.7 defines the incident field in terms of a 'fill factor' f_0; experimentally, this quantity is set by the ratio of the incident beam waist to the back-aperture of the microscope objective (the back-aperture of most high-NA objectives is 5-10 mm in diameter).

Now that we have an expression for $\mathbf{E}_{\infty}$, geometrical optics allows us to calculate the focal field $\mathbf{E}_{\text{exc}}(\rho, \varphi, z)$ directly, and subsequently $|\mathbf{E}_{\text{exc}}(\rho, \varphi, z)|^2$ as a function of the fill factor f_0. This is done using the angular spectrum representation, which relates each ray of the far field $\mathbf{E}_{\infty}$ to a particular plane wave of wavevector $\mathbf{k}$ at the focus. It is this elegant theory that allows us to move seamlessly from $\mathbf{E}_{\infty}$ to $\mathbf{E}_{\text{exc}}(\rho, \varphi, z)$, with the following caveats: 1) we ignore the vector nature of the fields (i.e. $\mathbf{E}_{\text{inc}}$ polarization), and 2) make the paraxial approximation. Following Novotny's

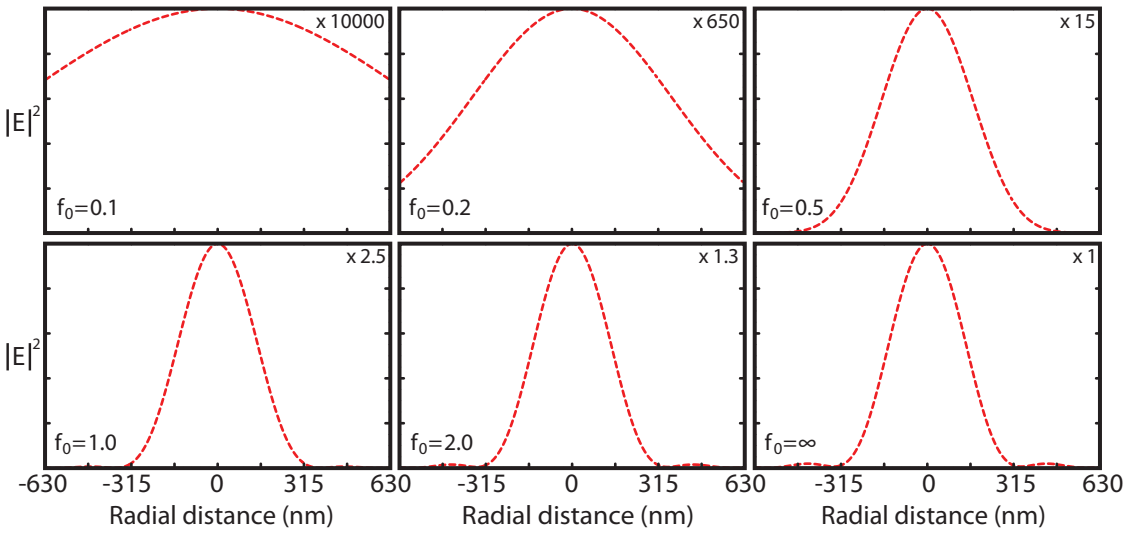

Figure 2-2: Calculated focal intensity profile along the direction of laser polarization, as a function of objective fill factor f_0. As the incident field uses more of the objective NA (i.e. as the fill factor increases), the focused intensity increases while the full width at half-maximum (FWHM) decreases.

methodology [102], we find

$$\mathbf{E}_{\text{exc}}(\rho, \varphi, z) \propto \begin{pmatrix} I_{00} + I_{02}\cos(2\varphi) \\ I_{02}\sin(2\varphi) \\ -2iI_{01}\cos(\varphi) \end{pmatrix} \tag{2.8}$$

where I_{ij} are the integral expressions given in Novotny - they are functions of f_0, NA, and Bessel functions that define the features of $\mathbf{E}_{\text{inc}}$. Taking the modulus squared of Equation 2.8 and setting NA $= 1.4$, $n_2/n_1 = 1.518$, we calculate the focus intensity profile and plot the results for different fill factors f_0 (Figure 2-2. In the limit of $f_0 \to \infty$, $\mathbf{E}_{\text{inc}}$ becomes a plane wave and fully uses the NA of the lens ($\theta_{\max} \approx 68°$), giving the tightest focus. In an actual experiment, a fill factor of approximately one is enough to generate an appropriately focused excitation spot. Novotny includes a full calculation without the paraxial approximation and finds excellent agreement with our approximated result - this suggests that even for a NA $= 1.4$ lens, small angle approximations are still appropriate.

2.1.2 Point-spread function

We will now use our understanding of focal fields to dive deeper into two key concepts in fluorescence microscopy: image formation, and resolution. The quantity that best conveys this connection is the point-spread function (PSF), a measure of the resolving power of an optical system [102]. Physically, the PSF is the measured intensity profile in the image plane for a delta-function emitter in the object plane - the sharper the PSF, the finer the details that can be captured by the imaging system. The PSF can also be cast in the Fourier domain, a composition of spatial frequencies $\mathbf{k}$ that are coupled from the delta-function source to the image plane, with the maximum resolution (smallest PSF full-width-half-maximum) given by the maximum $\mathbf{k}$ transmitted.

Here, we will compare the point-spread function for two excitation scenarios: uniform illumination and focused illumination. In both, a three step prescription is followed: 1) calculation of the excitation PSF, 2) the excitation-dipole interaction, and 3) the detection PSF, given by the response in image space. We assume the source is a dipole aligned along the x-axis and that the paraxial approximation holds ($\theta_{\max} \ll \pi/2$, where NA $= n\sin(\theta_{\max})$), but the results are essentially the same for a full calculation. The excitation and detection point-spread function is well-approximated by the intensity profile in the object and image plane, respectively; the previous section's results will be helpful in this regard.

Wide-field illumination:

The excitation field is a constant E_0 in the object plane - the excitation-dipole interaction is therefore $\boldsymbol{\mu} \propto E_0 \mu_x \mathbf{n}_x$. The radiation emitted from this dipole is collected and eventually focused onto the image plane. As we did before with the excitation focal field, we are now concerned with $\mathbf{E}_{\text{det}}(\rho, \varphi, z)$ in the image plane as this now determines the detection PSF. This can be straightforwardly expressed using the Green's function formalism of Novotny,

$$\mathbf{E}_{\text{det}}(\rho, \varphi, z) = \frac{\omega^2}{\epsilon_0 c^2} \overleftrightarrow{\mathbf{G}}_{\text{PSF}} (\rho, \varphi, z) \cdot \boldsymbol{\mu} \tag{2.9}$$

where ω is the emission frequency, and $\overleftrightarrow{\mathbf{G}}_{\text{PSF}}$ is a Green's function that describes the

entire imaging system, from source to image. In other words, $\overleftrightarrow{\mathbf{G}}_{\mathrm{PSF}}$ tells us how the electric field $\mathbf{E}$ responds to the presence of a source $\boldsymbol{\mu}$, precisely what we are interested in. Making the approximations listed above, and setting $z = 0, \varphi = \pi/2$ (coordinates of the image plane), $\overleftrightarrow{\mathbf{G}}_{\mathrm{PSF}}$ is given by

$$\overleftrightarrow{\mathbf{G}}_{\mathrm{PSF}} \propto \frac{k'}{8\pi i}\frac{f}{f'}e^{i(kf-k'f')}\begin{bmatrix} \tilde{I}_{00} & 0 & 0 \\ 0 & \tilde{I}_{00} & -2i\tilde{I}_{01} \\ 0 & 0 & 0 \end{bmatrix}\sqrt{n}, \tag{2.10}$$

$$\tilde{I}_{00} \propto \int_0^{\theta_{\max}} \theta J_0(k'\rho\theta f/f')\mathrm{d}\theta \tag{2.11}$$

$$\tilde{I}_{01} \propto \int_0^{\theta_{\max}} \theta^2 J_1(k'\rho\theta f/f')\mathrm{d}\theta \tag{2.12}$$

where f/f' is the ratio of object to image focal length, k (k') is the wavevector for a ray through the object (image) plane, n is the index of refraction in the object field, and J_n are Bessel functions of order n. Solving for $|\mathbf{E}^w_{\mathrm{det}}(\rho,\varphi,z)|^2$ gives us the detection PSF in the image plane:

$$|\mathbf{E}^w_{\mathrm{det}}(\rho,\varphi,z)|^2 \propto \frac{\mu_x^2 \mathrm{NA}^4}{n\lambda^6 M^2}\left[\frac{J_1(2\pi\tilde{\rho})}{2\pi\tilde{\rho}}\right]^2, \tilde{\rho} = \frac{\mathrm{NA}\rho}{M\lambda}, M = n\frac{f'}{f} \tag{2.13}$$

where M is the magnification of the imaging system, and λ is the emission wavelength. Since the image plane is where we place our confocal pinhole or point detector, Equation 2.13 is also the overall *wide-field illumination* point-spread function.

Focused excitation:

The excitation field is now a tightly focused Gaussian in the object plane. Fortunately, we already calculated this field profile in Section 2.1.1, and the excitation PSF is simply the square of $\mathbf{E}_{\mathrm{exc}}$. The emitter dipole response $\mu = \mu_x \mathbf{n}_x \cdot \mathbf{E}_{\mathrm{exc}}(\rho,\varphi,z)$ now depends on the excitation focal field which we calculated in Equation 2.8. Assuming

a similarly rigid dipole aligned along the x-axis in the excitation focal plane:

$$\mu \propto \begin{pmatrix} \mu_x(I_{00} + I_{02}\cos(2\varphi_n)) \\ 0 \\ 0 \end{pmatrix}. \tag{2.14}$$

The integral expressions $I_{ij} \approx \tilde{I}_{ij}$ in the small θ limit (paraxial approximation). Plugging this expression into Equation 2.10 and taking the square gives us the detection PSF $\left|\mathbf{E}^f_{\text{det}}(\rho, \varphi, z)\right|^2$:

$$\left|\mathbf{E}^f_{\text{det}}(\rho, \varphi, z)\right|^2 \propto \left(\mu_x \left[\frac{J_1(2\pi\tilde{\rho})}{2\pi\tilde{\rho}}\right]^2\right)^2. \tag{2.15}$$

Once again, the intensity profile in Equation 2.15 is what we measure in the image

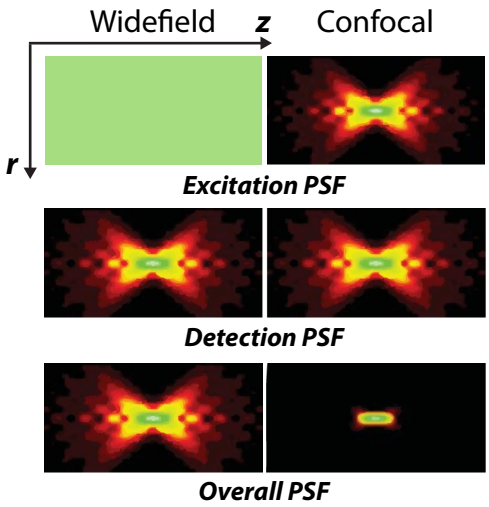

Figure 2-3: Comparison of the excitation, detection and overall point-spread functions at the focus of a high-NA lens for different excitation profiles. A small improvement in the transverse FHWM is obtained for focused excitation, but the real improvement comes in the z-axis. Adapted from Hell and Schönle [52].

plane with our point detector, so this is the overall *focused excitation* point-spread function. Comparing Equation 2.15 with 2.13 is illustrative. By focusing the excitation,

$$\left|\mathbf{E}^f_{\text{det}}(\rho, \varphi, z)\right|^2 = \left(\left|\mathbf{E}^w_{\text{det}}(\rho, \varphi, z)\right|^2\right)^2. \tag{2.16}$$

This results in a slightly smaller overall PSF in the transverse direction - we note however that this improvement is oftentimes just a few percent. This can be seen clearly in Figure 2-3, where the excitation, detection and overall PSFs are plotted for the two situations considered here. More generally, we see that the overall PSF of the system can be approximately regarded as the product of the excitation and detection PSFs (here, the detection PSF is the one given in Equation 2.13):

$$\text{Overall PSF} \approx \text{Excitation PSF} \times \text{Detection PSF}. \tag{2.17}$$

Experimentally the excitation focal field determines the former term, and the spatial filtering done in the image plane (i.e. with a pinhole, small-area avalanche photodiode, or the end of a fiber) controls the latter. This is a very nice result which the microscopist should keep in mind whenever he or she is concerned with resolution.

2.1.3 Emitter radiation profile

Note: this section was produced in collaboration with G. Nair.

The ultimate task in single-molecule spectroscopy is to maximize the signal collected from weakly-emitting species. A single CdSe nanocrystal ($k_{\text{rad}} \approx 40$ MHz) excited at 1 MHz with $\langle n_{\text{ex}} \rangle = 0.1$ excitons on average will emit approximately 100,000 photons per second while it is on, translating to an optical power of about 30-40 fW. This light must be efficiently collected from the emitter and transported to the single-photon detectors used in the experiment. What was shown theoretically in a series of papers by Walter Lukosz and Rino Kunz is that the angular distribution of this emitted power is strongly affected by the presence of a dielectric surface [77, 78, 76] - in our case, this would be the glass coverslip on which the NCs reside. In this section, we investigate three common collection scenarios used in single NC experiments: immersion imaging with an oil objective, air imaging, and through-glass air imaging. We show how the orientation of the dipole alters the emission profile, as well as the total collection efficiency as a function of lens numerical aperture (NA), for these scenarios. The results are general, and are applicable for both visible and

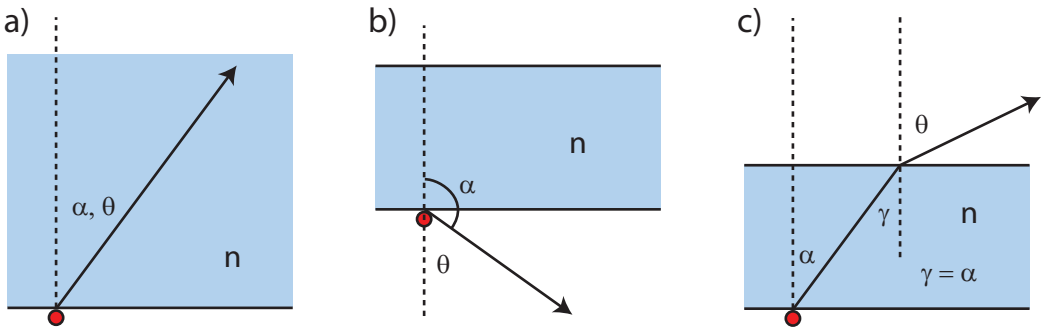

Figure 2-4: Three collection schemes commonly used in single NC experiments. Light is collected in the direction of the vector shown, and the red dot is the dipole emitter. a) Immersion imaging, typically with an oil that index-matches both the coverslip and objective glass ($n = 1.515$). b) Air imaging, such as that usually done in low-temperature experiments. b) Back-side air imaging, with the coverslip flipped and light collected through the glass, but without an immersion oil. n is the index of refraction, θ is the collection angle, and α is the ray angle with respect to the z optical axis.

SWIR emitters.

General setup of the problem

The three scenarios we will investigate are depicted in Figure 2-4. The origin is at the glass-air interface, with positive z pointing upwards ($\alpha = 0$). In general, the dipole emitter resides a distance $d \ll \lambda_{\text{em}}$ from the interface between the glass substrate of index n and air (or vacuum), and is circularly symmetric (no ϕ dependence). In the case of a colloidal NC, d will be on the order of 1-2 nm, given by the surface ligand length. The power $\mathrm{d}L$ emitted into a solid angle $\mathrm{d}\Omega_\alpha$ is

$$\mathrm{d}L = P_{\text{emit}}(\alpha)\mathrm{d}\Omega_\alpha = P_{\text{emit}}(\alpha)\sin(\alpha)\mathrm{d}\alpha\mathrm{d}\phi \tag{2.18}$$

where $P_{\text{emit}}(\alpha)$ is the angular emission power distribution for the dipole. In a homogeneous environment, $P^{\perp}_{\text{emit}}(\alpha) = 3/8\pi\sin^2(\alpha)$, producing the familiar donut profile. $P^{\parallel}_{emit}(\alpha) = 0$ since no power is radiated in the direction of dipole oscillation [56]. The power $\mathrm{d}L$ collected by the microscope objective, whose angle of collection is defined by θ, is also given by $\mathrm{d}L = P_{\text{coll}}(\alpha)\sin(\theta)\mathrm{d}\theta\mathrm{d}\phi$. Therefore, the emitted power that is

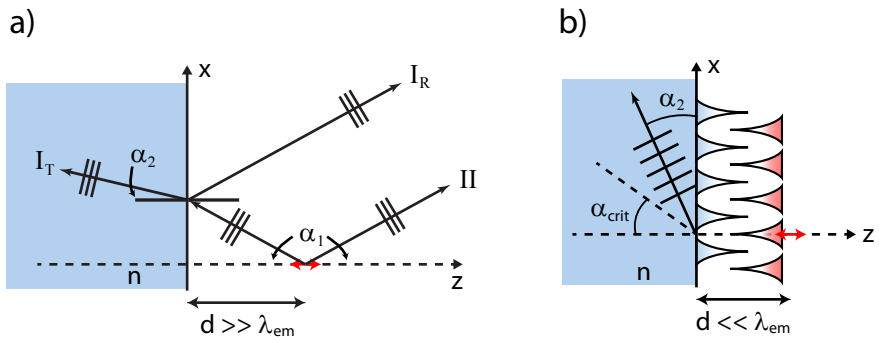

Figure 2-5: a) Dipole (red) placed far away from the interface. Interference between rays I_R and II will determine power in the +z direction, while reflection and Snell's law will determine the angular distribution α_2 into the glass (-z direction). b) Dipole in close proximity to the interface. Evanescent waves of the dipole transmit as power-carrying waves at refraction angles $\alpha_2 > \alpha_{\text{crit}}$. Figure adapted from Ref. [77].

collected by the objective is

$$P_{\text{coll}}(\theta) = T(\gamma) P_{\text{emit}}(\alpha) \frac{\sin(\alpha)}{\sin(\theta)} \frac{\mathrm{d}\alpha}{\mathrm{d}\theta} \tag{2.19}$$

with a transmission coefficient T to account for the air-glass interface in back-side air imaging (Figure 2-4c). In general T will be different for s and p polarized light, so P_{coll} should be calculated for each polarization component separately, and then summed.

Emitted power distributions, P_{emit}

The electric field produced by an oscillating dipole can be separated into two zones of interest: the near-field ($d \ll \lambda_{\text{em}}$) and the far-field ($d > \lambda$em). In a homogeneous environment, the electric field in the near-field is static and cannot radiate power - the emitted power P(emit) is fully determined by the far-field (see Jackson [56], Chapter 9 for an in-depth discussion). This would be the case if our emitter of interest was placed far away from the glass-air interface; the power collected in the direction of the objective would be determined by a mixture of constructive/destructive interference as well as reflection losses. This is schematically depicted in Figure 2-5a. The rays incident on the interface are subject to Snell's law and cannot refract beyond $\alpha_{\text{crit}} =$

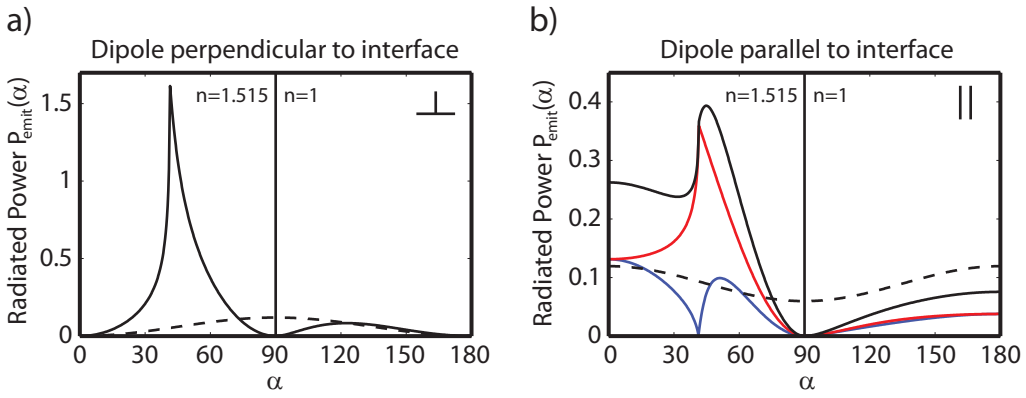

Figure 2-6: Radiation power P_{emit} for a dipole at an air-glass interface. a) Dipole oriented perpendicular to the optical axis z. b) Dipole oriented parallel to the optical axis. A dramatic difference in radiation patterns is apparent between the total interface-dipole power (black solid line) and the dipole in a homogeneous environment (black dashed line). s and p components of the total parallel power are shown in red and blue, respectively. The emitted power density can be calculated by multiplying these functions by $\sin(\alpha)$.

$\sin^{-1}(1/n)$, where α_{crit} is the critical angle beyond which total internal reflection occurs.

The situation is dramatically different once the dipole emitter is in close proximity to the interface, such that the near-field evanescent modes can couple to those of the substrate (Figure 2-5b). Now, in addition to the transmitted power mentioned above, the dipole evanescent waves provide an additional contribution to the power transported into the far-field! In other words, the dipole's evanescent modes are converted into power-carrying modes in the substrate at angles $\alpha > \alpha_{\text{crit}}$ - this is an important result, and is the fundamental cause for increased collection efficiency in immersion imaging. Using the analytical results of Lukosz for $P^{\perp}_{\text{emit}}$, $P^{\parallel(s)}_{\text{emit}}$ and $P^{\parallel(p)}_{\text{emit}}$ [77], we calculate the angular radiation pattern for an emitter at an air-glass interface ($n = 1.515$) and plot the radiated power in Figure 2-6. Two important features are immediately apparent:

1. Integrating P_{emit} from $\alpha = 0 \rightarrow 90°$ shows that most of the power is radiated into the glass (specifically, 86% and 84% for perpendicular and parallel dipoles, respectively).

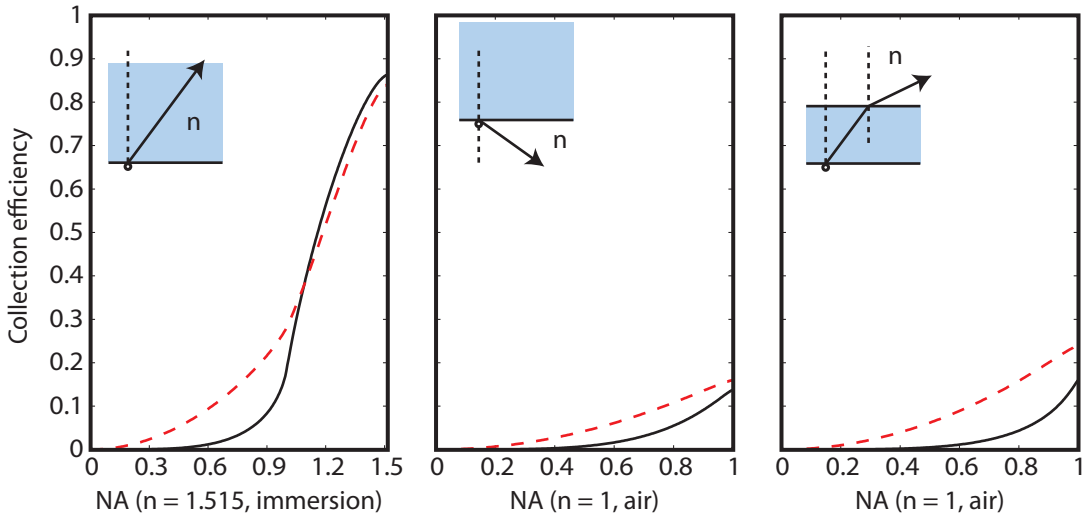

Figure 2-7: Collection efficiency as a function of NA for the three scenarios commonly used in single nanocrystal spectroscopy. The x-axes are chosen based on the highest possible NA lens available for that collection scenario (left figure: oil-immersion objective, middle and right figures: air objective) The case is clearly made for immersion imaging, with $> 80\%$ of the emitted light captured if a high-NA objective is used. The solid black (dashed red) line is for a dipole oriented perpendicular (parallel) to the observation plane.

2. The emission into the glass is concentrated near the critical angle $\alpha_{\text{crit}} = 41°$. In fact, 79% (perpendicular dipole) and 66% (parallel) of the light emitted into the glass propagates above the critical angle.

Collection efficiency

With the expressions for $P_{\text{emit}}(\alpha)$, we can determine $P_{\text{coll}}(\theta)$ and integrate over the range $[-\theta_{\text{max}}, \theta_{\text{max}}]$ of collection angles set by the objective numerical aperture (NA). For the three cases:

1. ***Immersion imaging:*** $\alpha = \theta$. There is no dielectric interface, so $T = 1$. $P_{\text{coll}} = P_{\text{emit}}$.

2. ***Air imaging:*** $\alpha = \pi - \theta$ since emission is collected in the -z direction. Similarly no interface, so $T = 1$. $P_{\text{coll}}(\theta) = P_{\text{emit}}(\pi - \alpha)$.

3. ***Through-glass air imaging:*** The dipole emits into the glass like the im-

mersion case, except now the top glass-air interface refracts rays according to Snell's law. So $n\sin\gamma = n\sin\alpha = \sin\theta$, giving

$$\frac{\mathrm{d}\alpha}{\mathrm{d}\theta} = \frac{\cos\theta}{n\cos\alpha}. \tag{2.20}$$

$T = T(\alpha)$ and can be determined from the Fresnel equations. Therefore,

$$P_{\mathrm{coll}}(\theta) = P_{\mathrm{emit}}(\alpha)T(\alpha)\frac{\cos\theta}{n^2\cos(\alpha)}. \tag{2.21}$$

We plot P_{coll} as a function of NA for these three scenarios in Figure 2-7. Here, efficiency is defined as the ratio of power emitted into the angle subtended by the collection objective to the total emitted power, i.e.

$$\text{Coll. efficiency} = \int_0^{\theta_{\max}} \mathrm{d}\theta\sin(\alpha)P_{\mathrm{coll}}(\theta) / \int_0^{\pi} \mathrm{d}\theta\sin(\alpha)P_{\mathrm{emit}}(\alpha). \tag{2.22}$$

Comparing the three plots, the case is clearly made for immersion imaging - almost 85% of the light is extracted from the emitter if an NA = 1.4 objective is used. This is a common lens and is widely used by us in the visible. Accessing the near-field modes of the dipole is critical to improving the overall signal of the experiment, especially if the emitter radiative rate is slow due to intrinsic material properties.

2.2 Experimental realization of SWIR microscopy

Having discussed the theoretical aspects of microscopy in the previous section, we now turn to our experimental implementation of SWIR microscopy. We highlight the salient features of the setup (collection and detection methodology), and discuss the challenges inherent to pursuing single-molecule investigations under ambient conditions.

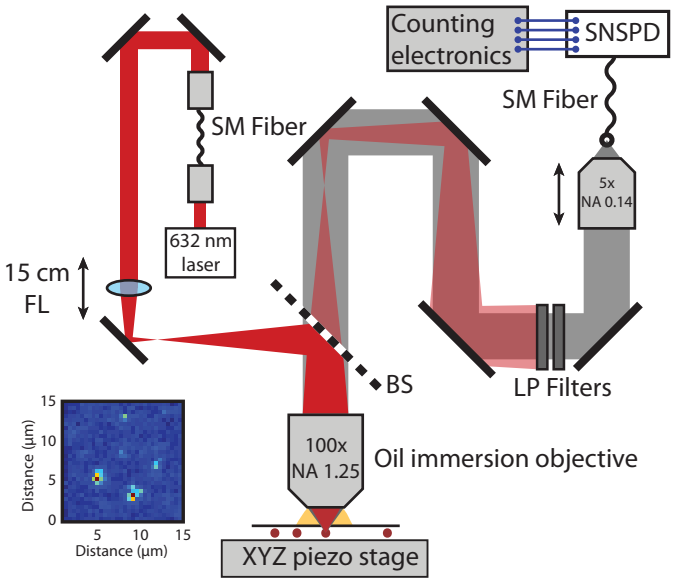

Figure 2-8: Schematic of the sample-scanned SWIR confocal microscope used in this thesis. A 15 cm focusing lens (FL) is used to correct for the chromatic aberration between excitation and emission wavelengths in the focal plane of the immersion objective. Light is collected after the beamsplitter (BS), passed through two > 700 nm longpass (LP) filters, and focused onto the core of a 1500 single-mode (SM) fiber. Photons are detected by the four-channel superconducting nanowire single photon detector (SNSPD). Inset is a raster scan of a dilute InAs NC sample. Excitation is shown in red, and emission in grey.

2.2.1 Collection: the SWIR microscope

Measuring the fluorescent optical properties of an individual nano-object is demanding, but technological advances in photon-counting hardware and high-quality objectives have made the task somewhat routine in the visible. However, the shortwave-infrared portion of the spectrum (SWIR, $\lambda = 1 - 3\mu m$) has yet to fully experience these gains and sensitive measurements in this wavelength regime are limited in scope because of this [29]. The recent surge of interest in experimental quantum information and communication over the last two decades has begun to bridge the gap, at least on the detection front [49].

To interrogate single SWIR-emitting nanocrystals, we built a custom sample-scanned optical microscope as shown in Figure 2-8. Given the potentially low signal-to-noise, silver-coated mirrors were used for the excitation path and gold-coated mirrors for reflecting the emission. Initially, an uncoated 2-inch pellicle (Thorlabs, 90% T, 10% R) was used as the beamsplitter (BS), but this was switched to a dichroic (Thorlabs, DMLP900L) due to airflow issues in the laboratory that distorted the pellicle. The excitation was either a 632 nm cw HeNe laser or a 633 nm pulsed diode laser with variable repetition rate (Picoquant, LDH-P-635). We filtered both excitation sources through a 633 nm single-mode fiber (Thorlabs, P1-630A-FC) to generate a clean TEM_{00} beam profile prior to entering the SWIR microscope. An infinity-corrected achromatic air objective (Mitutoyo Plan Apo NIR, 5× magnification, NA = 0.14) with high transmission in the SWIR was used to focus the excitation onto the entrance of a 1260-1620 nm single-mode fiber (Thorlabs, P1-SMF28E-FC). It is important that the NA of the detection objective and fiber are matched, as well as the emission beam diameter to the back aperture of the detection objective, to ensure maximum coupling from free-space into the fiber core.

As we saw in Figures 2-3 and 2-7, the collection objective plays a critical role in the success of single-molecule experiments. While readily available in the visible, commercial immersion objectives that are chromatically corrected from 600-1500 nm are not available. That is, the excitation- and emission-wavelength focal planes are

displaced from each other along the optical axis when the field incident on the back aperture is collimated. In principle, we could minimize the extent of aberration by exciting at an energy closer to the NC band gap, but the low absorption cross-section of 1200-nm-emitting PbS nanocrystals in this region ($r \approx 2$ nm) restricted us to visible excitation.

If we treat the immersion objective as a simple lens, one can correct for the $\Delta z_{\text{focal}} = f_{1550} - f_{633}$ by introducing a defocusing lens in the excitation path. We determined f_{632} and f_{1550} by carefully measuring the retroreflected 633 nm and 1550 nm power through our candidate immersion objective (Nikon, 100× magnification, NA = 1.25) off a gold-coated microscope coverslip, optimizing for the maximum power. Once we determined $\Delta z_{\text{focal}} \approx 18 - 20\mu m$, we used the thin lens equation $z_o^{-1} + z_i^{-1} = f_{633}^{-1}$ to determine where the defocusing lens focal plane needed to be (z_o^{-1}):

$$\frac{1}{z_i} + \frac{1}{z_o} = \frac{1}{f_{633}} \tag{2.23}$$

$$z_i = \left(\frac{1}{2 \text{ mm}} - \frac{1}{2 + \Delta z_{\text{focal}} \text{ mm}} \right)^{-1} \tag{2.24}$$

$$\Rightarrow z_i \approx 202 - 224 \text{ mm}. \tag{2.25}$$

Since it is important that the back aperture of the immersion objective be filled to fully utilize the NA (Figure 2-2), we chose a 15 cm convex lens and adjusted its z_o^{-1} position along an optical rail. There is certainly some trial-and-error involved in this step since in principle z_o^{-1} depends on the emission wavelength, but we found that there was enough tolerance in the optical system that major adjustment from NC-to-NC was not required.

2.2.2 Detection: single photons in the shortwave-infrared

An ideal single-photon detector, at any wavelength, would satisfy the following conditions: a 100% probability that an incident photon is detected (detection efficiency, d.e.), zero detector 'clicks' in the absence of incident photons (dark-count rate, DCR),

instant detector recovery after recording an incident photon (dead time), zero temporal variation between photon detection and electrical output response (timing jitter), energy resolution, and the ability to count the number of photons in an incident pulse [29]. In reality, trade-offs between these parameters are made in accordance with the needs of the experiment at hand. In single-molecule spectroscopy, a high d.e. and low DCR are prized above all - if time-resolved dynamics are of interest, then detector timing jitter is important too. Here, we review a few competing technologies for single photon detection in the shortwave-infrared, and highlight their overall 'usefulness' to a microscopist using the three critical features listed above.

The most obvious choice for SWIR photon detection would be an avalanche photodiode (APD) fabricated from a semiconductor that can absorb $1 - 3\mu$m light - silicon APDs are currently the champion detectors in the visible. Indium gallium arsenide (InGaAs) and germanium (Ge) are candidate materials and have been used successfully to study individual epitaxial quantum dots [142], but current implementations produce too high a DCR to make ambient single-molecule experiments feasible [112]. Another option relying on conventional technology is frequency upconversion, whereby SWIR light is shifted into the visible and detected using high-efficiency silicon APDs [113]. This is only feasible for narrow-band sources like epitaxial quantum dots due to limited phase-matching bandwidth within the non-linear medium (typically a periodically poled $LiNbO_3$ waveguide); at room temperature, a CdSe colloidal nanocrystal has a 20-30 nm emission FWHM, and this is quite likely broader for PbS and other SWIR materials. In parallel, a new detection methodology based on superconductivity in niobium nitride (NbN) nanowires was proposed and experimentally realized by Gol'tsman et al. in 2001 [44]. Spurred on by the demands of optical communication and quantum information, these superconducting nanowire single photon detectors (SNSPDs) have demonstrated $> 60\%$ system detection efficiency (from input to detection), sub-kHz DCR and 50 ps timing jitter, making them the superior method for detecting weak SWIR emission. Recently, a tungsten silicide transition-edge sensor based on an SNSPD design was fabricated and exhibited 93% d.e. with low DCR and small timing jitter [84], but the system needed to be cooled to sub-

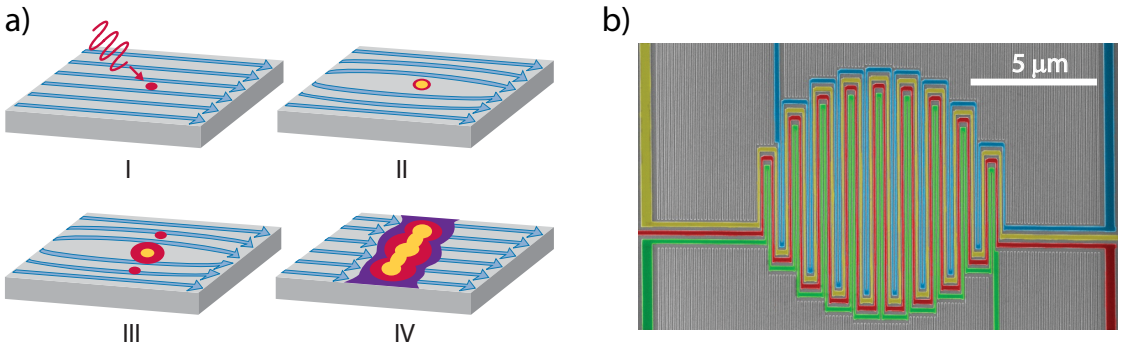

Figure 2-9: a) A phenomenological model for SNSPD operation: (I) photon absorption by a superconducting nanowire biased near the critical current I_{crit}. (II) Creation of a small resistive hotspot, forcing the supercurrent (blue arrows) to flow along the periphery. (III) The hotspot grows quickly, increasing the local current density around the hotspot above I_{crit}. (IV) Eventually, the hotspot spans the width of the nanowire (< 100 nm) and blocks current flow, transiently switching off superconductivity in the detector and producing an electrical 'click' that can be counted. b) False-color SEM image of a representative 4-channel interleaved SNSPD. Each color indicates a uniquely biased nanowire, acting as an independent detector. Figure a) from Ref. [61], Figure b) courtesy of E. A. Dauler.

Kelvin temperatures for optimum operation. The difficulties inherent in operating a detector at 100 mK, even for a specialist, makes this system a daunting prospect.

2.2.3 Superconducting nanowire single photon detectors

For the SWIR portion of this thesis, we used highly efficient SNSPDs fabricated by Lincoln Laboratory to detect our weak NC luminescence. Here, we briefly outline our current understanding of their operation, and make a few observations concerning the implementation of these detectors for confocal microscopy.

While a comprehensive understanding of detector operation still eludes the SNSPD community, a working phenomenological model has been proposed by a few groups including the MIT-Lincoln Laboratory collaboration [44, 62]. Upon cryogenically cooling the NbN nanowire to ca. 2.5 K the detector becomes superconducting. The nanowire is biased near its critical current I_{crit}, above which the nanowire switches to a normal metal conducting state. When a photon impinges on the nanowire, a small resistive hotspot is formed which rapidly grows to span the width (< 100 nm). This

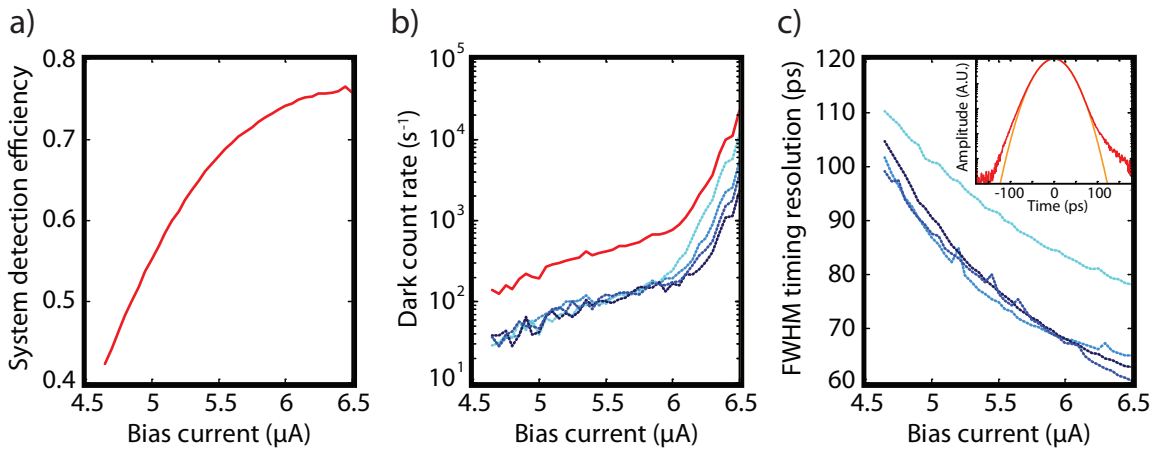

Figure 2-10: Detector parameters as a function of bias current. a) Total system detection efficiency, summed across all four SNSPD channels (variation between channels is minimal). b) Dark count rate for individual (dotted blue lines) and the sum (solid red line) of the four channels. c) Full-width-half-maximum timing resolution for each channel. Inset is the experimentally measured jitter (red) and fit (orange) time for one of the channels. Figure adapted from [117].

forces the supercurrent to 'bunch' near the periphery of the hotspot until eventually I_{crit} is exceeded, instantly switching the nanowire to the normal state. Eventually (within a few ns, for our SNSPD) the nanowire dissipates the thermal load, and resets back to the superconducting state. The transient change from essentially zero to some finite resistance is measured by an external readout circuit, providing us with a suitable way to count photon detection events. This mechanism is depicted schematically in Figure 2-9a.

In our experiments, we use a 4-channel interleaved SNSPD and operate with a total system detection efficiency of ca. 60% at 1550 nm and sub-kHz DCR across all four channels (Figure 2-10a-c, [117]). The detector chip looks similar to that in Figure 2-9b - the chip is placed in a Gifford-McMahon closed-loop cryocooler with optical access provided by a single-mode fiber. The advantage of the interleaved detector is that a beamsplitter is not required for correlation experiments, a key measurement we pursue in later chapters, since the signal photon's spatial mode overlaps with all four detectors yet only one can absorb it. Each nanowire is biased independently, with minimal crosstalk between adjacent nanowires.

A few drawbacks exist when coupling the SWIR microscope to SNSPDs. First,

as we saw in Figure 2-6 the radiated power from a single nanocrystal at the glass/air interface is concentrated near the critical angle α_{crit}. This means that the emission spatial mode we eventually focus onto the single-mode detection fiber is not Gaussian, but more like a ring [70]. We believe this to be the cause of fairly large signal loss at the objective-fiber interface, since only a fraction of this shaped emission light is likely to enter the TEM_{00} allowed fiber mode. Switching to a multi-mode fiber would mediate this problem somewhat, however the larger number of accepted modes would also result in a higher DCR due to blackbody radiation coupling into the detection fiber. Second, single NC experiments often monitor the PL intensity as a function of time as a way to probe the statistics of fluorescence intermittency (see Chapter 3). Since the emission intensity is likely to fluctuate with time, the SNSPD d.e. must remain constant with time so that any variations can be attributed to the NC. However, other groups report that Gifford-McMahon-cooled SNSPDs experience a slow 1-2 Hz temperature variation due to the pumping of helium through the cooling system, resulting in an oscillating count rate [126]. We found that this behavior was current bias-dependent, i.e. if we set the detector bias too close to I_{crit} the 2 Hz oscillation would appear in our intensity trace. In our NC experiments, we set the bias just below the threshold for 2 Hz noise, and still operate with ca. 60% d.e.

Chapter 3

Continuous-wave exciton dynamics in single PbS nanocrystals

When a semiconductor nanocrystal (NC) is optically excited with energy $E > E_g$, an electron-hole pair is instantaneously created and delocalizes within the confines of the NC. This excited species - a hot exciton - undergoes a flurry of activity as it relaxes to the band edge before finally recombining radiatively or nonradiatively. What has captivated a legion of scientists, ever since the first interrogation of single NCs [98], is the precise nature of this activity prior to recombination; it plays a critical role in determining whether fluorescence is produced or not [59]. The stochastic switching between a radiative on state and a non-radiative off state, colloquially termed 'blinking', is probably the most striking example of the complexity contained within the exciton lifecycle and has been studied extensively in visible-emitting systems [54, 23, 125, 115].

Light emission is a fitting probe of nanoscale exciton dynamics: as revealed in single cadmium selenide (CdSe) NC fluorescence studies [68, 123, 11, 106], much can be learned about the microscopic phenomena governing recombination of ground-state and highly-excited excitons. However, very little is known about the optical properties of single SWIR-active colloidal NCs ($E_g \approx 0.6-1.2$ eV) such as the lead chalcogenides (PbX, X = S, Se). Exotic phenomena that occur in PbX NCs like the process of carrier multiplication [94, 87], or the remarkably slow rate of radiative recombination [121],

would be better understood if probed beyond the ensemble average.

Previous attempts have been made by others to localize and study the luminescence from individual SWIR-emitting nanocrystals, but conventional single-photon detector technologies do not have the sensitivity to measure their weak emission with adequate signal to noise [49]. For example, the authors of Ref. [112] attempted single PbS NC spectroscopy with InGaAs avalanche photodiodes but were unable to locate individual nanocrystals, concluding that their approach was insufficient given the prohibitively large background detector noise and low detection quantum efficiency. Another recent experiment utilized frequency upconversion to detect single 1300-nm-wavelength photons from self-assembled epitaxial quantum dots (SAQDs) by shifting them into the visible, but limited phase-matching bandwidth in the nonlinear medium restricts the applicability to narrow linewidth systems [113]. Direct SWIR photon detection with SNSPDs, the detector of our choice, circumvents this problem and has been used in the past to study the optical properties of SAQDs, as well as single plasmon excitations in gold waveguides [142, 50, 135]. In these reports, the low system detection efficiency (ca. 5-10%) of the SNSPD was compensated for by the extreme photostability and fast radiative rate of the SAQD emitter, providing an adequate signal to noise ratio to perform sophisticated correlation experiments. Infrared colloidal nanocrystals on the other hand produce a lower emission photon flux compared to their epitaxial counterparts; the excitation pumping rate is usually much higher for SAQDs due to the larger absorption cross-section when excited nonresonantly, as is the single exciton radiative rate [142, 50]. Since nanocrystals photobleach after a finite amount of time, single SWIR wavelength NC experiments demand efficient collection and detection of the weak luminescence.

In this chapter, we marry confocal microscopy with SNSPD detection to construct an apparatus that provides an unobstructed view of single PbS NC fluorescence dynamics. Section 3.1 explores luminescence blinking in overcoated PbS nanocrystals, while Section 3.2 details the $g^{(2)}$ intensity autocorrelation measured on both individual and clusters of NCs.

3.1 Two-state intermittency

Lead sulfide nanocrystals were chemically synthesized following literature guidelines, as part of a scale-up preparation [141]. After precipitating the core particles in isopropanol and redissolving in hexanes, a large excess of cadmium oleate dissolved in toluene was added and the resulting mixture was heated at 100 °C for a few hours. The Cd^{2+} ions undergo a cation exchange with surface Pb^{2+} ions, passivating the most reactive facets of the core NCs. This strategy is beneficial as it boosts the luminescence quantum yield (PL QY) of the final NC solution as measured with an integrating sphere - in our experience, an increase from $< 20\%$ to 35-40% is common. The surface of PbS NCs is extremely susceptible to PL-quenching oxidation, even after the Cd^{2+} treatment - therefore, we almost always performed the single NC measurements within 24 hours of the shell growth. Nanocrystals were transported to Lincoln Laboratory, the site of our SWIR confocal microscope, in a nitrogen environment - occasionally, the sample was precipitated once and redissolved in hexanes to purify the PbS/CdS NCs but this was not found to be necessary. The NC solution was diluted to a $\approx 10^{-10} M$ solution with 9:1 hexane:octane, and this was dropcast onto glass microscope coverslip (Electron Microscopy Sciences, No. 1) before being loaded face-down in our SWIR microscope. The final batch of core/shell nanocrystals had a bandgap of ≈ 1.1 eV, as determined from the ensemble emission spectrum (Figure 3-1a). We remind the reader that for the experiments in this chapter, the 36% d.e. four-channel SNSPD on sapphire was used for luminescence detection, necessitating long-pass excitation filters to remove laser scatter from the detected signal. In subsequent experiments performed on InAs nanocrystals (Chapter 4), the 60% d.e. silicon-backed SNSPD was utilized.

When excited using 633 nm continuous-wave light at a moderate flux of ≈ 1.1 kW/cm^2, single PbS/CdS nanocrystals clearly exhibited fluorescence intermittency, stochastically switching between a fluorescent on state and a nonfluorescent off state (Figure 3-1b). We verified that the off state count rate in all measurements was equal to the dark count rate measured from a pristine coverslip under identical experimental

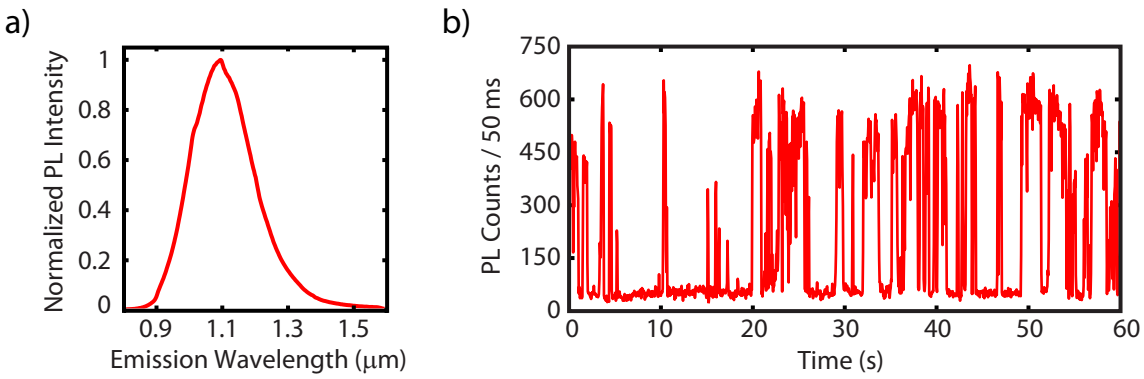

Figure 3-1: a) Normalized ensemble emission spectrum for PbS/CdS NCs used in this chapter, with $E_g \approx 1.1$ eV. b) Representative blinking trace for a single PbS/CdS NC excited with continuous-wave 633 nm light, showing strong two-state intermittency.

conditions, supporting our assignment of binary blinking. Similar dynamics were observed across the handful of PbS/CdS NCs we were able to optically detect - to highlight this behavior, representative blinking traces for three different nanocrystals from the same synthetic batch are shown in Figure 3-2a. Curiously, the data suggests that the PbS/CdS NCs we studied spend a remarkably short amount of time in the on state, and when an individual NC randomly switches from off $\rightarrow$ on it only does so for a few seconds at most. This is in stark contrast to the dynamics commonly seen in modern CdSe-based NCs, where a high-quality shell can almost completely suppress blinking [20, 54]. The low 'on-fraction' makes single NC detection even more challenging, given the other experimental restrictions on both the collection and detection of weak SWIR emission (see Chapter 2 for more details on the experimental setup).

The single NC fluorescence trace is a valuable asset, and greatly informs on exciton physics when examined through the lens of statistics [7]. For example, we can quantify the initial observation made above regarding on and off times and directly measure the probability density $P(t_{\text{on}})$ of observing an on period of time t_{on}, having defined a fluorescence intensity threshold that demarcates an on and off state. In Figure 3-2a, this is indicated by the dotted blue line. For two-state dynamics this threshold setting is relatively straightforward, but it remains somewhat of an open question for more complex behavior, especially since the intermittency statistics vary considerably

depending on the threshold used [25, 138]. In any case, the functional form of the probability density distributions $P(t_{\mathrm{on/off}})$ is of primary interest to us, since the nature of carrier relaxation as well as any stochastic process responsible for switching single NCs on and off is encoded in these distributions [134, 41, 40]. If a single trap or quenching process (such as Auger recombination) with a well-defined rate constant k_{trap} was responsible for the on $\rightarrow$ off transition, the probability density $P(t_{\mathrm{on}})$ would have an exponential form:

$$P(\tau) = -\frac{d}{d\tau} N_{\mathrm{on,off}}(\tau) = -\frac{d}{d\tau} e^{-k_{\mathrm{trap}}\tau} = k_{\mathrm{trap}} e^{-k_{\mathrm{trap}}\tau} \tag{3.1}$$

where τ represents either the on or off times. This simple model describes the oft-studied singlet-triplet dynamics in single organic molecule spectroscopy [8], nanodiamond PL intermittency [13], and was first used as the 'quantum jump' model in atoms [3]. However, studies have shown that nearly all nanocrystal systems to date exhibit power-law-distributed on and off periods ($t_{\mathrm{on/off}}$) of emission, indicative of a highly distributed mechanism for quenching and reviving the luminescence. Both theory and experiments on CdSe-based NCs suggest the following functionality [40, 23]:

$$P(t_{\mathrm{on}}) \propto t_{\mathrm{on}}^{-\alpha_{\mathrm{on}}} exp\left(-t_{\mathrm{on}}/\tau_{\mathrm{sat}}\right) \tag{3.2}$$

$$P(t_{\mathrm{off}}) \propto t_{\mathrm{off}}^{-\alpha_{\mathrm{off}}}. \tag{3.3}$$

To extract on- and off-time probability density distributions from the PbS/CdS data, on and off event frequency histograms $H(t_{\mathrm{on/off}})$ (i.e. $H(t_{\mathrm{on},i})$ is equal to the number of times an on period of length $t_{\mathrm{on},i}$ is measured) are first generated, and then weighted by a factory of $0.5(t_{\mathrm{on/off,i+1}} - t_{\mathrm{on/off,i-1}})$ for each i^{th} value. The weighting only necessary when the frequency of events, especially long-time ones, is very small, and serves to extend the temporal dynamic range of the histogrammed datasets [53]. In Figure 3-2b, raw $H(t_{\mathrm{on/off}})$ histograms are plotted on double logarithm axes for the three nanocrystals shown adjacently, with both the on- and off-time distributions exhibiting very similar power-law dynamics. The black dotted lines in Figure 3-2b

are power law functions with $\alpha_{\text{on,off}} = -1.5$, and match the slopes of $H(t_{\text{on/off}})$ well.

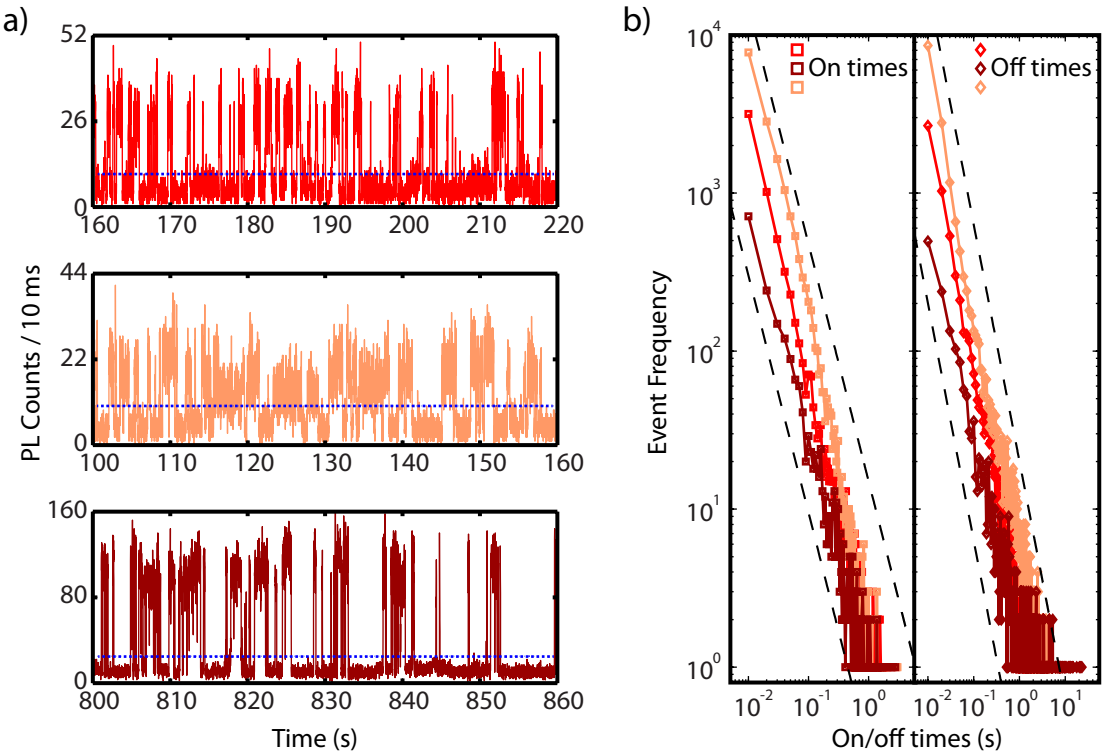

Figure 3-2: a) Representative blinking traces from three different PbS/CdS NCs, interrogated under the same conditions. The on state is brightest in the lowest panel, suggesting that this NC has the fastest radiative rate, or is somehow coupled better to the collection optics of the microscope. The blue dotted line indicates the threshold used to differentiate between on and off states. b) Blinking statistics for the three NCs shown in a) display similar trends; both on and off-time probabilities fit power laws with coefficients very close to 1.5 (black dotted lines are calculated using power laws with $\alpha_{\text{on,off}} = -1.5$).

We combined the histograms from all the PbS/CdS data we collected, and plotted the probability density distributions $P(t_{\text{on,off}})$ in Figure 3-3. Most intriguing is that the power-law exponents α are essentially the same as every other colloidal NC nanomaterial studied to date [40], with a few notable exceptions [42, 20]. Fitting the distributions to the power-law equations above gives exponents $\alpha_{\text{on}} = 1.46 \pm 0.05$, $\alpha_{\text{off}} = 1.51 \pm 0.05$ and a cutoff time $\tau_{\text{sat}} = 1.3 \pm 0.1$ s, and excepting for the low-probability data in the off-time plot (Figure 3-3b), the majority of the dataset suggests excellent fits.

It is both complex and compelling to observe similar blinking power-law exponent

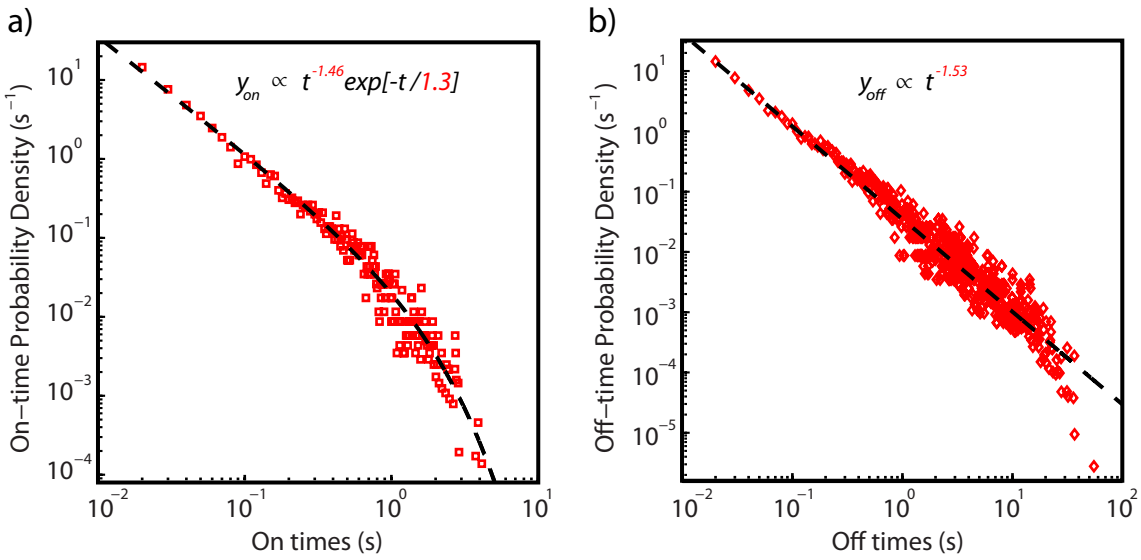

Figure 3-3: On and off-time probability densities for PbS/CdS NCs, plotted on double logarithmic axes. a) The on-time probability density (open squares) follows a power-law with an exponential cutoff at longer times. b) The off-times (open diamonds) are similarly power-law distributed but do not display an appreciable exponential cutoff at longer waiting times. The rarity of extremely long off-times ($t_{\text{off}} > 30$ s) skews the data away from the power-law fit (Equation 3), but does not justify the use of an exponential cutoff (see main text).

values in PbS NCs to those found in visible emitting NCs ($1 < \alpha_{\text{on/off}} < 2$). On the one hand, it frustrates those who believe blinking is intimately tied to the intrinsic properties of the nanocrystal: PbS and CdSe have vastly different crystal structures (rock salt vs. wurtzite), dielectric constants ($\epsilon_{\text{CdSe},\infty} = 6.2, \epsilon_{\text{PbS},\infty} = 17.2$), and electronic structure [1, 28]. However, it furthers the theory that the processes governing stochastic blinking in colloidal nanocrystals are universal, seemingly insensitive to microscopic material properties and perhaps better characterized by physical properties like shape, surface passivation and the local chemical environment. A number of theories have invoked mechanisms that do not rely on intrinsic chemical properties such as the material's band gap, electron/hole effective masses or the dielectric constant [41, 134]. Recently, statistical analysis of another peculiarity in colloidal nanocrystals, luminescence spectral diffusion, was conducted using a bath of environmental two-level systems in the same way Ref. [41] analyzed single NC blinking statistics, with both approaches finding anomalous power-law distributions of the experimental

observables [109]. It is our hope that the experiments contained in this section contribute to the ongoing debate regarding intermittency in single NCs, and help guide future theoretical efforts to explain the phenomenon.

3.2 Statistical properties of light

As we highlighted in the previous section, there is much to be learned about the exciton lifecycle by analyzing the statistics of luminescence intermittency. However, to fully realize the potency of statistical analysis in the light emission process, we must set aside the binned fluorescence traces and look directly at the photon stream. The results below highlight both classical and quantum interpretations of light, and reveal both theoretical and experimental situations that show the quantized nature of photons, for which no classical analog exists. An excellent introduction to this topic can be found in Fox's book [38]; the more rigorously inclined reader is pointed to Loudon's monograph [73].

3.2.1 Light statistics: Poissonian

The first key point to understand is that even for a light source (a laser, a light bulb, the sun) with constant intensity I (i.e. constant photon flux), the way in which these photons are distributed in subsegments of time can be quite different:

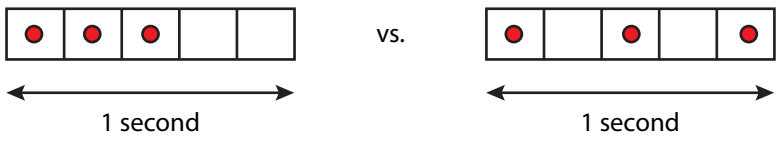

with the red dots identifying the position of an individual photon in a subsegment of time. Both light beams have a flux of 3 photons/second. More generally, the photon flux for a monochromatic light field with constant I can be expressed as $IA/\hbar\omega = \Phi$, where A is the cross-sectional area of the beam. Therefore the average number of

photons in a beam of length L is

$$\bar{n} = \frac{\Phi L}{c}, \text{with } \bar{n} = \text{integer for large } L. \tag{3.4}$$

What we would like is a quantity that characterizes the statistical distribution of photons throughout the beam. In other words, what is the probability $P(n)$ of finding n photons in a beam of length L with N subsegments? Defining $p = \bar{n}/N$ as the probability of finding a photon in one of the subsegments, $P(n)$ follows the binomial distribution:

$$P(n) \propto p^n(1-p)^{N-n} = \frac{N!}{n!(N-n)!}p^n(1-p)^{N-n} \tag{3.5}$$

where we have assumed that N is large enough that the probability of finding two photons in the same subsegment is negligible. Substituting our definition for p into Equation 3.5, and taking the limit of $N \to \infty$ gives

$$P(n) = \frac{1}{n!}\underbrace{\left(\frac{N!}{(N-n)!N^n}\right)}_{\text{as } N\to\infty,\, \approx 1}\bar{n}^n \underbrace{\left(1-\frac{\bar{n}}{N}\right)^{N-n}}_{\approx e^{-\bar{n}}} \tag{3.6}$$

$$P(n) = \frac{\bar{n}^n}{n!}exp(-\bar{n}) \tag{3.7}$$

using Stirling's approximation $lnN! = NlnN - N$ to simplify the first bracketed term, and a series expansion to obtain the exponential. $P(n)$ is then described by a Poisson distribution that states, for a given $\bar{n}$ (or photon flux Φ), the probability of measuring $n \neq \bar{n}$ photons is non-zero. Continuous-wave laser light is well-described by Poissonian statistics - what Equation 3.7 tells us experimentally is that even for extremely faint laser light ($\Phi < 1$), the probability of measuring more than one photon at a time is non-zero.

3.2.2 Light statistics: sub-Poissonian

If instead of a laser, a single molecule or nanocrystal was the source of light, what distribution would $P(n)$ adopt? In the case of a Poissonian light source, we made the

assumption that photons could be randomly distributed among the N subsegments, and then counted the number of ways in which these photons could be arranged without two overlapping in the same segment. For a perfect single emitter with unity quantum yield [73],

$$P(n) = \begin{cases} 1, n = \bar{n} \\ 0, n \neq \bar{n}. \end{cases} \tag{3.8}$$

Physically, this means that the number of photons produced by a perfect single emitter is deterministic - in fact, they are also equally spaced in time (with some jitter due to the lifetime of the excited state). This equal spacing, or "antibunching", is a beautiful result that occurs due to the finite time it takes for a molecule to be excited after the first excitation [8]. It is this unique statistical property that we can experimentally measure using a $g^{(2)}(\tau)$ intensity autocorrelation (*vide infra*), to determine whether we have indeed optically interrogating a single nanocrystal. The $g^{(2)}(\tau)$ measurement can be simply thought of as mapping the probability of detecting two photons for a given time delay τ between photons 1 and 2 - as discussed above, this temporal distribution between subsequent photons is unique for a single emitter. The parameter of interest is the value of $g^{(2)}$ at time-zero: if a perfect single emitter with negligible two-photon emission probability is being investigated, $g^{(2)}(0) = 0$. More realistically, $g^{(2)}(0) < 0.5$ after accounting for spurious coincidence counts. If the number of emitters in the collection focal volume $q = 2, 3, 4...$, the extent of antibunching decreases until $g^{(2)}$ looks just like that for a Poissonian source (*vide infra*). A cartoon highlighting the differences between Poissonian (classical) and sub-Poissonian (non-classical) light is shown in Figure 3-4a, alongside the corresponding $g^{(2)}$ (3-4b). In the following section, we will use the $g^{(2)}$ autocorrelation to determine whether we truly are studying individual NCs, and show how it reports on other intrinsic excitonic properties within a NC, such as the radiative lifetime.

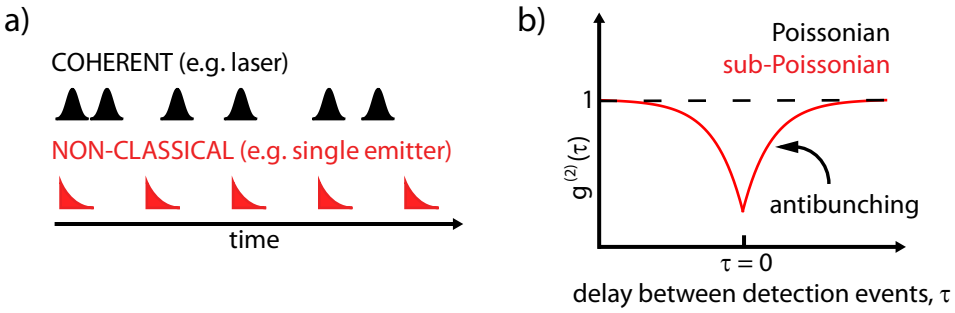

Figure 3-4: Statistical properties of light. a) Classical cw light is randomly distributed in time, while emission from a perfect single emitter is deterministically spaced in time. b) A $g^{(2)}$ measurement can be used to identify the presence of a single emitter, by looking for antibunching near $\tau = 0$ (red curve). A Poissonian light source has a constant $g^{(2)}$ for all τ (black dotted line). The rise time of the dip (red curve) can be fit to extract the excited state lifetime of the single emitter.

3.3 Sub-Poissonian emission statistics from a single PbS NC

While two-state blinking is a signature of single NC localization [98], we strengthened the assertion by measuring the statistical nature of the emission photon stream with the second-order intensity autocorrelation $g^{(2)}(\tau)$:

$$g^{(2)}(\tau) = \frac{\langle I_1(t) I_2(t+\tau)\rangle}{\langle I_1(t)\rangle \langle I_2(t+\tau)\rangle} = \frac{q-1}{q} + \frac{1}{q}\left(1 - exp\left(-k_{\text{tot}}\,|\tau|\right)\right) \tag{3.9}$$

where q is the number of emitters in the focal volume, $k_{\text{tot}} = \gamma + k_{\text{L}}$, $\gamma = I_{\text{ex}}\sigma/\hbar\omega$ is the excitation pumping rate, k_{L} is the single exciton radiative rate, σ is the absorption cross-section at 633 nm and I_{ex} is the excitation intensity [73]. In our experiment, the photon arrival times recorded on each superconducting nanowire were correlated with the other three channels, achieving a 50% increase in coincidence counts compared to a two-channel setup. We emphasize that even in the correlation measurements, each emission photon has a 36% chance of detection (rather than 9% if only one channel was active); this is because the photon's spatial mode overlaps with all four nanowire channels on the interleaved SNSPD chip, increasing the probability of detection to that of all four elements combined. One can readily make the analogy between our

method and a Hanbury Brown-Twiss (HBT) setup that splits the emission photon stream to four independent detectors, each with a detection efficiency of 36%. Figure

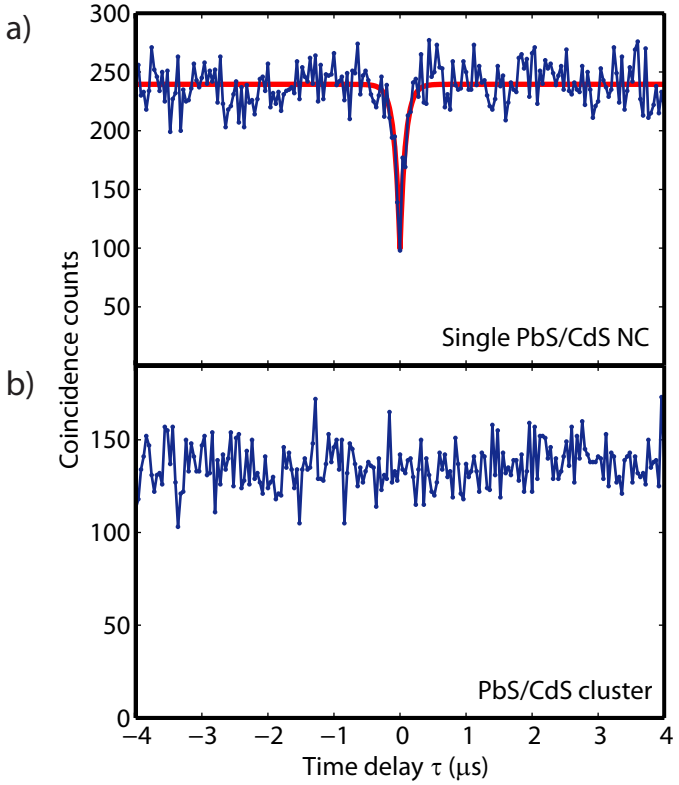

Figure 3-5: Unnormalized intensity autocorrelations for PbS/CdS nanocrystals. a) Strong antibunching from a single blinking SWIR nanocrystal, characteristic of non-classical luminescence. After accounting for the uncorrelated background, the normalized $g_0^{(2)} \approx 0.19$. The solid red line is a double-sided single exponential fit, which, after accounting for the excitation pumping rate γ, gives an extracted excited state lifetime of ca. 115 ns (see text). b) The same measurement on a cluster of nanocrystals displayed no dip at zero time delay as expected from a group of independent emitters.

3-5a depicts an unnormalized $g^{(2)}$ measurement for a single PbS/CdS nanocrystal - the 0-time dip was found to be $g_0^{(2)} = 0.415$ when normalized by the coincidence count value at longer times, strong evidence that the SWIR emission is non-classical and is composed primarily of single photons. The full extent of antibunching is reduced due to the accumulation of uncorrelated background-background and signal-background coincidence counts during the integration period, obscuring the intrinsic NC $g_0^{(2)}$. For

four detection channels the uncorrelated coincidence counts can be calculated using

$$C_{\mathrm{uc}}(\tau) = \sum_{i=1}^{4} \sum_{j>i}^{4} (N_i N_j + N_i S_j + N_j S_i) w T, \tag{3.10}$$

where N_i (S_i) is the average dark (signal) count rate on channel i, w is the bin time for $g^{(2)}(\tau)$, and T is the integration time (note that $S + N = I_{\mathrm{PL}}$, the average count rate measured on each channel). For this experiment $N_i = 280$ counts/s, $S_i = 266$ counts/s, $w = 40$ ns, and $T = 1200$ s, giving $C_{\mathrm{uc}}(\tau) = 65$. Subtracting this value from the unnormalized 0-time dip and recalculating the extent of antibunching gives $g_0^{(2)} \approx 0.19$, a much stronger indicator of single emitter localization.

It has been shown in CdSe nanocrystals that multi-exciton radiative emission can corrupt the single photon stream even in the limit of low excitation fluence, due to a small but finite biexciton quantum yield [106, 96]. However, one would expect the biexciton quantum yield to be low based on ensemble $k_{\mathrm{BX,rad}}$ and $k_{\mathrm{BX,non\text{-}rad}}$ measurements for PbS (ca. 10^7 s^{-1} and 10^{10} s^{-1}, respectively) [87, 95]. While the probability of a secondary adjacent nanocrystal emitting into the collection volume ($q = 2$) is very low (the blinking trace exhibits clear two-state instead of three-state blinking), we note that our calculation of $C(\tau)$ accounts for this by using the off-state intensity rather than the detector dark count rate for N_i. We also collected fluorescence from a cluster of nanocrystals ($q > 3$) that did not blink but exhibited continuous intensity fluctuations, and extracted the resulting $g^{(2)}(\tau)$. No 0-time antibunching was seen (Figure 3-5b), confirming that the observed single NC antibunching was not an artifact of the experiment.

Even though this experiment was performed with cw excitation, we can still extract dynamical information about the exciton from the $g^{(2)}$ data. Fitting the antibunching dip to a double-sided exponential gives $k_{\mathrm{tot}}^{-1} = 82$ ns - estimating $\gamma \leq \left(1100 \text{ W/cm}^2 \times 1 \times 10^{-15} \text{ cm}^2\right) / \left(3.14 \times 10^{-19} \text{ W}\right) = 3.5 \times 10^6$ s^{-1}, the excited state lifetime for this particular PbS/CdS nanocrystal was $k_{\mathrm{L}}^{-1} \leq 115$ ns. The absorption cross-section at the excitation wavelength was obtained by scaling $\sigma_{\text{band-edge}}$ by the optical density at 633 nm, using band-edge values from Ref. [18]. Given the uncer-

tainties in accurately determining γ (i.e. most likely underestimating the excitation spot size), we can at most provide an upper bound to the excited state lifetime, but this value is still considerably shorter than the ensemble photoluminescence lifetime in solution (ca. 500-1000 ns). In CdSe NCs, the extracted time constant k_{tot}^{-1} varies at most by a factor of 2-5, over a wide range of excitation fluences [74]. Since the k_{tot}^{-1} we measure is more than an order of magnitude faster than previously measured ensemble lifetimes, we believe it reflects an intrinsic property of *this* particular nanocrystal, rather than an extreme pumping rate γ.

3.4 Conclusion

In summary, we have experimentally realized a platform to count single infrared photons from individual quantum systems under ambient conditions, directly probing the excitonic lifecycle in single SWIR nanocrystals. The data in this chapter highlights both new and surprising features in the fluorescence from PbS/CdS nanocrystals, discussing the statistics of blinking and the quantum nature of light emission (antibunching). The ability to perform sophisticated photon correlation measurements like $g^{(2)}$ is exciting: in the next chapter, we will extend its use by switching to pulsed excitation, in order to probe more deeply the dynamics of single and multiple excitons within single SWIR NCs.

Chapter 4

Time-evolution of excitons in single InAs colloidal nanocrystals

Excitons form the basis of light-matter interactions in semiconductor nanocrystals (NCs) [99, 11, 59, 27], as well as in a host of other nanoscale materials [124]. These excitations have proven to be extremely useful intermediaries when converting between different forms of energy - for example, turning solar radiation into electric power in a photovoltaic device [120], or producing light under current injection as is done in an LED [128]. In fact, the creation, time-evolution and subsequent recombination (or ionization) of excitons are central processes that govern the efficiency of devices that use NCs; a detailed understanding of this "excitonic lifecycle" is crucial if we are to experimentally realize the full potential of solution-processed devices.

Single-molecule spectroscopy has played a central role in probing nanocrystal physics, providing us with experimental observables that directly report on the behavior of excitons in confined systems [34, 45, 23]. In particular, time-resolved measurements have allowed us to dissect two key steps in the lifecycle outlined above: the time evolution, and subsequent recombination, of both single and multiple excitons within an individual NC [123, 69, 129, 36, 96, 106]. These results and others like them have helped build a causal link between the observed dynamics and chemical properties of nanocrystals (for example, the nature of the shell used to coat the surface), steering synthetic efforts to chemically synthesize brighter, more photostable

fluorescent nanomaterials in the visible portion of the spectrum that are of real use in today's applications [128, 63, 114]. Ideally, one would like to realize these gains for NCs whose optical activity extend beyond the visible and into the shortwave-infrared (Pb chalcogenides, InAs, HgTe). Given their dramatically different optical and electronic properties [1, 137, 71], there is much to learn if we can interrogate SWIR nanocrystals individually. Here, we classify a nanocrystal as being SWIR-active if it absorbs or emits light between 1-3 μm.

The peculiar properties of InAs - a large exciton Bohr radius of 34 nm, an extremely light electron effective mass of $0.023m_0$ - along with its faster radiative rate compared to PbS NCs make it a prototypical system for single NC interrogation in the shortwave-infrared. Until recently [24], the only experimental tool that successfully probed individual InAs NCs was the scanning tunneling microscope (STM) [6, 72, 47]. Using tunneling spectroscopy, Banin and co-workers observed discrete energy level structure and atomic-like states in single InAs NCs [4], and subsequently extended this work to chemically doped nanocrystals [90]. However, while these measurements are not subject to the transition selection rules that optical experiments must obey, they are static in nature; conventional STM does not allow us to study non-equilibrium exciton dynamics in the same way optical experiments do. Transient photoluminescence (PL) [122], transient absorption [10] and terahertz spectroscopy [107, 108] have been employed to investigate ultrafast phenomena near the band edge of InAs NCs, but these experiments were conducted at the ensemble level and therefore only report the average of observable distributions.

In this chapter, we describe the first optical experiments on individual colloidal InAs/CdZnS nanocrystals and their fluorescence dynamics under ambient conditions. Upon correlating the luminescence intensity to the PL decay lifetime, we discover that InAs NCs blink in one of two ways, either with the PL decay rate fluctuating simultaneously with the PL intensity or remaining constant for all PL intensities other than the off state. We also find that nearly every InAs/CdZnS NC in this experiment had a near-zero biexciton quantum yield under pulsed illumination, a surprising observation given the broad distribution in radiative rates extracted from

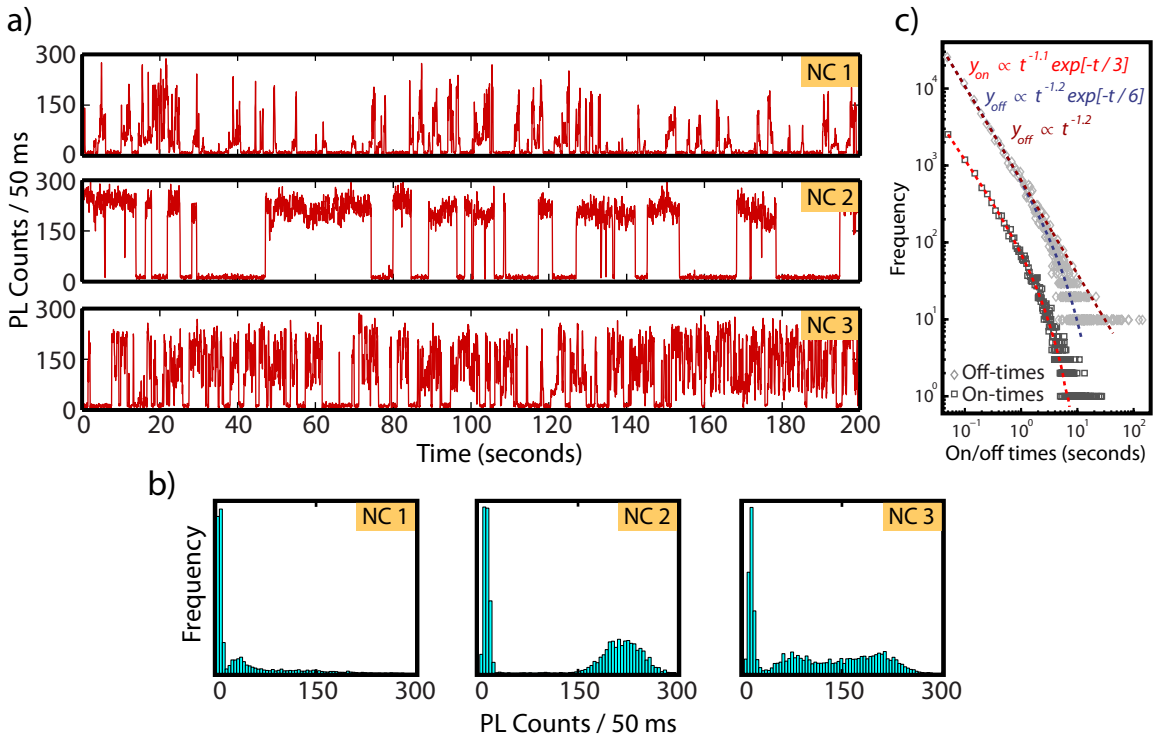

Figure 4-1: Representative blinking dynamics from single InAs/CdZnS NCs. a) Three blinking traces with corresponding intensity histograms in c). The frequency distributions in b) for on and off times are fit to pure power laws and power laws with exponential cutoffs; the extracted power exponents were $\alpha_{\text{on}} = -1.1 \pm 0.1$ and $\alpha_{\text{off}} = -1.2 \pm 0.1$, with an apparent exponential cutoff near $\tau = 3$-6 s. The exponents are slightly smaller than the $\alpha_{\text{on,off}} = -1.5$ measured in conventional CdSe-based nanomaterials.

on state PL lifetimes.

4.1 Observation of a grey emissive state in InAs NCs

The experimental apparatus used in this experiment is identical to the one used in the previous chapter, with the exception of a new detector that was grown on silicon instead of sapphire [117]. The collected SWIR luminescence from single 1295-nm-emitting InAs/CdZnS (90% Cd, 10% Zn) NCs is detected by illuminating cryo-cooled superconducting nanowire single photon detectors through the silicon substrate, acting as an additional longpass filter in the optical path (at 3 K, the silicon bandgap is

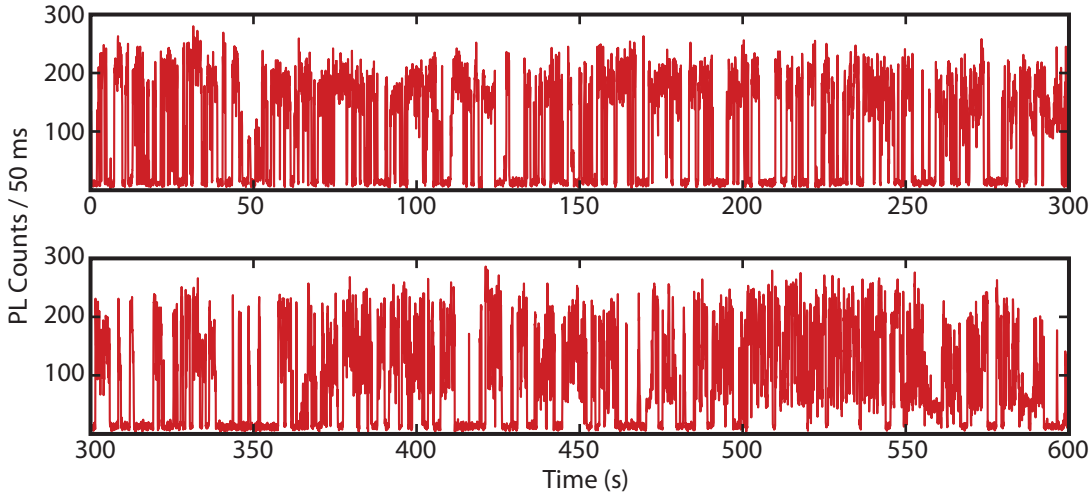

Figure 4-2: Emergence of a grey state in InAs NC 3, over the course of minutes. The timescale of appearance suggests a slow photoinduced chemical oxidation, or gradual buildup of molecular species that perform chemistry on the surface.

≈1.17 eV [12]). The nanocrystals were provided by QD Vision, and synthetic details are provided in Ref. [60]. Briefly, the InAs cores are 3.5 nm in diameter as determined from a sizing curve, with a nominal CdZnS shell thickness of 2 monolayers (2.3 Angstroms/monolayer) [51]. The concentrated NC-hexanes solution was diluted with a 9:1 hexane:octane mixture, and dropcast in air onto a No. 1 glass microscope coverslip. Pulsed excitation at 633 nm (instrument-response function ca. 200 ps) was used for all of the experiments below, with the power adjusted to be in the linear excitation intensity regime as confirmed by saturation of the fluorescence intensity. Photon arrival times were recorded in a time-tagged time-resolved mode (TTTR) using a Picoquant Hydraharp. In total, 21 individual InAs nanocrystals were studied.

The three blinking traces in Figure 4-1a exemplify the range of behavior we observe across the sample. NC 1 spends most of its time in the off state, experiencing short sojourns to an emissive state with varying amounts of non-radiative recombination, while NC 2 is more binary in nature with discrete switching between on and off. However, the range of intensities observed in the on state for NC 3 is broad, indicative of fast switching between a bright and grey state ($I_{\text{bright}} \approx 225$ counts/50 ms, $I_{\text{grey}} \approx$ 70 counts/50 ms). These dynamics are more clearly seen in the intensity histograms

(Figure 4-1b). What is intriguing about NC 3 is that the first few minutes of optical interrogation produced blinking that looked more like NC 2, with the grey state gradually emerging over the course of a minute (Figure 4-2). Grey-state emission has been observed before, most prominently in thick-shell CdSe/CdS nanocrystals, with trions (i.e. a single exciton with an additional charge carrier) being implicated as the cause [46, 129, 80]. In Gomez et al. the grey state in CdSe/CdS is attributed to oxidation of the nanocrystal surface [46] - here, the timescale of appearance for the new emissive state in NC 3 implies either a slow photoinduced oxidation process that is cumulative (multiple reaction events occurring on the surface with time), or a gradual buildup of molecular species that perform chemistry on the reactive facets of the NC. The PL lifetime measurements (discussed below) suggest that the shell thickness varies from NC to NC, and may lead to an increased surface reactivity for some nanocrystals over others.

Setting a dark count rate threshold of approximately 30 counts/50 ms, we extract frequency histograms for on and off waiting times between switching events. These are summarized in Figure 4-1c along with pure power-law and power-law/exponential cut-off fits to the data. Best fits are obtained with power law exponents $\alpha_{\text{on}} = -1.1 \pm 0.1$ and $\alpha_{\text{off}} = -1.2 \pm 0.1$, with an apparent exponential cutoff near τ = 3-6 s. The exponents are nearly equal, similar to the blinking dynamics seen in most other NC systems [40]. The CdSe/CdS nanocrystals recently synthesized by Chen et al. [20] are an exception; a statistically significant difference between on and off-state waiting time distributions has been measured, with $\alpha_{\text{off}} > \alpha_{\text{on}}$.

If the excitons involved in bright and intermediate emission, as observed in NC 3, are unique species (i.e. neutral and charged excitons, respectively), measuring the PL lifetime as a function of fluorescence intensity would allow us to probe these states individually and extract the associated recombination rate. We construct single NC PL lifetimes using photon detection events that, when binned, fall within a particular range of luminescence intensity - since we have access to the photon arrival times, this is a relatively straightforward process (see Brent Fisher's thesis for a detailed explanation of how one goes from the arrival time data to the intensity-dependent

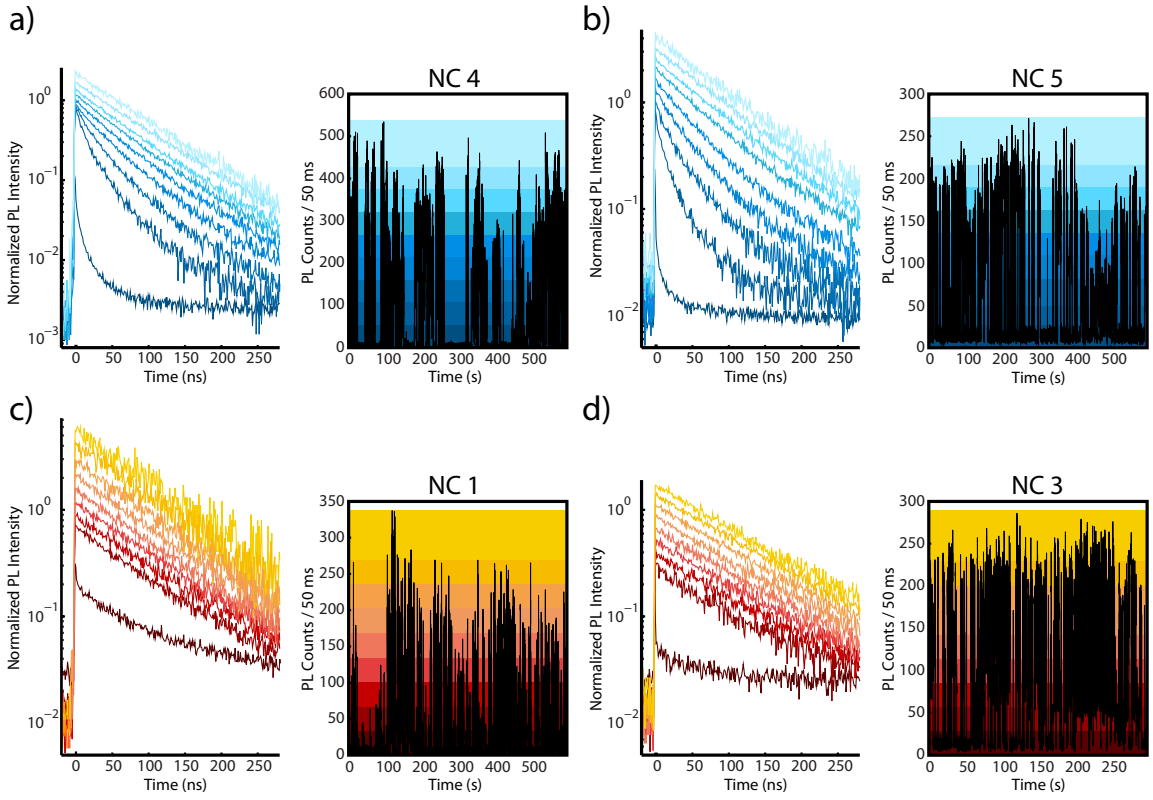

Figure 4-3: PL-intensity-dependent single NC lifetimes and corresponding blinking traces. Two types of emission are observed - in a) and b), an increasing non-radiative decay component grows in at lower PL intensity (type I, blue panels); in c) and d), the lifetime does not fluctuate with PL intensity (type II, red panels). Lifetime decays are displaced vertically for clarity, with temporal bin size of 1.024 ns.

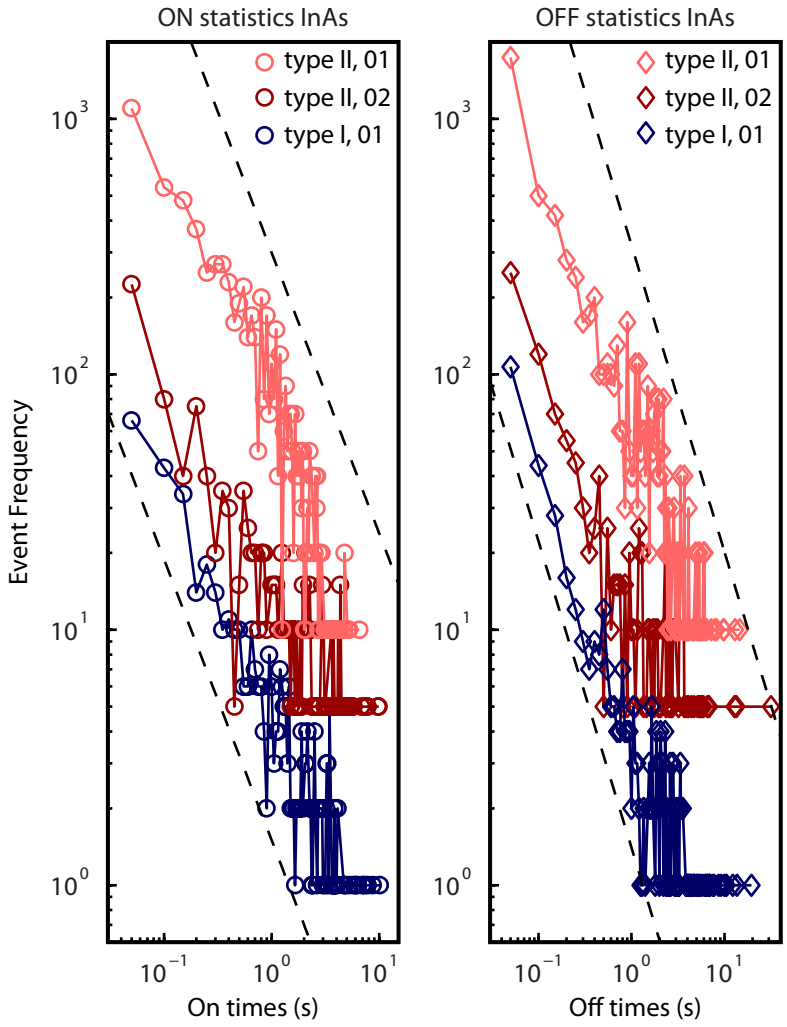

Figure 4-4: Blinking statistics for three different individual InAs/CdZnS nanocrystals, bounded by power laws (black dotted lines) with exponents $\alpha_{\text{on}} = -1.1$, $\alpha_{\text{off}} = -1.2$. Both type I (dark blue) and type II (dark and light red) NCs follow the power law plots fairly closely; the on times for 'type II trace 01' (light red) appears to kink at about 0.6 s, possibly due to the onset of an exponential cutoff.

PL decay traces). The generated lifetimes are color coded according to the intensity range used, and plotted for four different NCs (Figure 4-3). We note that while the adjacent blinking traces in Figure 4-3 are often just subsections of a longer acquisition, the PL lifetime decays are only constructed from photons in the section shown. The data suggest that single InAs/CdZnS nanocrystals exhibit two types of blinking - type I (Figures 4-3a,b), where a fast non-radiative component grows in the PL decay for lower intensity periods, and type II (Figures 4-3c,d), where the lifetime remains constant for all intensity values other than the off state. Of the 21 nanocrystals we studied, 13 were definitively type I, 5 of them type II, and 3 showed some mix of the two. Type I dynamics are characteristic of most visible nanocrystals studied to date, and has been assigned to a fluctuating non-radiative rate k_{nr} based on the observation that the PL lifetime trace becomes more monoexponential as the PL intensity increases [37, 123]. Galland et al. first reported a new kind of blinking where some thick-shell CdSe/CdS NCs experienced no change in PL lifetime even as the NC switched off ("Type B" in their paper) [42]. The type II dynamics we observe are somewhat similar to the anomalous "Type B" blinking in that the lifetime appears independent of the PL intensity, except for the off state which in our case has a fast decay time reflective of the instrument-response function. We also find that type I and II nanocrystals have very similar on and off waiting-time statistics - in Figure 4-4, blinking statistics are shown for three different nanocrystals along with power laws that bound the data ($\alpha_{\mathrm{on}} = -1.1$, $\alpha_{\mathrm{off}} = -1.2$). This is unlike the qualitative differences in blinking statistics seen by Galland et al. between their two types of intermittency.

Notably, the grey and bright-state PL decay times in NC 3 are the same, with $\tau \approx$ 114 ns (Figure 4-3d). This is in contrast to the observed dynamics in CdSe/CdS where the ratio of grey to bright PL lifetimes varies between 2-8, often as a function of shell thickness [46, 129, 42]. As a result, the grey emission has been attributed to charged exciton (i.e trion) emission - a statistical scaling of radiative rates would suggest $k^T_{\mathrm{rad}} = 2k^X_{\mathrm{rad}}$, just by counting the number of available recombination pathways. While a direct measurement of charged exciton recombination rates has not been made on

InAs/CdZnS nanocrystals, recent theoretical work on InAs/CdSe NCs found Auger non-radiative rates on the order of 10-100 ps for both positive and negative trions [19]. PL lifetimes are sensitive to both radiative and non-radiative decay, but we see no signature of fast Auger decay in NC 3, within the time-resolution of our experiment.

If the grey state we observe in NC 3 is indeed due to trion emission, a mechanism for charging the NC core prior to the subsequent excitation event (upon which the trion species is created) must exist. One possibility is electron trapping, leaving the NC positively charged. Due to the small conduction band offset between bulk InAs and CdZnS, single electron states in the conduction band of InAs/CdZnS delocalize into the shell - the extremely light electron effective mass of InAs ($m_e^* = 0.023m_0$, $m_h^* = 0.41m_0$ at the bulk Γ point), enhances this delocalization. As a result, access to trapping surface states could positively charge the NC, producing a grey state in the intermittency trace. We note that our experiment cannot differentiate between a positive or negative trion. Recently, hole trapping and subsequent surface oxidation was implicated as the dominant cause of the off state in CdSe/CdS NCs, whose band offsets are similar to InAs/CdZnS with a core-shell delocalized electron, and a core-confined hole [111]. In Ref. [133], the authors synthesize a PbS-tipped CdSe/CdS nanorod, artificially adding a hole trap that they use to probe blinking. The striking similarity between their PL traces and those exemplified by NC 3 in our experiment is fascinating - both exhibit a wide distribution of on state intensities that they assign to negative charging of the nanocrystal core.

4.2 Direct measurement of InAs radiative rates

The neutral exciton radiative rate is particularly sensitive to the chemical structure of a nanocrystal, and more importantly, one that we can measure directly in this experiment. By constructing PL decay curves from photons that, when binned, have a PL intensity of at least $0.7I_{\mathrm{PL,max}}$, we obtained strictly mono-exponential 'maximum lifetime' decays (Figure 4-5a). We rely on the assumption that photons emitted for $I > 0.7I_{\mathrm{PL,max}}$ only come from the neutral exciton state with $\mathrm{QY}_{\mathrm{on}} \approx 1$ [14,

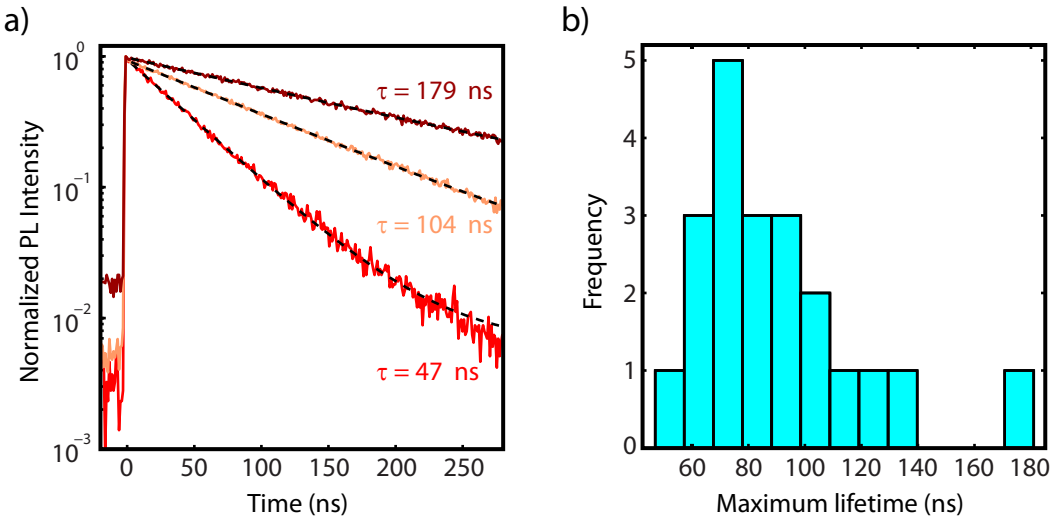

Figure 4-5: a) Three single NC maximum lifetimes, calculated using photon detections that have a binned intensity of at least $0.7I_{\mathrm{PL,max}}$. b) A histogram of extracted maximum lifetimes, which we interpret as the neutral exciton radiative lifetime. The variation most likely stems from shell-thickness heterogeneity in the sample (see text).

37], and extract the distribution of radiative lifetimes across our sample (Figure 4-5b). Figure 4-5a shows the full range of timescales that we observe from single InAs/CdZnS NCs, a spread of >100 ns. This heterogeneous behavior most likely reflects a variation in shell thickness, with the thicker-shelled InAs/CdZnS NCs having a longer radiative lifetime due to the reduced spatial overlap between electron and hole states [16]. An alternative hypothesis could be that the core radii or aspect ratio are nonuniform instead, altering the order of s-like and p-like valence-band-maximum states and resulting in different optical selection rules with the $1S_e$ conduction-band-minimum state [110] - the radiative rate we measure will depend on how strongly the band-edge radiative transition is allowed.

4.3 Negligible biexciton radiative yields

Having investigated single exciton dynamics in individual InAs NCs, we finally turn our attention to multi-excitons (MX). Measuring the optical properties of MX states is challenging, even at the ensemble level, for SWIR-active nanomaterials that are

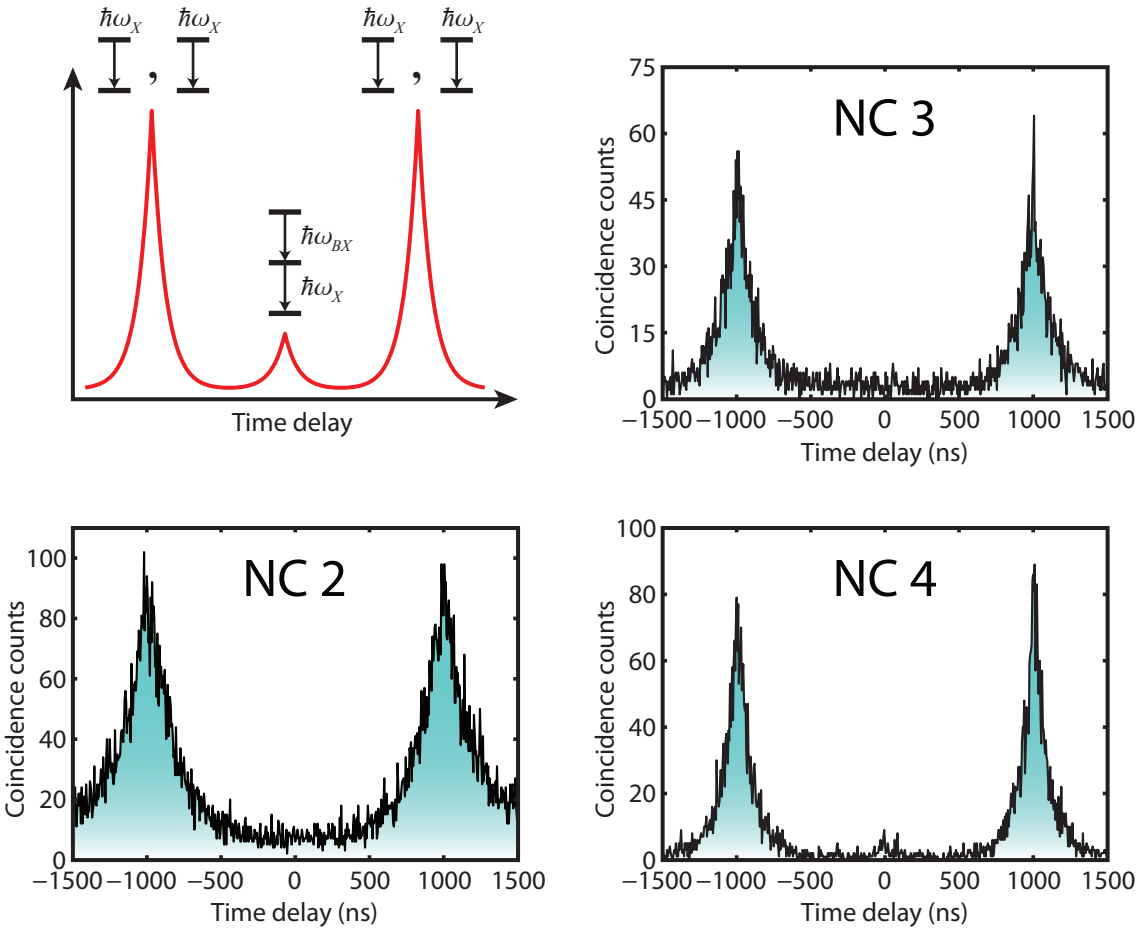

Figure 4-6: Representative $g^{(2)}$ autocorrelation traces that reveal a near-zero biexciton quantum yield for the nanocrystals studied. The ratio of center-to-side peak areas is proportional to this experimental observable, a sensitive measure of multi-exciton recombination processes.

known to degrade under strong illumination [95, 87]. In addition, the weak emission is difficult to detect, requiring sophisticated hardware such as the SNSPD to unambiguously measure the observable of interest [118]. Recent work done by our group and others has shown how $g^{(2)}$ intensity autocorrelations, measured with much lower excitation fluences, can be used to connect nanocrystal MX radiative yields to the ratio of center to side peaks in a pulsed experiment [96, 106]. This deep connection has its origins in work done on epitaxial quantum dots [119], and was extended by Nair et al. [96] to account for subtleties in the NC exciton lifecycle.

We measure $g^{(2)}$ for all 21 InAs/CdZnS nanocrystals studied in this experiment, and plot three representative traces in Figure 4-6 along with a schematic that highlights the features of a typical pulsed antibunching measurement. Surprisingly, all but one NC exhibits a negligible biexciton (BX) quantum yield, revealed by the near-zero ratio of center/side peak area for each NC (the one NC that produced BX emission has a center/side peak area ratio of ≈ 0.18). In CdSe/CdS nanocrystals, a high-quality shell can dramatically suppress non-radiative MX recombination and produce very high BX quantum yields under relatively low excitation fluence, in some cases $> 80\%$ [106]. A weak correlation exists between the on-fraction and the BX quantum yield for a single nanocrystal [139]; in this experiment all of our NCs had low on-fractions, implying that the exciton quenching processes responsible may also affect biexcitons negatively.

4.4 Conclusion

In this chapter, we investigated the lifecycle of single excitons across a broad range of timescales in individual InAs/CdSe nanocrystals, under ambient conditions. Using our newfound ability to measure time-resolved PL lifetimes, we revealed two types of blinking by correlating the decay time to the PL intensity, and, most surprisingly, find an emissive grey state with an identical PL lifetime to the bright state. As far as we are aware of, this has not been observed in nanocrystals studied to date. In parallel, we pushed the limits of collection and detection of single SWIR photons

and measured pulsed $g^{(2)}$ data with a minimal biexciton radiative signature for the same batch of NCs. As improvements are made to synthetic protocols for SWIR nanomaterials, it might become possible to chemically tune the observables probed in this study with great precision, much like we can in the visible. The analogous behavior between InAs/CdZnS and CdSe/CdS nanocrystals is intriguing, and holds great promise for the former system given the dramatic strides we have made with the latter.

Chapter 5

Photophysics of single CdSe/CdS nanocrystals

Cadmium selenide has firmly established itself as the semiconductor material of choice from which high-quality colloidal nanocrystals are chemically synthesized. With a tunable band gap throughout the visible portion of the spectrum, CdSe NCs are well-suited for applications that require bright luminescence with the added benefit of solution-processability [63, 128]. By virtue of being one of the first colloidal nanomaterials to undergo single NC interrogation [98], the photophysics of CdSe NCs have been thoroughly investigated across a range of temperatures [69, 16], magnetic [11] and electric fields [111, 58].

Of the dynamics observed, none has received more attention than fluorescence intermittency since it appears to be a universal process that affects not just nanocrystals but organic molecules [9], fluorescent proteins [26], nanodiamonds [13], and even epitaxially grown quantum dots [131, 105]. It is clear now that for nanocrystals, a high-quality shell that both insulates the core from the atmosphere and passivates the interfacial region is critical to suppressed blinking [40]. Recently, better synthetic protocols for growing crystalline cadmium sulfide shells on CdSe have produced a new generation of visible emitters that, when studied individually, rarely switch off [22, 20, 80]. This has renewed efforts to understand the nature of the off state [57, 129, 139] - what does this peculiar CdS shell provide to the NC that other

shells did not? In some experiments the fraction of time spent in the on state seems to increase with CdS shell-thickness [81], adding another dimension to the blinking puzzle.

The unique electronic structure of CdSe/CdS may clue us in on recombination processes taking place within the nanocrystal. The conduction band offset between core and shell is small, allowing the electron states to delocalize into CdS, while the hole remains confined to the core due to a large valence band offset barrier. This delocalization has the effect of reducing electron-hole overlap especially for thick-shelled CdSe/CdS NCs [16] - since the Coulomb potential V_{coul} mediating non-radiative Auger recombination (AR) scales as $1/r$, a larger effective NC size due to delocalization results in a decreased AR rate [43]. It is worth noting that most reports use the bulk CB and VB offsets for heterostructured nanocrystals band alignment, quantities which are not necessarily conserved for nanometer-sized core/shell particles. Pandey et al. have taken steps to measure the band offsets directly in II-IV semiconductor nanocrystals using intraband absorption spectroscopy, and found that the delocalized-electron/localized-hole picture for CdSe/CdS holds for certain CdSe core sizes [104]. Experimentally, a slowdown in AR for CdSe/CdS NCs is seen at the individual nanocrystal level as well, with high biexciton quantum yields η_{BX} under low excitation intensity as measured by $g^{(2)}$ autocorrelation [106]. However, there seems to be a weak correlation between on-fraction and η_{BX}, with the thickest shelled CdSe/CdS NCs exhibiting a broad distribution of η_{BX} across nominally similar NCs from the same synthetic batch [139].

A surprising observation was made by Galland and co-workers recently when they studied individual CdSe/8CdS NCs in an electrochemical cell (the prefixed number indicates the number of nominal CdS shell monolayers) [42]. By correlating the PL intensity with the instantaneous PL lifetime for a particular bin time, they discovered that under certain conditions the nanocrystal PL would switch off without changing the PL lifetime. This behavior was substantially different from previous reports on CdSe/ZnS and CdSe/CdS NCs that found an increasing nonradiative component to the lifetime for lower PL intensities [37, 123, 129, 116]. In fact, they found that

CdSe/8CdS NC blinking could be switched between this anomalous form ('Type B' in their paper) and the correlated PL intensity-lifetime form ('Type A') as a function of applied voltage. At zero bias, both A and B blinking was observed within the same nanocrystal.

Given the mechanism proposed by Galland et al. to explain Type B blinking (see below), a few hypotheses are immediately testable. In the rest of this chapter, we detail our assessment of Type B blinking in CdSe/7CdS and CdSe/2CdS NCs, and compare these results to conventional NCs (QD Corp. 655). We find a signature for type B blinking in CdSe/2CdS NCs, but attribute it to an artifact of the lifetime-fitting algorithm. CdSe/7CdS and QDC655 NCs both exhibit the well-understood type A blinking mechanism.

5.1 Grey state dynamics: trion-like behavior

5.1.1 Experimental methods

Colloidal CdSe/CdS nanocrystals were synthesized by O. Chen following Ref. [20]. All samples were carefully precipitated three times from the growth solution using a methanol/butanol mixture, and redissolved in toluene. After diluting the purified NCs further with toluene, the solution was spincoated in air onto clean glass coverslips (Electron Microscopy Sciences, No. 1) and loaded into a home-built visible confocal microscope. The microscope was identical to the one used in Ref. [139], with appropriate longpass filters used depending on the center emission wavelength of the NC sample. CdSe/2CdS NCs (2ML) has a center emission at 605 nm, CdSe/7CdS NCs (7ML) at 628 nm, and QD Corp NCs at 655 nm (QDC). Single NCs were excited with 100 nW of pulsed 414 nm laser light (IRF $\approx$ 300 ps) at 2.5 MHz repetition rate, an excitation intensity of 90-100 W/cm^2. Photon detection arrival times were recorded on a Picoquant Picoharp in time-tagged-time-resolved (TTTR) mode. We did not encounter a nanocrystal with $g^{(2)}(0) > 0.5$, and so used $g^{(2)}$ to identify if single NCs had been isolated.

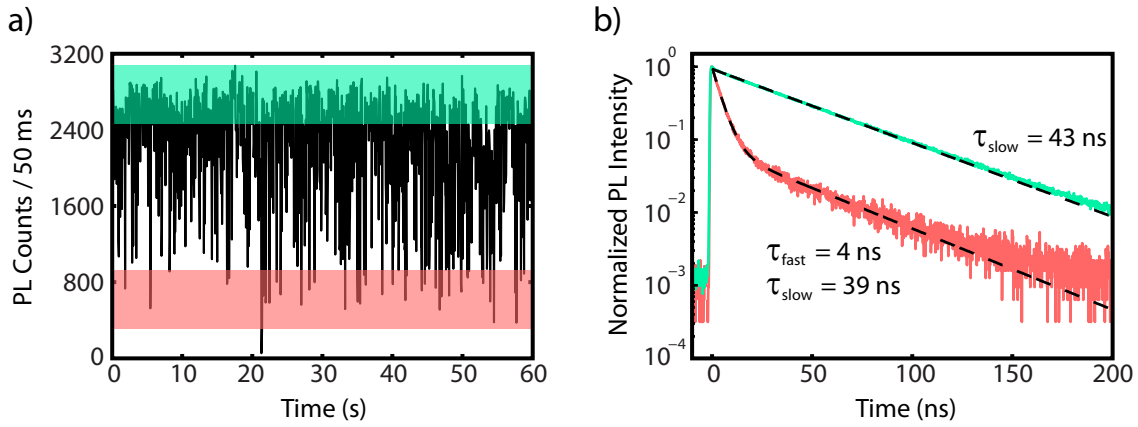

Figure 5-1: a) Representative blinking trace for a CdSe/7CdS nanocrystal with strong grey-state character. The colored bars indicate the intensity section used to generate the PL decays in the adjacent plot (see Chapter 2 for details); green indicates the bright state, while red demarcates the grey state. b) Time-averaged PL lifetime decays for the bright (green) and grey (red) state. The bright state has a monoexponential decay time of 43 ns, while the grey state is dominated (91% of the overall PL decay weight) by a fast decay of 4 ns. The temporal bin size is set to 128 ps.

5.1.2 Time-averaged PL lifetimes for single 2ML and 7 ML NCs

Upon localizing a single NC, we measure PL blinking traces and construct PL lifetimes that are time-averaged over the entire blinking trace (Figure 5-1). As was done in our work on single InAs/CdZnS nanocrystals (Chapter 4), PL intensity slices were used to generate PL lifetimes that correspond to the bright, grey, and in the case of 2ML NCs, off state. Figure 5-1a is a representative example of the PL blinking dynamics we observe from 7ML NCs - rapid switching between a bright and grey state with rare excursions to the off state. Two experimental parameters distinguish this experiment from previous studies on the same system where grey-state emission was not as frequent [139, 20]: 1) we excite NCs with a higher intensity (factor of 8-10 higher), and 2) our samples are not packaged in a polymer matrix. The grey state is not wholly unexpected, however - a larger effective NC volume by virtue of electron delocalization would slow down Auger recombination versus radiative trion emission for the reasons described above [58]. Using photon detections from the green and red portions of the PL blinking trace, we construct PL lifetimes and fit them to mono-

(bright state) and bi-exponentials (grey state) as shown in Figure 5-1b. While the green-colored PL decay has a single time constant of 43 ns, the red-colored decay is dominated by a fast time constant (91% of the overall PL decay weight) of 4 ns. The slow component for both red and green-colored decays is approximately the same, indicative of bright state emission.

Table 5.1: Summary of PL lifetime fit parameters for single CdSe/7CdS and CdSe/2CdS nanocrystals.

	Bright state	Grey state			
Nanocrystal	τ_{slow} (ns)	A_{fast}	τ_{fast} (ns)	A_{slow}	τ_{slow} (ns)
7ML NC 1	39	0.99	3.3	0.01	40
7ML NC 2	33	0.97	2.5	0.03	30
2ML NC 3	31	0.68	1.3	0.32	24
2ML NC 4	31	0.76	1.2	0.24	26

We repeated this measurement on many individual 2ML and 7ML nanocrystals, and compare two representative examples from each system in Figure 5-2 and Table 5.1. Both samples exhibit a fast component in the grey-state PL decay (colored red), with $A_{\text{fast}}^{\text{7ML}} > 95\%$ and $A_{\text{fast}}^{\text{2ML}} \approx 70 - 75\%$, across all the NCs studied. Similarly, 7ML and 2ML NCs both emit grey-state photons at a faster rate than their corresponding bright state - on average, $\tau_{\text{slow}}^{\text{7ML}} \approx 12\tau_{\text{fast}}^{\text{7ML}}$ and $\tau_{\text{slow}}^{\text{2ML}} \approx 24\tau_{\text{fast}}^{\text{2ML}}$. The 2ML nanocrystals switched completely off on occasion, and the corresponding lifetime is plotted in yellow in Figure 5-2, b and d. The decay time here was close to the instrument-response function.

Magnetic-field-dependent experiments by the groups of Hermier [57] and Lounis [33] have produced considerable evidence that the grey state in CdSe/CdS NCs is due to trion emission, although they differ as to the whether it is a positive or negative trion. In our experiment, if we assume the on state has a near-unity quantum yield [14], we can estimate the trion quantum yield from $I_{\text{PL}}^{\text{grey}}/I_{\text{PL}}^{\text{bright}} \approx 0.2$ for the 7ML NC 1 ($I_{\text{PL}}^{\text{grey,bright}}$ are the PL intensity values measured in the blinking trace). Since $g^{(2)}$ is low for this nanocrystal when averaged over the entire PL trace (i.e. single photons are being emitted for the majority of the trace), and $A_{\text{fast}}^{\text{7ML}} > 95\%$ for the grey state (i.e. one state is emitting the majority of the time during the grey period), we can

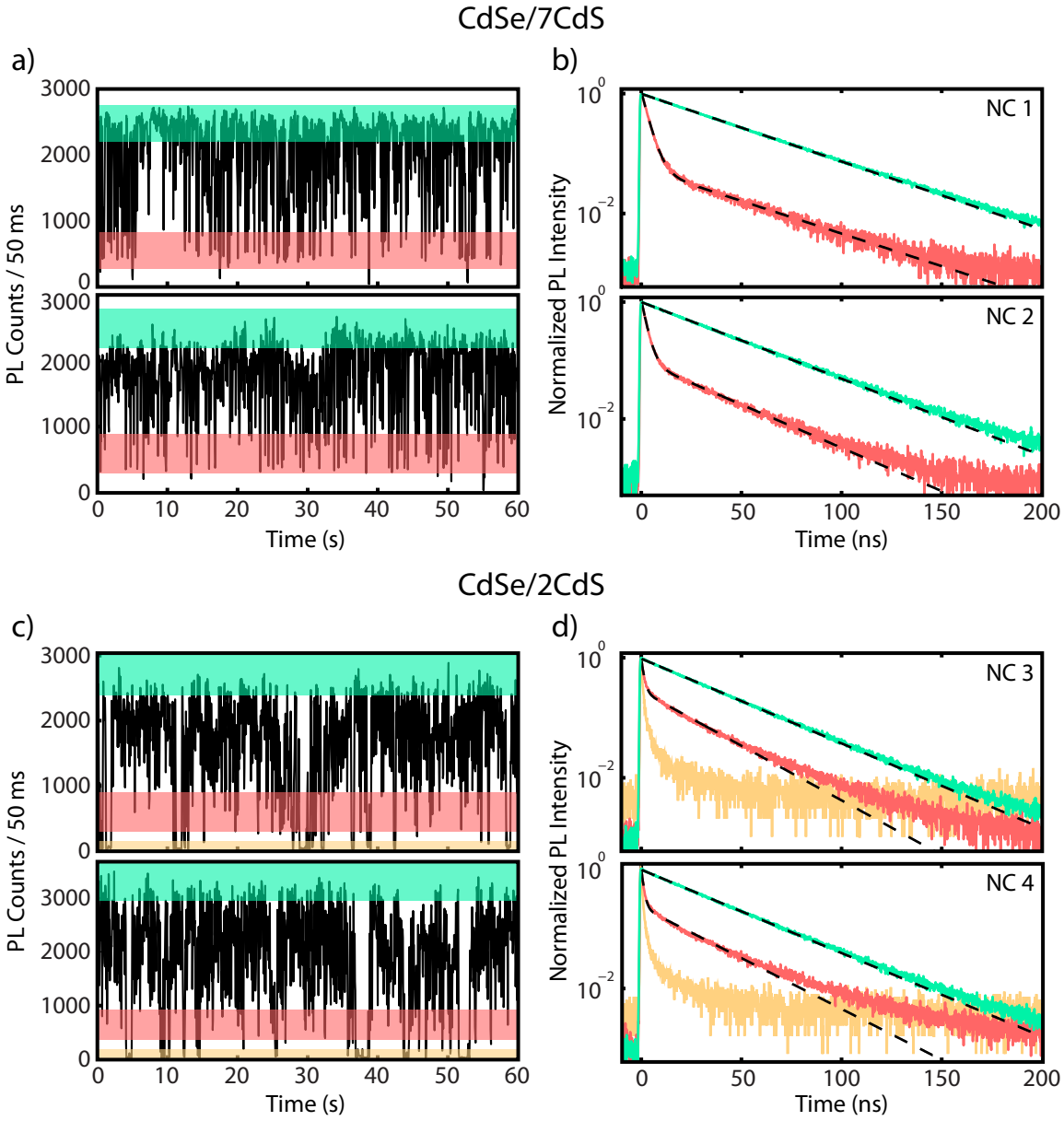

Figure 5-2: Comparison of a)-b) 7ML and c)-d) 2ML blinking and PL-intensity-sectioned decay dynamics. Thick-shelled CdSe/CdS nanocrystals have a slower trion emission rate than their thin-shell counterparts, but do not switch off as frequently. The off state of 2ML NCs is nearly equal to the detector dark count rate, and the decay (yellow) is IRF limited. Fits to mono- and bi-exponentials are shown as black dashed lines in b) and d). Lifetime fit parameters for all eight NCs are summarized in Table 5.1.

use the ratio of intensities to determine the trion QY [129]. If we further assume that for well-passivated 7ML nanocrystals a single process dominates trion non-radiative recombination k_{nr}^{T} (e.g. Auger recombination), then

$$\mathrm{QY}_{T} = \frac{k_{\mathrm{rad}}^{T}}{k_{\mathrm{rad}}^{T} + k_{\mathrm{nr}}^{T}} \approx 0.2, \tag{5.1}$$

$$\Rightarrow 4k_{\mathrm{rad}}^{T} = k_{\mathrm{nr}}^{T}. \tag{5.2}$$

From the extracted decay times in Table 5.1,

$$12\tau_{\mathrm{tot}}^{T} \approx \tau_{\mathrm{tot}}^{X} \tag{5.3}$$

$$\frac{12}{k_{\mathrm{rad}}^{T} + k_{\mathrm{nr}}^{T}} = \frac{1}{k_{\mathrm{rad}}^{X} + k_{\mathrm{nr}}^{X}} \approx \frac{1}{k_{\mathrm{rad}}^{X}} \tag{5.4}$$

$$\Rightarrow k_{\mathrm{rad}}^{T} = 12/5k_{\mathrm{rad}}^{X} = 2.4k_{\mathrm{rad}}^{X}. \tag{5.5}$$

A similar calculation for 7ML NC 2 gives $k_{\mathrm{rad}}^{T} \approx 1.9k_{\mathrm{rad}}^{X}$. A statistical scaling of trion radiative recombination pathways gives $k_{\mathrm{rad}}^{T} = 2k_{\mathrm{rad}}^{X}$, in close agreement with our experimentally determined relationship. This suggests that the approximations made above are not wholly unreasonable - in particular, it indicates that Auger recombination may indeed be the dominant quenching pathway for trions. It is difficult to speculate whether the dynamics we measure are for the positive or negative trion since our data cannot distinguish between the two - given that more sophisticated approaches [57, 33] on nominally similar samples remain contentious, we think it prudent to hold judgement on this issue for now.

From the rates above, we estimate $\tau_{\mathrm{Auger}}^{T} \approx 4$ ns for 7ML NC 1. The AR decay time is much slower than that measured in conventional CdSe-based NCs [66], but perhaps reflects the reduced Coulomb coupling in thick-shelled nanocrystals. Indeed, if the rates we extract reflect the true dynamics of CdSe/7CdS, rational shell synthesis may give us an exquisite handle on multiparticle interactions, dialing in the strength of Coulomb-mediated processes in a deterministic way.

5.2 An assessment of Type B blinking in CdSe NCs

Having characterized the grey state dynamics of individual CdSe/CdS NCs, we are better positioned to assess the prospects of anomalous blinking in both CdS and conventional-shell nanocrystals. As was reported by Galland and co-workers, thick-shell CdSe/CdS NCs exhibit both type A and type B blinking at zero bias in their electrochemical cell, with very short off periods ([42], supplementary information). They proposed the following mechanism to explain off state dynamics in type B blinking: upon exciting a single CdSe/CdS NC with above-band-gap excitation, the hot electron is trapped with a rate $k_{\text{trap}} \gg k_{\text{cool}}$, preventing the exciton from cooling to the band edge and radiatively recombining. This also requires that k_{trap} is the dominant quenching mechanism, with no competing non-radiative process at the band edge. They propose that the hot-electron trap is due to a surface state. In type A blinking, the opposite is true - competing kinetics are set up between a non-radiative process (surface trapping, Auger recombination, etc) and radiative emission.

To explain the differences between their data and others [37, 140, 116], Galland et al. make two testable hypotheses. First, they posit the emergence of type B must be shell-thickness-dependent, with thinner-shelled NCs more susceptible than thick-shell NCs. This is because of the surface state they assign to fast electron-trapping. Second, they suggest that while our group's results challenging the charging model for blinking in conventional CdSe/ZnS NCs are not consistent with type A blinking, they could be rationalized if these NCs exhibited type B blinking.

Since A and B blinking are supposed to occur in the same NC, measuring time-averaged lifetimes across the entire PL trace as a function of intensity is inadequate. Instead, we must calculate the instantaneous PL lifetime from photon detections in each time bin of the PL trace and look for correlated or uncorrelated fluctuations. Figure 5-3 depicts three hypothetical blinking scenarios and their corresponding fluorescence-lifetime-intensity distributions (FLIDs, shown in the inset). To determine which scenario best reflects CdSe/CdS NCs, we produce FLID data for individ-

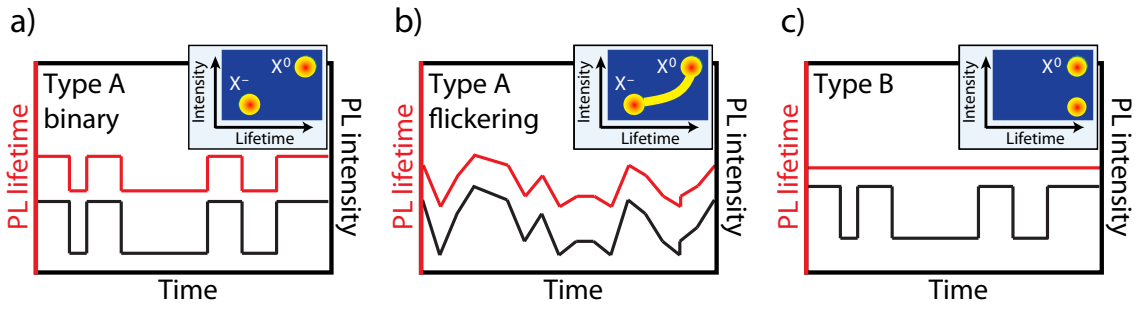

Figure 5-3: Hypothetical data for type A and B blinking. a), b) The PL intensity and instantaneous PL lifetime are correlated in type A. c) Type B blinking, with no change in PL lifetime as the NC switches between on and off states. Corresponding fluorescence-lifetime-intensity distributions (FLIDs) are shown as insets. Figure adapted from Ref. [42].

ual 2ML and 7ML NCs and test the first hypothesis outlined above. Next, we compare our CdSe/CdS data to that obtained from single conventional-CdSe nanocrystals, similar to the sample used in Zhao et al. [140].

5.2.1 Maximum-likelihood lifetime fitting

We briefly mention how instantaneous PL lifetimes were calculated both in Galland's and our FLID data. Due to the large number of bins in each PL trace (a 300 s intensity trace with 50 ms time-spacing has 6000 bins), it is impractical to use a leastsquares fitting approach for each bin of data. Instead, we rely on the maximum likelihood estimator (MLE) to estimate the PL lifetime [86, 132]. If we make the important assumption that the instantaneous lifetime can be approximated by a single exponential, the likelihood function is

$$L(\tau) = \prod_{i=1}^{m} \frac{1}{\tau} exp(-t_i/\tau). \tag{5.6}$$

The quantity of interest is the average lifetime, τ. We maximize $L(\tau)$ by solving $\frac{\partial L(\tau)}{\partial \tau} = 0$, giving

$$1 + \frac{1}{exp(T/\tau) - 1} - \frac{m}{exp(mT/\tau)} = \frac{1}{N} \sum_{i=1}^{m} iN_i. \tag{5.7}$$

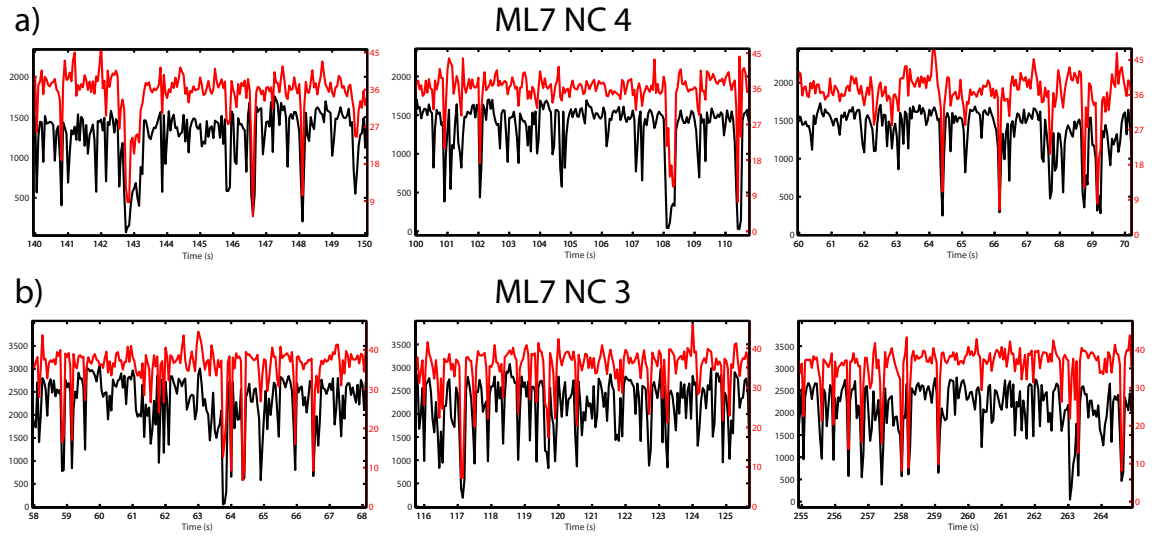

Figure 5-4: Representative PL lifetime (red) and intensity (black) traces for individual CdSe/7CdS nanocrystals. NC 4 (a, top three traces) and NC 3 (b, bottom three traces) both exhibit grey-state emission, with rare sojourns to the full off state. PL lifetime and intensity fluctuate in sync for both nanocrystals shown.

In our experiment, the average lifetime is usually longer than the time-resolution ($T \ll \tau$), and the lifetime decay is fully resolved within our observation time window ($mT \gg \tau$), allowing us to simplify Equation 5.7 and produce an expression for the average lifetime:

$$\hat{\tau} = \frac{1}{N} \sum_{i=1}^{m} (i-1) T N_i. \tag{5.8}$$

Here, we use $\hat{\tau}$ to indicate the maximum-likelihood estimate, and τ to indicate the true instantaneous lifetime. In practice, Equation 5.8 greatly speeds up the lifetime calculation - it is a simple average of the number of counts N_i that are detected in each lifetime bin i. In our calculations, we use 50 ms bin times to calculate $\hat{\tau}$, with a resolution of 1 ns

5.2.2 Thin and thick-shell CdSe/CdS nanocrystals

We collect photon arrival times from individual CdSe/7CdS (7ML) and CdSe/2CdS (2ML) nanocrystals and plot their PL intensity (black) and instantaneous PL lifetime (red) in Figure 5-4. Three 10-second subsections of the overall trace are shown for

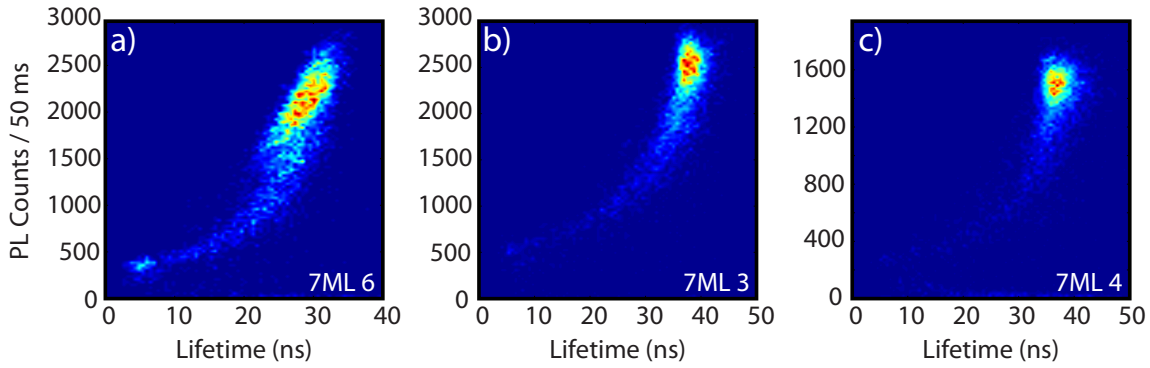

Figure 5-5: Fluorescence-lifetime-intensity distribution (FLID) plots for three representative CdSe/7CdS nanocrystals. Data for all three NCs (a-c) exhibits correlation reflective of type A flickering. NC 4 (c) exhibits less smearing, but this is due to majority emission from the bright state, with infrequent switching to the grey state.

ML7 NC 3 and 4. On average, the on state lifetime is approximately 35-40 ns for all ML7 NCs studied, in good agreement with our time-averaged data from the previous section (Table 5.1). Close inspection of the black and red traces shows fairly strong correlation between PL lifetime and PL intensity fluctuations, with the grey-state lifetime varying by a factor of two ($\approx$ 9-20 ns). To visualize the correlation for the entire PL trace (on average, we collected 300 s of photon arrival data for each NC studied), we construct FLIDs for three representative 7ML nanocrystals and show the results in Figure 5-5a-c. Referring back to the hypothetical scenarios outlined in Figure 5-3, the data from ML7 nanocrystals looks like it originated from type A 'flickering' NCs. In the case of ML NC 4 (Figure 5-5c, Figure 5-4a), infrequent switching to the grey state results in less smearing in the FLID data - for the most part, this NC emits from the bright state. We contrast these dynamics to the ones we measure for single CdSe/2CdS nanocrystals (Figure 5-6). Surprisingly, the FLID data for the NCs shown shows less correlation between PL intensity and the instantaneous lifetime - at first glance, this is suggestive of type B blinking as shown in the hypothetical data above (Figure 5-3c). However, examining the PL lifetime-PL intensity traces in Figure 5-7a suggests an alternative explanation. Figure 5-7 shows the blinking and lifetime trace, along with six PL lifetimes extracted at times given in the top-right portion of the plot (the light blue boxes in Figure 5-7a indicate which

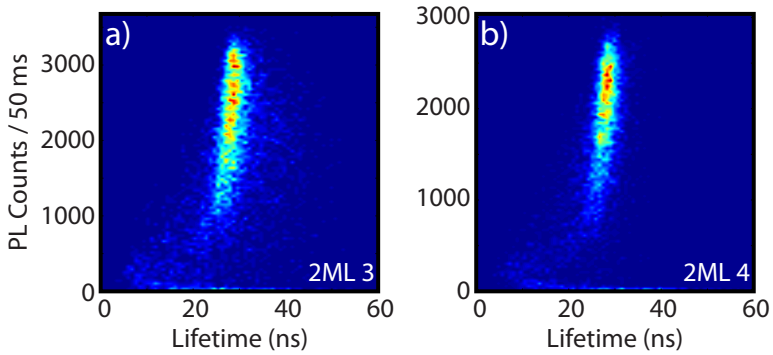

Figure 5-6: FLID plots for two representative CdSe/2CdS nanocrystals (a-b). Both sets of data look qualitatively different from our 7ML results shown above.

bins were used to calculate the six decays). At $t = 119$ s, the nanocrystal has a high PL intensity value (black trace) and the PL lifetime (Figure 5-7b, $t = 119$ s plot) reflects a realistic luminescence decay time of ca. 30 ns (red trace value in Figure 5-7a). However, a troubling issue arises for low PL intensity regions, presumably where the lifetime should not change from the on state value if type B blinking is occuring. The PL intensity at $t = 122.7$ s and $t = 125.3$ s (Figure 5-7a) is approximately the same ($\approx$ 500 counts/50 ms) - if both these events originated from type B blinking, their PL lifetime would be close to 30 ns (unchanged from the on state value), and the decays should *look* like the $t = 119$ s decay. Instead, both decays exhibit fast kinetics that are qualitatively different from real on state luminescence decay (Figure 5-7b). Moreover, the calculated MLE lifetimes for these two traces differ by 10 ns, 30% of the neutral exciton lifetime. This, in our opinion, results in an erroneously long lifetime being assigned to the $t = 125.3$ s point. We confirm that this incorrect lifetime estimation occurs throughout the PL intensity trace - when this data is subsequently correlated in the FLID shown in Figure 5-6b, one is led to believe that 2ML NC 4 exhibits type B blinking.

What leads to this experimental artifact in our 2ML data? Looking back at the assumptions made in Section 5.2.1, we see that the condition $T \ll \tau$ is not true for the fast decays that occur at $t = 122.7$ s and $t = 125.3$ s - the time resolution T is on the order of the true lifetime decay τ. As a result, the MLE calculation considers the uncorrelated background counts that occur at longer times part of a

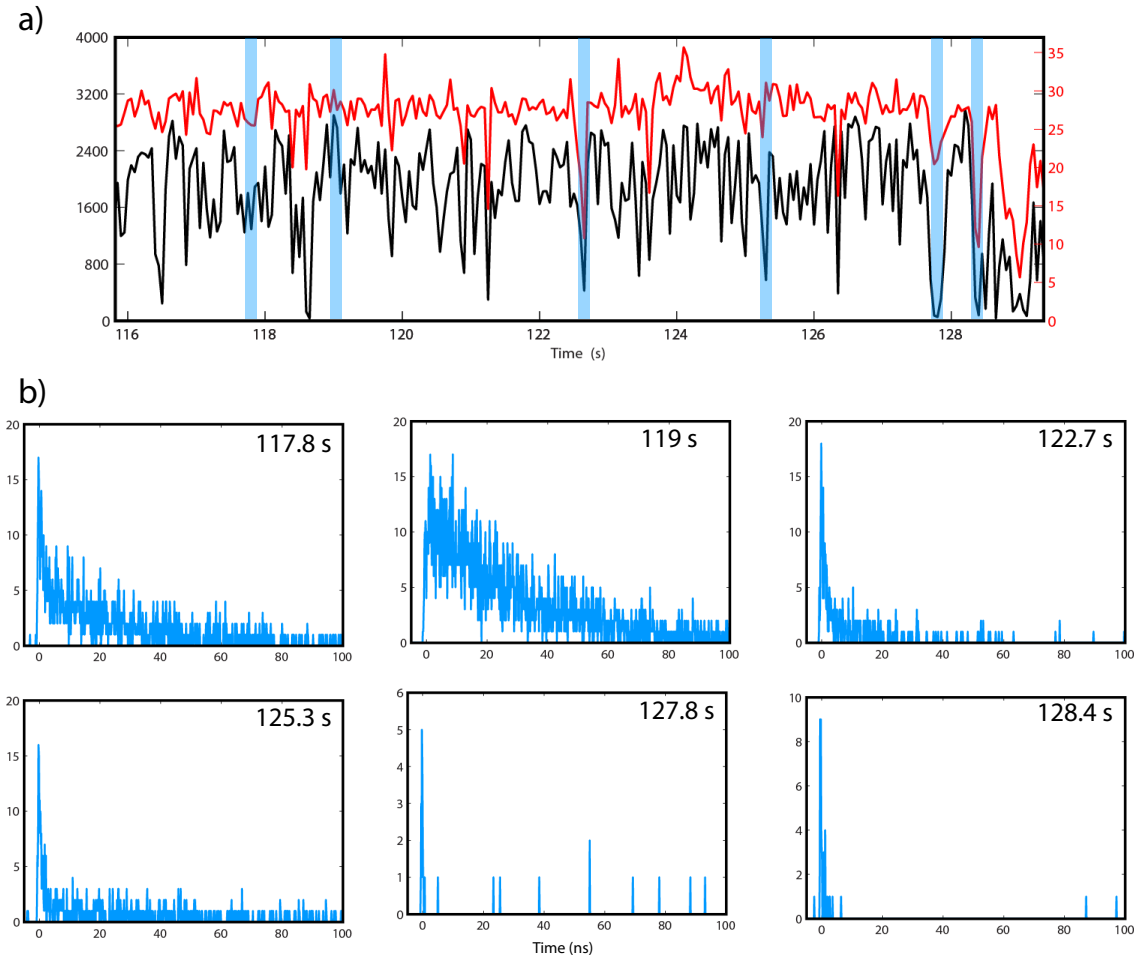

Figure 5-7: a) PL intensity (black) and PL lifetime (red) traces for 2ML NC 4. b) Six instantaneous PL lifetimes extracted from the single NC trace above, taken at times in the blinking trace indicated by the top-right number. The PL lifetime at $t = 119$ s resembles real luminescence. However, while the MLE-calculated PL lifetimes for $t = 122.7$ s and $t = 125.3$ s differ by 10 ns (ca. 30% of the neutral exciton lifetime), the difference in PL intensity negligible. This suggests that the MLE fitting method is not adequately capturing the true PL decay rate (see text).

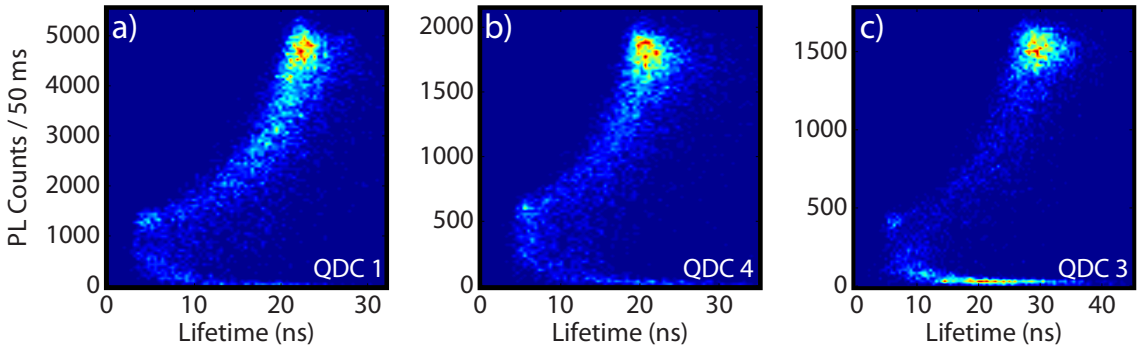

Figure 5-8: FLID data for three representative QD Corp. nanocrystals - all three show strong correlation between PL intensity and PL lifetime.

'long lifetime' decay, and depending on the distribution of detection events within the lifetime window, produces a $\hat{\tau}$ that oftentimes does not reflect the true lifetime τ. In fact, in the limit of low signal ($S/N \to 0$), $\hat{\tau} > \tau$, biasing the estimated lifetime.

5.2.3 Comparison to QD Corp nanocrystals

To test the second hypothesis suggested by the Galland work, we perform the same experiment on QD Corp 655 nanocrystals and calculate FLID data for a number of single NCs studied (Figure 5-8). QDC NCs were the workhorse of single NC experiments due to their exceptional photostability and high ensemble PL quantum yield, allowing different research groups to study nominally similar samples. These NCs were also used in Ref. [140], specifically cited by Galland et al. as a material system likely to exhibit type B blinking. The calculated FLID data for representative QDC NCs shows otherwise - all three datasets shown in Figure 5-8 show a strong correlation between PL intensity and instantaneous lifetime. QDC NCs, unlike CdSe/CdS NCs, are more likely to switch completely off for long periods of time [127]. This is seen in the FLID data - at very low PL intensities (0-100 PL Counts/50ms), no fluorescence is detected from the off state. As a result, the PL lifetime decay is flat, giving an average lifetime $\hat{\tau}$ that is larger than the IRF-limited lifetime. This results in a smearing of PL lifetime values in the FLID. Comparing the PL intensity and lifetime traces directly to each other as was done for 2ML nanocrystals (Figure 5-7) reveals no artifacts in the lifetime fitting - as far as we can tell, QDC NCs exhibit

type A blinking.

5.2.4 Interpretation of PL blinking mechanisms

Starting with the first observation of fluorescence from single CdSe nanocrystals [98], the blinking puzzle has rallied a legion of scientists to understand the microscopic processes responsible for on-off switching. Each new experiment has added to our knowledge of what may or may not be occuring to quantum-confined excitons upon photoexcitation of a single NC, and has advanced the state of the field considerably over the past 17 years. Therefore, when a new and unexpected phenomenon is discovered at the single NC level, it is greeted with wonderment [48]. This is especially the case for blinking.

In our experiments, we sought to test the hypotheses put forward by the new results of Galland et al. [42], and looked to see if type B blinking was a general process that occurs under neutral conditions. The FLID data for all three material systems studied here (2ML, 7ML and QDC NCs) instead suggests that conventional type A blinking dominates. While it is not known whether the Galland data suffers from similar artifacts as seen by us in the 2ML FLIDs, it does warrant a closer inspection of how lifetimes are calculated by the commercial software used in their paper. For example, if a threshold was set to discount fast decay, or if the assumptions made about MLE fitting were not true for off-state decays (see Section 5.2.2 for more details), this could lead to concerns analogous to our own. However, we do not completely discount the possibility of a new blinking mechanism *a priori*: now, what is required is more experiments to fully disentangle the photophysics of NCs that exhibit type B blinking, especially under neutral conditions. The electrochemical charging experiments of Galland et al. are a refreshing direction for single NC investigations, and will surely provide the nanoscience community with more information to pore over.

The blinking dynamics we observe in the new generation of CdSe/CdS NCs are intriguing in their own right. For thick-shell CdSe/7CdS, an off state equal to the detector dark count rate is rarely, if at all, seen. Instead, 7ML NCs exhibit high

on-fractions with radiation most likely from single neutral exciton recombination. Switching to a grey state, which our kinetic analysis suggests is a trion, occurs infrequently. Our observations are consistent with the hypothesis that a thick CdS shell can slow down Auger recombination - for the 7ML NC we investigated in detail, we extract an AR time constant on the order of nanoseconds, versus the few hundred picoseconds usually measured for conventional NCs like QDCorp 655. This grey-state is reduced in intensity when we study thinner shelled CdSe/2CdS NCs - here, the nanocrystal PL trace has off periods equal in intensity to the detector dark count rate, occasionally emitting from a grey state. Comparing 2ML and 7ML NCs, having a thicker shell does seem to suppress the fully off state. If we assume the quality of the core-shell interface is roughly the same for these two samples, this implicates a potential surface-mediated effect for the off state in CdSe/2CdS NCs. The lifetime we measure from the low PL period is very fast, and therefore is unlikely caused by the same kind of surface state Galland et al. call upon to explain type B blinking, where no change in lifetime occurs. The fast off-state kinetics from CdSe/2CdS suggest that whatever the quenching mechanism is, it competes efficiently with band edge recombination and sets up the branching kinetics seen in other NCs exhibiting type A behavior.

Chapter 6

Concluding remarks

The overriding concern of this thesis is the study of excitons in quantum-confined colloidal nanostructures, with a heavy emphasis on new materials that display optical activity in the shortwave-infrared (SWIR). Key to these studies was new tool development: by combining our expertise in optical microscopy with very efficient superconducting nanowire single photon detectors, we successfully realized a working SWIR fluorescence microscope that operates under ambient conditions [24]. So what have we learned?

6.1 Conclusions of this thesis work

In our first experiments on individual lead sulfide nanocrystals, we discovered that the process of fluorescence intermittency is present in PbS/CdS NCs. This observation was somewhat expected - almost every fluorophore studied to date has exhibited PL blinking in one form or another [40]. What intrigues us is that the on and off waiting-time statistics measured from single PbS nanocrystals is identical to those seen in conventional CdSe-based nanomaterials. The electronic structure of PbS is dramatically different from CdSe - a much larger dielectric constant, a smaller band gap originated from L-point as opposed to the Γ-point (CdSe), even a different crystal structure (rock salt versus wurtzite or zinc blende). Our results suggest that the blinking mechanism in PbS/CdS is likely tied to surface or defect states that trap

and quench the exciton emission rapidly, rather than intrinsic electronic properties.

Second, we find that the statistics of light emission from PbS nanocrystals is sub-Poissonian, demonstrated by a deep antibunching in the $g^{(2)}$ intensity autocorrelation data. This experiment confirmed that we were indeed interrogating single nanocrystals - while two-state blinking is a strong indicator for single NC localization, also measuring a $g^{(2)} < 0.5$ strengthens the assertion.

Encouraged by our ability to measure $g^{(2)}$ autocorrelations from a single SWIR emitter, we investigated single InAs/CdZnS nanocrystals with pulsed excitation. We discovered complex blinking dynamics, oftentimes analogous to the behavior reported from single CdSe/CdS NCs. Having found a previously unmeasured grey state in InAs NCs, we measured the kinetics of emission and discovered to our surprise that the bright and grey states emit at the same rate. In fact, all InAs/CdZnS NCs we studied exhibited one of two types of blinking: PL blinking where the lifetime was faster for lower-PL intensity periods (type I), and PL blinking where the lifetime remained constant for all intensities other than the off state (type II).

We quantified the distribution of 'maximum' lifetimes across our sample and found it to be quite broad, a feature we attribute to varying shell thickness. Interestingly, measuring $g^{(2)}$ on the same NCs revealed a near-zero biexciton quantum yield for all but one NC. The low biexciton quantum yield reflects an efficient multi-exciton quenching mechanism within InAs nanocrystals - this is in contrast to experiments conducted in the visible, where within a single batch of core-shell nanocrystals (i.e. CdSe/CdS, or CdSe/ZnS), a distribution in biexciton yields is commonly measured.

In the visible portion of this thesis, we determined that CdSe/7CdS NCs (7ML) can on occasion produce fast grey-state emission, which our kinetic analysis suggests is due to trion radiative recombination. Based on this analysis, we found a surprisingly slow Auger recombination time in a 7ML NC, on the order of a few nanoseconds. In conventional CdSe/ZnS nanocrystals, this decay time is usually a few hundred picoseconds. Preliminary studies on thick and thin-shell CdSe/CdS NCs, as well as on QD Corp 655 nanocrystals, indicate that all three material systems exhibit type A blinking (type I in our terminology, type A in Galland et al. [42]). Nanocrystals that

switch completely off have a corresponding lifetime that is very fast - one must be careful that the algorithm used to fit the lifetimes accounts for this fast decay. The FLID analysis is a useful way to correlate PL intensity and lifetime dynamics, and we recommend its use when the occasion arises.

6.2 An outlook on the future

Even from the limited data presented in this thesis, it is clear that single nanocrystal spectroscopy is still a rich and vibrant topic of research. We conclude this chapter with an outlook on future directions in single NC investigations, with a special emphasis on the shortwave-infrared:

1. The data we present has carefully studied the intensity dynamics of single SWIR NCs, a crucial first step. We envision true single NC *spectroscopy* as the next grand challenge. Measuring the **spectral properties of single lead chalcogenide** NCs will almost certainly reveal new physics - the ensemble linewidths of PbS NCs are much broader than PbSe, and preliminary studies cannot solely attribute the difference to greater size polydispersity in PbS synthesis. The dephasing time for band edge excitons in PbS NCs has been measured and it is very fast, on the order of hundreds of femtoseconds [85]. This hints at a rather large homogeneous linewidth, one which we might be able to measure using photon-correlation Fourier spectroscopy (PCFS) [83].

2. Performing single NC experiments with a **SNSPD array** would be most beneficial, especially if the detector has >100 detection elements. Spectrally dispersing the emission from a single NC and performing single photon counting as a function of energy would allow us to watch cascading energy flow - for example, monitoring multi- and single-exciton emission at the same time, from the same NC, as has been done with streak cameras in the visible [35].

3. It would be prudent to **extend the range of SWIR-active systems** studied using our unique apparatus. For example, carbon nanotubes can be synthe-

sized to produce SWIR emission, and have undergone single tube interrogation in the visible. One barrier is the low quantum yield of these materials compared to SWIR nanocrystals, but this has mostly been attributed to bundling of quenching metallic and emitting semiconducting nanotubes. Improvements in synthetic protocols and purification methods should be able to solve this problem, if it has not already. In a similar vein, the low radiative rate of PbS NCs has hampered our efforts to pursue pulsed excitation experiments on the lead chalcogenide NCs. Colloidal nanoplatelets have been shown to have very fast radiative rates, on the order of a few hundred picoseconds - synthesizing platelets out of SWIR-active materials would be most exciting. Reports do exist of 2D PbS 'nanosheets', but it is unclear if these exhibit the same optical properties as platelets. One strategy might be to attempt platelet synthesis from a cation-labile material like copper sulfide, and perform an ion exchange to produce PbS platelets, as is commonly done for PbS nanorod synthesis.

4. Moving beyond single NCs (gasp), combining SWIR spectroscopy with functioning nanocrystal photovoltaic or light-emitting devices is an exciting direction our group has already begun. More of this is necessary, especially with time-resolved PL. One could ask the question: **can we correlate features in a photovoltaic J-V curve to intrinsic nanocrystal film photophysics?** If this turns out to be true, we will finally be able to move beyond the trial-and-error that currently limits device improvement.

Finally, we encourage a bridge between single and mesoscopic NC experiments. With synthetic advances bringing the problem of visible-NC blinking to an empirical end, the time is right to start probing the photophysics of well-defined arrays, or clusters of nanocrystals. This is a challenging task. It requires deterministic manipulation of nanometer-sized crystals. It requires new photonic methods to couple excitation light to one NC and watch the emission from its neighbor. It requires new theory to move beyond single NC electronic structure and consider nearest-neighbor interactions. It requires new nanocrystals, new ligands, and new ideas. This is a

challenging task. But isn't this why we are here?

Bibliography

[1] J. M. An, A. Franceschetti, S. V. Dudiy, and A. Zunger. The peculiar electronic structure of pbse quantum dots. *Nano Lett.*, 6:2728–2735, 2006.

[2] N. W. Ashcroft and N. D. Mermin. *Solid State Physics*. Saunders College Publishing, 1976.

[3] Plenio M. B. and P. L. Knight. The quantum-jump approach to dissipative dynamics in quantum optics. *Rev. Mod. Phys.*, 70:101–144, 1998.

[4] U. Banin, Y. W. Cao, D. Katz, and O. Millo. Identification of atomic-like electronic states in indium arsenide nanocrystal quantum dots. *Nature*, 400:542–544, 1999.

[5] U. Banin, C. J. Lee, A. A. Guzelian, A. V. Kadavanich, A. P. Alivisatos, W. Jaskolski, G. W. Bryant, A. L. Efros, and M. Rosen. Size-dependent electronic level structure of inas nanocrystal quantum dots: Test of multiband effective mass theory. *J. Chem. Phys.*, 109:2306–2309, 1998.

[6] U. Banin and O. Millo. Tunneling and optical spectroscopy of semiconductor nanocrystals. *Annu. Rev. Phys. Chem.*, 54:465–492, 2003.

[7] E. Barkai, F. L. H. Brown, M. Orrit, and H. Yang, editors. *Theory And Evaluation Of Single-Molecule Signals*. World Scientific, 2008.

[8] E. Barkai, Y. Jung, and R. Silbey. Theory of single-molecule spectroscopy: Beyond the ensemble average. *Annu. Rev. Phys. Chem.*, 55:457–507, 2004.

[9] T. Basche, S. Kummer, and C. Brauchle. Direct spectroscopic observation of quantum jumps of a single-molecule. *Nature*, 373:132–134, 1995.

[10] M. Ben-Lulu, D. Mocatta, U. Banin, and S. Ruhman. On the absence of detectable carrier multiplication in a transient absorption study of inas/cdse/znse core/shell1/shell2 quantum dots. *Nano Lett.*, 8:1207–1211, 2008.

[11] L. Biadala, Y. Louyer, P. Tamarat, and B. Lounis. Band-edge exciton fine structure of single cdse/zns nanocrystals in external magnetic fields. *Phys. Rev. Lett.*, 105:157402, 2010.

[12] W. Bludau, A. Onton, and W. Heinke. Temperature dependence of the band gap of silicon. *J. Appl. Phys.*, 45:1846–1848, 1974.

[13] C. Bradac, T. Gaebel, N. Naidoo, M. J. Sellars, J. Twamley, L. J. Brown, A. S. Barnard, T. Plakhotnik, A. V. Zvyagin, and J. R. Rabeau. Observation and control of blinking nitrogen-vacancy centres in discrete nanodiamonds. *Nature Nanotech.*, 5:345–349, 2010.

[14] X. Brokmann, L. Coolen, M. Dahan, and J.-P. Hermier. Measurement of the radiative and nonradiative decay rates of single cdse nanocrystals through a controlled modification of their spontaneous emission. *Phys. Rev. Lett.*, 93:107403, 2004.

[15] X. Brokmann, E. Giacobino, M. Dahan, and J. P. Hermier. Highly efficient triggered emission of single photons by colloidal cdse/zns nanocrystals. *Appl. Phys. Lett.*, 85:712–714, 2004.

[16] S. Brovelli, R. D. Schaller, S. A. Crooker, F. García-Santamaría, Y. Chen, R. Viswanatha, J. A. Hollingsworth, H. Htoon, and V. I. Klimov. Nano-engineered electronhole exchange interaction controls exciton dynamics in core-shell semiconductor nanocrystals. *Nat. Commun.*, 2:280, 2011.

[17] L. E. Brus. Electron electron and electron-hole interactions in small semiconductor crystallites - the size dependence of the lowest excited electronic state. *J. Chem. Phys.*, 80(9):4403–4409, 1984.

[18] L. Cademartiri, E. Montanari, G. Calestani, A. Migliori, A. Guagliardi, and G. A. Ozin. Size-dependent extinction coefficients of pbs quantum dots. *J. Am. Chem. Soc.*, 128(31):10337–10346, 2006.

[19] M. Califano. Direct and inverse auger processes in inas nanocrystals: Can the decay signature of a trion be mistaken for carrier multiplication? *ACS Nano*, 3:2706–2714, 2009.

[20] O. Chen, J. Zhao, V. P. Chauhan, J. Cui, C. Wong, D. K. Harris, H. Wei, H.-S. Han, D. Fukumura, R. K. Jain, and M. G. Bawendi. Compact high-quality cdsecds coreshell nanocrystals with narrow emission linewidths and suppressed blinking. *Nature Mater.*, 12:445–451, 2013.

[21] P. Chen, X. Zhou, H. Shen, N. M. Andoy, K.-S. Choudhary, G. Han, G. Liu, and W. Meng. Single-molecule fluorescence imaging of nanocatalytic processes. *Chem. Soc. Rev.*, 39:4560–4570, 2010.

[22] Y. Chen, J. Vela, H. Htoon, J. L. Casson, D. J. Werder, D. A. Bussian, V. I. Klimov, and J. A. Hollingsworth. "giant" multishell cdse nanocrystal quantum dots with suppressed blinking. *J. Am. Chem. Soc.*, 130:5026–5027, 2008.

[23] A. A. Cordones and S. R. Leone. Mechanisms for charge trapping in single semiconductor nanocrystals probed by fluorescence blinking. *Chem. Soc. Rev.*, 42:3209–3221, 2013.

[24] R. E. Correa, E. A. Dauler, G. Nair, S. H. Pan, D. Rosenberg, A. J. Kerman, R. J. Molnar, X. L. Hu, F. Marsili, V. Anant, K. K. Berggren, and M. G. Bawendi. Single photon counting from individual nanocrystals in the infrared. *Nano Lett.*, 12:2953–2958, 2012.

[25] C. H. Crouch, O. Sauter, X. Wu, R. Purcell, C. Querner, M. Drndic, and M. Pelton. Facts and artifacts in the blinking statistics of semiconductor nanocrystals. *Nano Lett.*, 10:1692–1698, 2010.

[26] R. M. Dickson, A. B. Cubitt, R. Y. Tsien, and W. E. Moerner. On/off blinking and switching behavior of single green fluorescent protein molecules. *Nature*, 388:355–358, 1997.

[27] A. L. Efros and M. Rosen. The electronic structure of semiconductor nanocrystals. *Annu. Rev. Mater. Sci.*, 30:475–521, 2000.

[28] A. L. Efros, M. Rosen, M. Kuno, M. Nirmal, D. J. Norris, and M. Bawendi. Band-edge exciton in quantum dots of semiconductors with a degenerate valence band: Dark and bright exciton states. *Phys. Rev. B*, 54(7):4843–4856, 1996.

[29] M. D. Eisaman, J. Fan, A. Migdall, and S. V. Polyakov. Single-photon sources and detectors. *Rev. Sci. Instrum.*, 82:071101, 2011.

[30] S. A. Empedocles, D. J. Norris, and M. G. Bawendi. Photoluminescence spectroscopy of single cdse nanocrystallite quantum dots. *Phys. Rev. Lett.*, 77(18):3873–3876, 1996.

[31] S.A. Empedocles and M. G. Bawendi. Quantum-confined stark effect in single cdse nanocrystallite quantum dots. *Science*, 278:2114–2117, 1997.

[32] S.A. Empedocles and M. G. Bawendi. Influence of spectral diffusion on the line shapes of single cdse nanocrystallite quantum dots. *J. Phys. Chem. B*, 103:1826–1830, 1999.

[33] M. J. Fernee, C. Sinito, Y. Louyer, C. Potzner, T. L. Nguyen, P. Mulvaney, P. Tamarat, and B. Lounis. Magneto-optical properties of trions in non-blinking charged nanocrystals reveal an acoustic phonon bottleneck. *Nat. Commun.*, 3:1287, 2012.

[34] M. J. Fernee, P. Tamarat, and B. Lounis. Cryogenic single-nanocrystal spectroscopy: Reading the spectral fingerprint of individual cdse quantum dots. *J. Phys. Chem. Lett.*, 4:609–618, 2013.

[35] B. R. Fisher. *Time Resolved Fluorescence of CdSe Nanocrystals using Single Molecule Spectroscopy.* PhD thesis, Massachussetts Institute of Technology, 2005.

[36] B. R. Fisher, J-M. Caruge, D. Zehnder, and M. G. Bawendi. Room-temperature ordered photon emission from multiexciton states in single cdse core-shell nanocrystals. *Phys. Rev. Lett.*, 94:087403, 2005.

[37] B. R. Fisher, H. J. Eisler, N. E. Stott, and M. G. Bawendi. Emission intensity dependence and single-exponential behavior in single colloidal quantum dot fluorescence lifetimes. *J. Phys. Chem. B*, 108(1):143–148, 2004.

[38] M. Fox. *Quantum Optics: An Introduction (Oxford Master Series in Physics, 6).* Oxford University Press, 2006.

[39] A. Franceschetti, L.-W. Wang, H. Fu, and A. Zunger. Short-range versus long-range electron-hole exchange interactions in semiconductor quantum dots. *Phys. Rev. B*, 58:13367–13370, 1998.

[40] P. Frantsuzov, M. Kuno, B. Jankó, and R. A. Marcus. Universal emission intermittency in quantum dots, nanorods and nanowires. *Nature Phys.*, 4:519–522, 2008.

[41] P. Frantsuzov, S. Volkan-Kacso, and B. Janko. Model of fluorescence intermittency of single colloidal semiconductor quantum dots using multiple recombination centers. *Phys. Rev. Lett.*, 103:207402, 2009.

[42] C. Galland, Y. Ghosh, A. Steinbruck, M. Sykora, J. A. Hollingsworth, V. I. Klimov, and H. Htoon. Two types of luminescence blinking revealed by spectroelectrochemistry of single quantum dots. *Nature*, 479:203–207, 2011.

[43] F. García-Santamaría, Y. Chen, J. Vela, R. D. Schaller, J. A. Hollingsworth, and V. I. Klimov. Suppressed auger recombination in "giant" nanocrystals boosts optical gain performance. *Nano Lett.*, 9:3482–3488, 2009.

[44] G. N. Gol'tsman, O. Okunev, G. Chulkova, A. Lipatov, A. Semenov, K. Smirnov, K. Voronov, A. Dzardanov, C. Williams, and R. Sobolewski. Picosecond superconducting single-photon optical detector. *Appl. Phys. Lett.*, 79:705–707, 2001.

[45] D. E. Gomez, M. Califano, and P. Mulvaney. Optical properties of single semiconductor nanocrystals. *Phys. Chem. Chem. Phys.*, 8:4989–5011, 2006.

[46] D. E. Gomez, J. van Embden, P. Mulvaney, M. J. Fernee, and H. Rubinsztein-Dunlop. Exciton-trion transitions in single cdse-cds core-shell nanocrystals. *ACS Nano*, 3:2281–2287, 2009.

[47] G. A. Grinbom, M. Saraf, C. Saguy, A. C. Bartnik, F. Wise, and E. Lifshitz. Density of states in a single pbse/pbs core-shell quantum dot measured by scanning tunneling spectroscopy. *Phys. Rev. B*, 81:245301, 2010.

[48] P. Guyot-Sionnest. A new quantum state? *Nature Mater.*, 4(9):653–654, 2005.

[49] R. H. Hadfield. Single-photon detectors for optical quantum information applications. *Nature Photon.*, 3:696–705, 2009.

[50] R. H. Hadfield, M. J. Stevens, R. P. Mirin, and S. W. Nam. Single-photon souce characterization with twin infrared-sensitive superconducting single-photon detectors. *J. Appl. Phys.*, 101:103104, 2007.

[51] C. W. Hamilton. Private communication.

[52] S. W. Hell and A. Schonle. *Biomedical Optical Imaging*. Oxford University Press, 2009.

[53] J. H. Hodak, C. D. Downey, J. L. Fiore, A. Pardi, and D. J. Nesbitt. Docking kinetics and equilibrium of a gaaa tetraloop-receptor motif probed by single-molecule fret. *Proc. Natl. Acad. Sci. U. S. A.*, 102:10505–10510, 2005.

[54] J. A. Hollingsworth. Heterostructuring nanocrystal quantum dots toward intentional suppression of blinking and auger recombination. *Chem. Mater.*, 25:1318–1331, 2013.

[55] B. Huang, M. Bates, and X. Zhuang. Super-resolution fluorescence microscopy. *Annu. Rev. Biochem.*, 78:993–1016, 2009.

[56] J. D. Jackson. *Classical Electrodynamics*. Wiley, 1998.

[57] C. Javaux, B. Mahler, B. Dubertret, A. Shabaev, A. V. Rodina, A. L. Efros, D. R. Yakovlev, F. Liu, M. Bayer, G. Camps, L. Biadala, S. Buil, X. Quelin, and J. P. Hermier. Thermal activation of non-radiative auger recombination in charged colloidal nanocrystals. *Nature Nanotech.*, 8:206–212, 2013.

[58] P. P. Jha and P. Guyot-Sionnest. Trion decay in colloidal quantum dots. *ACS Nano*, 3:1011–1015, 2009.

[59] P. Kambhampati. Hot exciton relaxation dynamics in semiconductor quantum dots: Radiationless transitions on the nanoscale. *J. Phys. Chem. C.*, 115:22089–22109, 2011.

[60] J. W. Kamplain and Z. Zhu. Us patent 61/421,164, december 8, 2010, 2012.

[61] A. J. Kerman. Superconducting nanowire photon-counting detectors for optical communications. *Lincoln Laboratory Journal*, 16:217–224, 2006.

[62] A. J. Kerman, E. A. Dauler, W. E. Keicher, J. K. W. Yang, K. K. Berggren, G. Gol'tsman, and B. Voronov. Kinetic-inductance-limited reset time of superconducting nanowire photon counters. *Appl. Phys. Lett.*, 88:111116, 2006.

[63] T. H. Kim, K. S. Cho, E. K. Lee, S. J. Lee, J. Chae, J. W. Kim, D. H. Kim, J. Y. Kwon, G. Amaratunga, S. Y. Lee, B. L. Choi, Y. Kuk, J. M. Kim, and K. Kim. Full-color quantum dot displays fabricated by transfer printing. *Nature Photon.*, 5:176–182, 2011.

[64] H. J. Kimble, M. Dagenais, and L. Mandel. Photon antibunching in resonance fluorescence. *Phys. Rev. Lett.*, 39:691, 1977.

[65] C. Kittel. *Quantum Theory of Solids*. WIley, 1987.

[66] V. I. Klimov, A. A. Mikhailovsky, D. W. McBranch, C. A. Leatherdale, and M. G. Bawendi. Quantization of multiparticle auger rates in semiconductor quantum dots. *Science*, 287(5455):1011–1013, 2000.

[67] M. Kuno. *Band edge spectroscopy of CdSe quantum dots*. PhD thesis, Massachusetts Institute of Technology, 1998.

[68] M. Kuno, D.P. Fromm, H.F. Hafmann, A. Gallagher, and D.J. Nesbitt. Nonexponential "blinking" kinetics of single cdse quantum dots: A universal power law behavior. *J. Chem. Phys.*, 112(7):3117, 2000.

[69] O. Labeau, P. Tamarat, and B. Lounis. Temperature dependence of the luminescence lifetime of single cdse/zns quantum dots. *Phys. Rev. Lett.*, 90:257404, 2003.

[70] K. G. Lee, H. Eghlidi, P. Kukura, R. Lettow, A. Renn, V. Sandoghdar, and S. Gotzinger. A planar dielectric antenna for directional single-photon emission and near-unity collection efficiency. *Nature Photon.*, 5:166–169, 2011.

[71] E. Lhuillier, S. Keuleyan, H. Liu, and P. Guyot-Sionnest. Mid-ir colloidal nanocrystals. *Chem. Mater.*, 25:1272–1282, 2013.

[72] P. Liljeroth, P. A. Z. van Emmichoven, S. G. Hickey, H. Weller, B. Grandidier, G. Allan, and D. Vanmaekelbergh. Density of states measured by scanning-tunneling spectroscopy sheds new light on the optical transitions in pbse nanocrystals. *Phys. Rev. Lett.*, 95:086801, 2005.

[73] R. Loudon. *The quantum theory of light*. Oxford University Press, Great Clarendon Street, Oxford OX2 6DP, 2000.

[74] B. Lounis, H.A. Bechtel, D. Gerion, P. Alivisatos, and W. E. Moerner. Photon antibunching in single cdse/zns quantum dot fluorescence. *Chem. Phys. Lett.*, 329:399–404, 2000.

[75] B. Lounis and W. E. Moerner. Single photons on demand from a single molecule at room temperature. *Nature*, 407:491–493, 2000.

[76] W. Lukosz. Light-emission by magnetic and electric dipoles close to a plane interface. iii. radiation patterns of dipoles with arbitrary orientation. *J. Opt. Soc. Am.*, 69:1495–1503, 1979.

[77] W. Lukosz and R. E. Kunz. Light-emission by magnetic and electric dipoles close to a plane interface. i. total radiated power. *J. Opt. Soc. Am.*, 67:1607–1615, 1977.

[78] W. Lukosz and R. E. Kunz. Light-emission by magnetic and electric dipoles close to a plane interface. ii. radiation patterns of perpendicular oriented dipoles. *J. Opt. Soc. Am.*, 67:1615–1619, 1977.

[79] J.-W. Luo, G. Bester, and A. Zunger. Long- and short-range electronhole exchange interaction in different types of quantum dots. *New J. Phys.*, 11:123024, 2009.

[80] B. Mahler, P. Spinicelli, S. Buil, X. Quelin, J.-P. Hermier, and B. Dubertret. Towards non-blinking colloidal quantum dots. *Nature Mater.*, 7:659–664, 2008.

[81] A. V. Malko, Y.-S. Park, S. Sampat, C. Galland, J. Vela, Y. Chen, J. A. Hollingsworth, V. I. Klimov, and H. Htoon. Pump-intensity- and shell-thickness-dependent evolution of photoluminescence blinking in individual core/shell cdse/cds nanocrystals. *Nano Lett.*, 11:5213–5218, 2011.

[82] L. F. Marshall. *Spectral dynamics of single quantum dots: A study using photon-correlation Fourier Spectroscopy for submillisecond time resolution at low temperature and in solution.* PhD thesis, Massachusetts Institute of Technology, 2011.

[83] L. F. Marshall, J. Cui, X. Brokmann, and M. G. Bawendi. Extracting spectral dynamics from single chromophores in solution. *Phys. Rev. Lett.*, 105:053005, 2010.

[84] F. Marsili, V. B. Verma, J. A. Stern, S. Harrington, A. E. Lita, T. Gerrits, B. Vayshenker, B. Baek, M. D. Shaw, R. P. Mirin, and S. W. Nam. Detecting single infrared photons with 93 *Nature Photon.*, 7:210–214, 2013.

[85] F. Masia, W. Langbein, I. Moreels, Z. Hens, and P. Borri. Exciton dephasing in lead sulfide quantum dots by x-point phonons. *Phys. Rev. B*, 83:201309, 2011.

[86] M. Maus, M. Cotlet, J. Hofkens, T. Gensch, F. C. De Schryver, J. Schaffer, and C. A. M. Seidel. An experimental comparison of the maximum likelihood estimation and nonlinear least squares fluorescence lifetime analysis of single molecules. *Anal. Chem.*, 73:2078–2086, 2001.

[87] J. A. McGuire, J. Joo, J. M. Pietryga, R. D. Schaller, and V. I. Klimov. New aspects of carrier multiplication in semiconductor nanocrystals. *Acc. Chem. Res.*, 41:1810–1819, 2008.

[88] X. Michalet, A. N. Kapanidis, T. Laurence, F. Pinaud, S. Doose, M. Pflughoefft, and S. Weiss. The power and prospects of fluorescence microscopies and spectroscopies. *Annu. Rev. Biophys. Biomol. Struct.*, 32:161–182, 2003.

[89] P. Michler, A. Imamo˘ glu, M. D. Mason, P. J. Carson, G. F. Strouse, and S. K. Buratto. Quantum correlation among photons from a single quantum dot at room temperature. *Nature*, 406:968–970, 2000.

[90] D. Mocatta, G. Cohen, J. Schattner, O. Millo, E. Rabani, and U. Banin. Heavily doped semiconductor nanocrystal quantum dots. *Science*, 332:77–81, 2011.

[91] W. E. Moerner. A dozen years of single-molecule spectroscopy in physics, chemistry, and biophysics. *J. Phys. Chem. B*, 106:910–927, 2002.

[92] W. E. Moerner and L. Kador. Optical detection and spectroscopy of single molecules in a solid. *Phys. Rev. Lett.*, 62:2535–2538, 1989.

[93] G. Nair. *Many-body processes in the photophysics of colloidal semiconductor nanocrystals*. PhD thesis, Massachusetts Institute of Technology, 2009.

[94] G. Nair, L. Y. Chang, S. G. Geyer, and M. G. Bawendi. Perspective on the prospects of a carrier multiplication nanocrystal solar cell. *Nano Lett.*, 11:2145–2151, 2011.

[95] G. Nair, S. G. Geyer, L.-Y. Chang, and M. G. Bawendi. Carrier multiplication yields in pbs and pbse nanocrystals measured by transient photoluminescence. *Phys. Rev. B*, 78:125325, 2008.

[96] G. Nair, J. Zhao, and M. G. Bawendi. Biexciton quantum yield of single semiconductor nanocrystals from photon statistics. *Nano Lett.*, 11:1136–1140, 2011.

[97] R.G. Neuhauser, K.T. Shimizu, W.K. Woo, S.A. Empedocles, and M. G. Bawendi. Correlation between fluorescence intermittency and spectral diffusion in single semiconductor quantum dots. *Phys. Rev. Lett.*, 85:3301–3304, 2000.

[98] M. Nirmal, B. O. Dabbousi, M. G. Bawendi, J. J. Macklin, J. K. Trautman, T. D. Harris, and L. E. Brus. Fluorescence intermittency in single cadmium selenide nanocrystals. *Nature*, 383(6603):802–804, 1996.

[99] M. Nirmal, D. J. Norris, M. Kuno, M. G. Bawendi, A. L. Efros, and M. Rosen. Observation of the "dark exciton" in cdse quantum dots. *Phys. Rev. Lett.*, 75(20):3728–3731, 1995.

[100] D. J. Norris. *Electronic Structure in Semiconductor Nanocrystals*. Marcel Dekker, 2004.

[101] D. J. Norris and M. G. Bawendi. Measurement and assignment of the size-dependent optical spectrum in cdse quantum dots. *Phys. Rev. B*, 53(24):16338–16346, 1996.

[102] L. Novotny and B. Hecht. *Principles of Nano-Optics*. Cambridge University Press, 2006.

[103] M. Orrit and J. Bernard. Single pentacene molecules detected by fluorescence excitation in a p-terphenyl crystal. *Phys. Rev. Lett.*, 65:2716–2719, 1990.

[104] A. Pandey and P. Guyot-Sionnest. Intraband spectroscopy and band offsets of colloidal ii-vi core/shell structures. *J. Chem. Phys.*, 127:104710, 2007.

[105] N. Panev, M.-E. Pistol, V. Zwiller, L. Samuelson, W. Jiang, B. Xu, and Z. Wang. Random telegraph noise in the photoluminescence of individual $\mathrm{ga}_x\mathrm{in}_{1-x}\mathrm{as}$ quantum dots in gaas. *Phys. Rev. B*, 64:045317, 2001.

[106] Y.-S. Park, A. V. Malko, J. Vela, Y. Chen, Y. Ghosh, F. García-Santamaría, J. A. Hollingsworth, V. I. Klimov, and H. Htoon. Near-unity quantum yields of biexciton emission fro cdse/cds nanocrystals measured using single-particle spectroscopy. *Phys. Rev. Lett.*, 106:187401, 2011.

[107] J. J. H. Pijpers, E. Hendry, M. T. W. Milder, R. Fanciulli, J. Savolainen, J. L. Herek, D. Vanmaekelbergh, S. Ruhman, D. Mocatta, D. Oron, A. Aharoni, U. Banin, and M. Bonn. Carrier multiplication and its reduction by photodoping in colloidal inas quantum dots. *J. Phys. Chem. C.*, 111:4146–4152, 2007.

[108] J. J. H. Pijpers, E. Hendry, M. T. W. Milder, R. Fanciulli, J. Savolainen, J. L. Herek, D. Vanmaekelbergh, S. Ruhman, D. Mocatta, D. Oron, A. Aharoni, U. Banin, and M. Bonn. Carrier multiplication and its reduction by photodoping in colloidal inas quantum dots. *J. Phys. Chem. C.*, 112:4783–4784, 2008.

[109] T. Plakhotnik, M. J. Fernee, B. Littleton, and H. Rubinsztein-Dunlop. Anomalous power laws of spectral diffusion in quantum dots: a connection to luminescence intermittency. *Phys. Rev. Lett.*, 105:167402, 2010.

[110] T. Puangmali, M. Califano, and P. Harrison. Interband and intraband optical transitions in inas nanocrystal quantum dots: A pseudopotential approach. *Phys. Rev. B*, 78:245104, 2008.

[111] W. Qin and P. Guyot-Sionnest. Evidence for the role of holes in blinking: negative and oxidized cdse/cds dots. *ACS Nano*, 6:9125–9132, 2012.

[112] M. T. Rakher, R. Bose, C. W. Wong, and K. Srinivasan. Fiber-based cryogenic and time-resolved spectroscopy of pbs quantum dots. *Opt. Express*, 19:1786–1793, 2011.

[113] M. T. Rakher, L. Ma, O. Slattery, X. Tang, and K. Srinivasan. Quantum transduction of telecommunications-band single photons from a quantum dot by frequency upconversion. *Nature Photon.*, 4:786–791, 2010.

[114] U. Resch-Genger, U. Grabolle, S. Cavaliere-Jaricot, R. Nitschke, and T. Nann. Quantum dots versus organic dyes as fluorescent labels. *Nat. Methods*, 5:763–775, 2008.

[115] E. A. Riley, C. M. Hess, and P. J. Reid. Photoluminescence intermittency from single quantum dots to organic molecules: Emerging themes. *Int. J. Mol. Sci.*, 13:12487–12518, 2012.

[116] S. Rosen, O. Schwartz, and D. Oron. Transient fluorescence of the off state in blinking cdse/cds/zns semiconductor nanocrystals is not governed by auger recombination. *Phys. Rev. Lett.*, 104:157404, 2010.

[117] D. Rosenberg, A. J. Kerman, R. J. Molnar, and E. A. Dauler. High-speed and high-efficiency superconducting nanowire single photon detector array. *Opt. Express*, 21:1440–1447, 2013.

[118] R. L. Sandberg, L. A. Padilha, M. M. Qazilbash, W. K. Bae, R. D. Schaller, J. M. Pietryga, M. J. Stevens, B. Baek, S. W. Nam, and V. I. Klimov. Multiexciton dynamics in infrared-emitting colloidal nanostructures probed by a superconducting nanowire single-photon detector. *ACS Nano*, 6:9532–9540, 2012.

[119] C. Santori, D. Fattal, J. Vuckovic, G. S. Solomon, and Y. Yamamoto. Single-photon generation with inas quantum dots. *New J. Phys.*, 6:1–16, 2004.

[120] E. H. Sargent. Infrared photovoltaics made by solution processing. *Nat. Photonics*, 3:325–331, 2009.

[121] R. D. Schaller, S. A. Crooker, D. A. Bussian, J. M. Pietryga, J. Joo, and V. I. Klimov. Revealing the exciton fine structure of pbse nanocrystal quantum dots using optical spectroscopy in high magnetic fields. *Phys. Rev. Lett.*, 105:067403, 2010.

[122] R. D. Schaller, J. M. Pietryga, and V. I. Klimov. Carrier multiplication in inas nanocrystal quantum dots with an onset defined by the energy conservation limit. *Nano Lett.*, 7:3469–3476, 2007.

[123] G. Schlegel, J. Bohnenberger, I. Potapova, and A. Mews. Fluorescence decay time of single semiconductor nanocrystals. *Phys. Rev. Lett.*, 88:137401, 2002.

[124] G. D. Scholes and G. Rumbles. Excitons in nanoscale systems. *Nature Mater.*, 5:683–696, 2006.

[125] O. Schwartz and D. Oron. A present understanding of colloidal quantum dot blinking. *Isr. J. Chem.*, 52:992–1001, 2012.

[126] X. F. Shen, L. X. You, S. J. Chen, X. Y. Yang, and L. M. Qiu. Performance of superconducting nanowire single photon detection system with different temperature variation. *Cryogenics*, 50:708–710, 2010.

[127] K.T. Shimizu, R.G. Neuhauser, C. A. Leatherdale, S.A. Empedocles, W.K. Woo, and M. G. Bawendi. Blinking statistics in single semiconductor nanocrystal quantum dots. *Phys. Rev. B*, 63:205316, 2001.

[128] Y. Shirasaki, G. J. Supran, M. G. Bawendi, and V. Bulovic. Emergence of colloidal quantum-dot light-emitting technologies. *Nature Photon.*, 7:13–23, 2013.

[129] P. Spinicelli, S. Buil, X. Quélin, B. Mahler, B. Dubertret, and J.-P. Hermier. Bright and grey states in cdse-cds nanocrystals exhibiting strongly reduced blinking. *Phys. Rev. Lett.*, 102:136801, 2009.

[130] M. D. Sturge. Optical absorption of gallium arsenide between 0.6 and 2.75 ev. *Phys. Rev.*, 127:768–773, 1962.

[131] M. Sugisaki, H-W. Ren, K. Nishi, and Y. Masumoto. Fluorescence intermittency in self-assembled inp quantum dots. *Phys. Rev. Lett.*, 86:4883–4886, 2001.

[132] J. Tellinghuisen and C. W. Wilkerson. Bias and precision in the estimation of exponential decay parameters from sparse data. *Anal. Chem.*, 65:1240–1246, 1993.

[133] R. Tenne, A. Teitelboim, P. Rukenstein, M. Dyshel, T. Mokari, and D. Oron. Studying quantum dot blinking through the addition of an engineered inorganic hole trap. *ACS Nano*, 7:5084–5090, 2013.

[134] Rogier Verberk, Antoine M. van Oijen, and Michael Orrit. Simple model for the power-law blinking of single semiconductor nanocrystals. *Phys. Rev. B*, 66:233202, 2002.

[135] Heeres R. W., Dorenbos S. N., B. Koene, G. S. Solomon, L. P. Kouwenhoven, and V. Zwiller. On-chip single plasmon detection. *Nano Lett.*, 10:661–664, 2010.

[136] S. Weiss. Fluorescence spectroscopy of single biomolecules. *Science*, 283:1676–1683, 1999.

[137] P. R. Yu, M. C. Beard, R. J. Ellingson, S. Ferrere, C. Curtis, J. Drexler, F. Luiszer, and A. J. Nozik. Absorption cross-section and related optical properties of colloidal inas quantum dots. *J. Phys. Chem. B*, 109(15):7084–7087, 2005.

[138] K. Zhang, H. Chang, A. Fu, A. P. Alivisatos, and H. Yang. Continuous distribution of emission states from single cdse/zns quantum dots. *Nano Lett.*, 6:843–847, 2006.

[139] J. Zhao, O. Chen, D. B. Strasfeld, and M. G. Bawendi. Biexciton quantum yield heterogeneities in single cdse (cds) core (shell) nanocrystals and its correlation to exciton blinking. *Nano Lett.*, 12:4477–4483, 2012.

[140] J. Zhao, G. Nair, B. R. Fisher, and M. G. Bawendi. Challenge to the charging model of semiconductor-nanocrystal fluorescence intermittency from off-state quantum yields and multiexciton blinking. *Phys. Rev. Lett.*, 104:157403, 2010.

[141] N. Zhao, T. P. Osedach, L. Y. Chang, S. G. Geyer, D. Wanger, M. T. Binda, A. C. Arango, M. G. Bawendi, and V. Bulovic. Colloidal pbs quantum dot solar cells with high fill factor. *ACS Nano*, 4:3743–3752, 2010.

[142] C. Zinoni, B. Alloing, C. Monat, V. Zwiller, L. H. Li, A. Fiore, L. Lunghi, A. Gerardino, H. de Riedmatten, H. Zbinden, and N. Gisin. Time-resolved and antibunching experiments on single quantum dots at 1300nm. *Appl. Phys. Lett.*, 88:131102, 2006.